Nanostructured Electrodes for Lithium Ion Batteries using Biological Scaffolds

by

Yun Jung Lee

B.S. & M.S. Seoul National University

SUBMITTED TO THE DEPARTMENT OF
MATERIALS SCIENCE AND ENGINEERING
IN PARTIAL FULFILLMENT OF THE REQUIREMENT FOR THE DEGREE OF

DOCTOR OF PHILOSOPHY

AT THE
MASSACHUSETTS INSTITUTE OF TECHNOLOGY
SEPTEMBER 2009

Signature of Author:

Department of Materials Science and Engineering
July 31, 2009

Certified by:

Angela M. Belcher
Professor Materials Science and Engineering and Biological Engineering
Thesis Supervisor

Accepted by:

Christine Ortiz
Chair, Departmental Committee on Graduate Students

Nanostructured Electrodes for Lithium Ion Batteries using Biological Scaffolds

by

Yun Jung Lee

Submitted to the Department of Materials Science and Engineering on
July 24, 2009 in Partial Fulfillment of the Requirements for the Degree of
Doctor of Philosophy in Materials Science and Engineering

ABSTRACT

Without doubt, energy and environment are becoming central issues for the future. In this regard, not only device performance but also environmentally sustainable ways of making energy device is important. To meet these needs, a M13 virus based biological toolkit was utilized in this work for controlling nanostructures of lithium ion battery electrodes which is a critical process in developing electrodes materials for high power applications. The M13 biological toolkit provides specificity, versatility and multifunctionality for controlling nanostructure of the materials using basic biological principles. The versatile E4 virus template could nucleate active cathode materials at low temperature by an environmentally benign method. High power lithium ion battery cathode materials were fabricated using genetically programmed multifunctional virus as a versatile scaffold for the synthesis and assembly of materials. A novel strategy for specifically attaching electrochemically active materials to conducting carbon nanotubes networks through biological molecular recognition was developed by manipulating the two-genes of the M13 virus. Viral amorphous iron phosphates cathodes achieved remarkable and otherwise impossible high power performance using this multifunctional virus. This environmentally benign low temperature biological scaffold could facilitate new types of electrode materials by activating a class of materials that have been excluded because of their extremely low electronic conductivity. Architecting nanostructures was further extended to activate noble metal alloy nanowires as anodes for lithium ion batteries by alleviating mechanical stress. By demonstrating electrochemical activity of noble metal alloy nanowires with various compositions, the M13 biological toolkit extended its utility for the study on the basic electrochemical property of materials.

Thesis Advisor: Angela M. Belcher
Title: Germeshausen Professor of Materials Science and Engineering and Biological Engineering

ACKNOWLEGEMENTS

First and foremost, I sincerely thank my advisor, Professor Angela Belcher for motivating, encouraging me and supporting every work done by me throughout my Ph.D. Even when I was in deep slump, Prof. Belcher showed her sincere belief in me and endless support to motivate and encourage me. I also would like to thank my committee members, Professor Gerbrand Ceder for his fruitful advice and scientific guide to my work and Professor Samuel Allen for his kind advices on my thesis. I really appreciate all the help from my many collaborators. I am indebted to Dr. Ki Tae Nam for his help for me on settling in this group. I appreciate Professor Kisuk Kang for the discussions and advice on my research. I also appreciate Hyunjung Yi, Dr. Woo-Jae Kim, Dr. Dong Soo Yoon for successful collaborations. I hope our collaboration would continue for future whenever, wherever we are. I am really indebted to Byungwoo Kang for the deep discussions and valuable advice on the research related to lithium ion battery. I would like to acknowledge all Belcher group members, who provided a great and clean research environment. I'd like to thank Youjin Lee for our current collaboration and for our friendship. I'd like to thank Dahyun Oh, who will take over my research and expand it further. I also deeply appreciate Pastor Dae-Sung Choi and his wife Young-Mi Choi for their holy prayers for me. I thank Professor Euijoon Yoon, my M.S. thesis advisor, who encouraged and motivated me to do Ph.D research. Finally, I really thank my family. Any words cannot express my gratitude to my husband, Kyung Joong Yoon. I really thank his decision to make me study at MIT and every physical and mental support. My life at MIT was balanced only though the life with my husband. I appreciate my father, mother and sisters Eunjung and Soojung for their love and high expectation for me. I sincerely thank my parents in law for their love, support and prayers for me.

BIOGRAPHICAL NOTE

Education

2005-2009	Ph.D at *Department of Materials Science and Engineering* Massachusetts Institute of Technology, U.S.A. Title of Dissertation: Nanostructured electrodes for lithium ion batteries using biological scaffolds Advisor: Angela M.Belcher
1998-2000	M.S. at *Department of Inorganic Materials Engineering,* Seoul National University, Korea Title of Dissertation : Structure analysis of a-Si:H and μc-Si:H grown by UHV-ECR-PECVD Advisor: Euijoon Yoon
1994-1998	B.S at *Department of Inorganic Materials Engineering* Seoul National University, Korea graduated with honors (Summa cum laude)

Professional Experience

2000-2003	Research Engineer at Semiconductor R&D Center, Samsung Electronics, Yongin, Korea Research details: Capacitor Module Integration with Ruthenium Top-electrode for Memory Devices and High-*k* Dielectric Oxide of Capacitor/Transistor Dielectrics for Memory and Logic Devices
1998-2000	Graduate Research Assistant, Semiconductor Materials & Processing Laboratory Seoul National University, Korea Research details: Deposition and Structural Analysis of Hydrogenated Amorphous and Nanocrystalline-Si for Optoelectronic Devices

Awards and Scholarship

2005	Departmental Fellowship from Department of Materials Science and Engineering Massachusetts Institute of Technology, U.S.A.
1998-1999	Scholarship from Young-poong Foundation (Korea) For superior academic achievement
1998	Graduated with Honors (Summa cum laude) Seoul National University, Korea
1995-1997	Scholarship from Chunman Scholarship Foundation (Samchully cooperation) For superior academic achievement
1994	Fellowship from Department of Inorganic Materials Engineering Seoul National University, Korea. For superior academic achievement.

Publications

- **Refereed Journals**
  1. **Ki Tae Nam*, Yun Jung Lee*, Eric M. Krauland, Stephen T. Kottmann, and Angela M. Belcher** (* equally contributed 1st co-author) *Peptide-Mediated Reduction of Silver Ions on Engineered Biological Scaffolds,* ACS Nano, vol.2(7), 1480-1486, 2008
  2. **Ki Tae Nam, Ryan Wartena, Pil J. Yoo, Forrest W. Liau, Yun Jung Lee, Yet-Ming Chiang, Paula T. Hammond, and Angela M. Belcher***,* *Stamped microbattery electrodes based on self-assembled M13 viruses,* Proceedings of the National Academy of Sciences of the United States of America, vol. 105(45) 17227-17231, 2008
  3. **Yun Jung Lee*,, Hyunjung Yi*,, Woo-jae Kim, Kisuk Kang, Dong Soo Yun, Michael S. Strano, Gerbrand Ceder and Angela M Belcher**(* equally contributed 1st co-author) *Fabricating Genetically Engineered High Power Lithium Ion Batteries Using Multiple Virus Genes,* Science, vol.324(5930), 1051-1055, 2009
  4. **Yun Jung Lee*, Youjin Lee* and Angela M. Belcher**(* equally contributed 1st co-author), *Biologically Activated Noble Metal Alloy Nanowires for Lithium Ion Battery Anodes*, in preparation.

- **Conference Proceedings**
  1. **K.-Y. Park, I.-S. Park, K.-V. Lim, Yun Jung Lee, J.-H. Yeo,** *HfO_2 Thin Film Prepared By Atomic Layer Deposition Using $Hf(OtBu)_4$ and O_3,* Japanese Society of Applied Physics Spring Conference, 2003(in Japan)
  2. **K.-V. Lim, I.-S. Park, Yun Jung Lee, J.-H. Yeo, K.-Y. Park** *Characteristics of Al_2O_3/HfO2 Capacitor Deposition by ALD,* Atomic Layer Deposition Conference (ALD 2002), 2002(in Korea)
  3. **Yun Jung Lee, S.-J. Joo, S.-H. Lim, E.Yoon**, *Effect of DC bias on structure of hydrogenated amorphous silicon and microcrystalline silicone*, pp7, Proc. of Korean Vacuum Society 18th Conference, 2000 (in Korea)

TABLES OF CONTENTS

Chapter 1. Introduction

Chapter 2. Peptide-Mediated Reduction of Silver Ions on Engineered Biological Scaffold

Chapter 3. Synthesis of Nanostructured Amorphous Iron Phosphates (a-FePO4) Nanowires Enabled by Virus for Lithium Ion Battery Cathode Electrodes

Chapter 4. Fabricating Genetically Engineered High-Power Lithium Ion Batteries Using Multiple Virus Genes

Chapter 5. Biologically Activated Noble Metal Alloy Nanowires for Lithium Ion Battery Anodes

Chapter 6. Ongoing Research Works and Future Directions

6.1 Hybrid BiF3/SWNTs cathode electrodes

6.2 Nanoparticles synthesis using biological nanoreactor – protein cage

List of Figures

Chapter 1

Introduction

Chapter 1.1 Background

Biological systems have developed biomineralization processes to nucleate, grow, and assemble inorganic materials[1, 2]. Examples of biomineralized products include pearls, bone, keratin, shell, calcite, siliceous materials synthesized by diatoms[3] and sponges[4], and magnetite in magnetotatic bacteria[5]. An important component of biomineralization is the protein or peptide template that controls the shape and crystal structure of biominerals as well as the assembly behavior. The extraction of nucleating biomolecules from the biominerals and the identification of materials specific peptides through combinatorial approaches[6-8] have broadened the possible application of biomineralization in nanoelectronics and nanobiotechnology. The underlying mechanism can be applied to the synthesis of technologically important materials beyond those few existing biominerals in nature. Inspired by biological systems with unique capabilities of specific and precise molecular recognition as well as self-assembly, an M13 bacteriophage (or phage or virus)-based biological toolkit has been developed in designing novel approaches for nanoarchitectured structures and materials[9-15]. Early work in our group focused on the use of phage display for this purpose. Among combinatorial approaches, phage display is a powerful technique in identifying biomolecules that exhibit necessary affinity for specific target materials. This selection process of biomolecules employed in phage display is called biopanning or screening. A phage display library is the pool of bacteriophage which has short peptides express on the surface of filamentous bacteriophage virus. By inserting random peptides on the proteins that constitute the virus, phage libraries are formed. In phage display, target materials are incubated with phage libraries to isolate peptide sequences that have affinity for the specific target. The unbound viruses are washed off and viruses bound to target material are eluted and amplified. The eluted and amplified phages are used as the sub-library for the next round biopanning. After several screening rounds, consensus peptide motif with strong affinity to the specific target is isolated.

The wild type filamentous M13 virus is approximately 6.5 nm in diameter and 880 nm in length[16]. The length of the cylinder reflects the length of the packaged single stranded DNA genome. At one end of the M13 virus, there are approximately five molecules each of protein VII (pVII) and protein IX (pIX). The other end has about five molecules each of protein III (pIII) and protein VI (pVI), totaling 10~16 nm in length. The wild type M13 virus coat is composed of roughly 2700 copies of the major coat protein VIII (pVIII) stacked in units of five in a helical array. To select viruses with affinity for target materials, pIII library with random peptide insert on pIII is generally used and commercially available. However, to template virus surface with materials of interest and utilize the full dimension of virus, effective functionalities on the virus major capsid surface is required. For this purpose, a pVIII library was previously constructed in our group and used for biopanning and biomineralzation of materials such as gold[12] and cobalt-platinum[17]. In addition to the advantage of biomolecular recognition, the functionality of subunit proteins of M13 virus can be modified specifically through genetic engineering. The amino acids of five different surface proteins can be rationally altered independently via genetic engineering. Surface proteins of the M13 virus have been engineered to grow and assemble[14] semiconductor, magnetic[10] and metal oxide nanomaterials[13]. For example, the E4 virus is a genetically modified M13 virus that has tetraglutamate (EEEE-) fused to the amino terminus of each pVIII major coat protein. Due to the presence of extra carboxylic acid groups compared with wild-type M13 virus (M13KE), E4 virus exhibits increased ionic interaction with cations, thus can serve as a template for materials growth[13, 18]. The E4 virus served as a general platform in templating functional materials in this study.

It has been suggested that more sustainable ways of making batteries are important for sustainable technologies of the future[19]. Biological systems offer unique capabilities for environmentally benign materials synthesis. For example, phosphate species manipulation in DNA and ATP formation is mediated by biomolecules. Motivated by this phosphate species manipulation, enzyme-mediated synthesis of $LiFePO_4$ have been envisaged[19]. Our group has shown the possibility of virus-enabled fabrication of lithium ion battery by synthesizing electrochemically active anode nanowires and organizing the virus on a polymer surface[13, 20]. The improvement of performance was possible using inherent structural properties of the virus and basic biological principles. The rod shape of virus ensures a high surface to volume ratio to the nanowires templated on it and also leads to the unusual ability to align on a polymer surface which results in flexibility in designing battery architecture. Incorporation of conducting nanoparticles to make heterostuctures was also achieved by common biological methods. Through this pioneering work, we anticipated that this versatile biological platform could be further explored in fabricating high power lithium ion batteries with remarkable performance.

Chapter 1.2 Scope of work

This work was focused on use of biological scaffolds in designing and fabricating electrode materials for lithium ion batteries. In this study, basic biological principles were applied to control nanostructures of materials for lithium ion batteies. In designing nanostructured electrodes for high power batteries, multifunctionality is required to achieve better electrical wiring. Multifunctional viruses have been engineered with desired modifications on different positions of the protein coat to achieve unique structural components[11, 12, 21]. This research explored how the multifunctionality of biology can be applied to improve the practical lithium ion battery device performance. The summary of each chapter is as follows:

Chapter 2 describes the spontaneous reduction of silver ions into nanostructures by yeast surface-displayed glutamic acid (E_6) and aspartic acid (D_6) peptides. As an effort to understand the interaction between E4 virus and cations, we focused on the role of carboxylic acid containing peptides expressed on yeast surfaces. Light spectroscopy and electron microscopy reveal that silver ions are photoreduced in the presence of the polycarboxylic acid-containing peptides and ambient light, with an increase in reduction capability of E_6 expressing yeast over D_6 yeast. The importance of tethering peptides to a biological scaffold was inferred by observing the reduced particle forming capacity of soluble peptides with respect to corresponding yeast-displayed peptides. This principle was further extended to the M13 virus for fabrication of crystalline silver nanowires. These insights into the spontaneous reduction of metal ions on biological scaffolds should help further the formation of novel nanomaterials in biological systems.

Chapter 3 presents the virus-enabled synthesis of nanostructured cathode materials for lithium ion battery using a low temperature and environmentally benign process. There is a growing need for nanostructured electrodes for lithium ion batteries for high power applications. Reducing materials dimension could enhance lithium intercalation kinetics, however, nanosized particles formation is still challenging in traditional high temperature process. Hydrolysis of Fe^{+3} ions during the synthesis was prevented by conjugate formation with carboxylic groups expressed on the surface of E4 virus and 4℃ low temperature synthesis. Nanowires of a-$FePO_4\cdot H_2O$ with particle size of 10-20 nm in diameter were templated on the E4 virus, but still showed limited utilization of active materials when tested as a cathode for lithium ion battery. Remarkable performance improvement was made by the formation of heterostructure with silver nanoparticles and the dehydration of structural water. The electrochemical property of biologically derived a-$FePO_4$ was similar to the best reported values for a-$FePO_4$ synthesized at high temperature.

Chapter 4 demonstrates a genetically programmed multifunctional virus as a versatile scaffold for the synthesis and assembly of materials for high power batteries. Development of materials that deliver more energy at high charge/discharge rates is important for high power applications including portable electronic devices and hybrid electric vehicles. Reducing materials dimensions for lithium ion batteries can boost Li^+ ion and electron transfer in nanostructured electrodes. We developed a strategy for attaching electrochemically active materials to conducting carbon nanotubes networks through biological molecular recognition. By manipulating two-genes of the M13 virus, viruses were equipped with peptide groups with affinity for single-walled carbon nanotubes (SWNTs) on one end and peptides capable of nucleating amorphous iron phosphate (a-$FePO_4$) fused to the viral major coat protein. For the virus clone that demonstrated 10 times greater affinity towards SWNTs, power performance of a-$FePO_4$ was comparable to that of crystalline lithium iron phosphate (c-$LiFePO_4$) even with 5 w%

SWNTs. The electrodes showed excellent capacity retention upon cycling at 1C for at least 50 cycles. When the materials were cycled between 1.5 and 4.3 V, the first discharge capacity at 10C reached 130 mAh/g, which is comparable to the capacity from state-of-art c-$LiFePO_4$. This environmentally benign low temperature biological scaffold could facilitate fabrication of electrodes from materials that have been excluded because of their extremely low electronic conductivity.

Chapter 5 reports the synthesis and electrochemical activity of noble metal and noble metal alloy nanowires using multiple virus clones for lithium ion batteries anode materials. Using two clones for specificity (p8#9 virus) and versatility (E4 virus), noble metal nanowires of high aspect ratio with diameters below 50 nm were successfully synthesized with control over particle size, morphology and compositions. The biologically derived noble metal alloy nanowires with diameter below 50 nm showed electrochemical activities toward lithium even when the electrodes were prepared from bulk powder forms. We demonstrated that improvement in capacity retention was also possible by optimizing composition, thickness and morphology. By demonstrating electrochemical activity of noble metal alloy nanowires with various compositions, M13 biological toolkit extended its utility for the study on the basic electrochemical property of materials.

Chapter 6 presents on-going research works and future directions. To electrochemically activate insulating bismuth fluoride as a cathode for lithium ion battery, multifunctional viruses developed for high power lithium ion battery in chapter 4 were applied and tested. The encountered problems are described and strategy for future research is suggested. Preliminary results on the use of ferritin protein cage as a biological nanoreactor are also provided.

Chapter 2

Peptide-Mediated Reduction of Silver Ions on Engineered Biological Scaffold

Chapter 2.1 Introduction

Peptides have been engineered to grow and assemble[14] semiconductor, magnetic[10], metal oxide nanomaterials[13], and we extend this approach to the spontaneous reduction of silver by introducing peptide sequences on yeast and M13 viruses to facilitate the growth of templated silver nanostructures. Organisms such as bacteria[22] and fungi[23] are reported to synthesize silver particles intra- or extracelluarly when they are exposed to silver salts. Although there is growing interest in the bioinspired synthesis of silver nanoparticles, a general understanding of growth is not yet known. Recently, the role of specific peptide motifs has been explored through identification of dodecamer peptides that are reported to generate silver nanoparticles of various morphology[24]. The importance of peptides was demonstrated as studies with single amino acid solutions of lysine, proline, serine, and arginine showed them to be incapable of silver reduction[24]. Additionally, tryptophan and aspartate, which can be used as reducing agents in the synthesis of gold nanoparticles, did not show the ability to reduce silver ions[25]. Although it has been experimentally demonstrated that the biological system such as cells, enzymes and peptides can reduce the metal ions, the detailed mechanisms are not well understood. The conformation, overall charge, and functional groups of biomolecules may all contribute to biological reduction in conjunction with solution pH, light, temperature, and other ions in solution.

As an effort to contribute to the understanding of spontaneous reduction and the interaction between E4 virus and cations, we focus on the role of carboxylic acid containing peptides expressed on yeast surfaces. Yeast surface display provides a convenient model system for the study of genetically engineered biomolecules with inorganic materials[26] while carboxylic acid groups are known to coordinate metal ions which may act as a nucleation site for nanoparticle formation[27-29]. Additionally, glutamic and aspartic acid rich peptides play an important role in biomineral growth as evident in the high population in biomineralizing protein sequences. While previous research has studied long polypeptide chains or single amino acids, this work utilizes hexamer peptides that are short enough to deduce side-chain influence while long enough to have multi-valent interactions. Additionally, previous reports of silver biomineralization occur in the solution with minimal control over the spatial distribution. In this work, the genetically engineered yeasts not only mediate the reduction of silver ions through expressed peptides, but also act as templates for controlled spatial growth of particles. Specifically, our findings demonstrate spontaneous reduction of silver facilitated by carboxylic acid groups in the presence of ambient light. The principle of the peptide-mediated reduction elucidated by the engineered yeast was further extended to a filamentous M13 virus scaffold for fabricating crystalline silver nanowires.

Chapter 2.2 Experimental

Genetic Engineering of Yeast Displayed Peptides. Hexamer peptides were engineered onto the surface of yeast as previously described[26]. Briefly, peptides were displayed as fusions to the C-terminus of Aga2, which is encoded on a 2-micron plasmid downstream of a Gal-based promoter. The expression vectors were maintained in *S. cerevisiae* strain EBY100, which has Aga1 under control of a Gal-based promoter integrated in its genome, as previously described[26]. Peptide expression vectors (X_6) were generated from annealed oligonucleotides (i.e. G_6 peptide oligos: 5'GTGGCggtggtg-gtggtggcggaTAGCCAGTAGC and 5'CTGGCTAtccgccaccaccaccaccGCCACCGCC) with BstXI compatible sticky ends ligated into BstXI sites of expression vector pBPZ. The complete list of oligonucleotides used is available upon request. All vectors were amplified, sequenced, and then transformed into EBY100. Peptide expression was induced by growing cells at mid-log phase in Select-Galactose media at 30 °C for 18-24 hours.

Silver Reduction by Yeast. Among various silver salt precursors, silver acetate ($AgOOCCH_3$) salt was chosen because metal ions from acetate salt were found to load faster and to a greater extent within block copolymer containing carboxylic acid group than metal ions from chlorides, nitrates and sulfates[27]. In addition, the silver ion reduction rate constant from silver formate (AgOOCH), which has almost the same structure as $AgOOCCH_3$, was reported as higher than that of Ag_2SO_4 and $AgNO_3$[28]. Silver acetate salt (99% pure) was obtained from Alfa Aesar. In a typical experiment, engineered 1 O.D. (O.D. is equivalent to absorbance units at 600 nm) yeast cells (10^6-10^7 cells) were washed 3 times in 1ml of Millipore water and incubated in 1mM aqueous solution of $AgOOCCH_3$ for 24-90 hours at room temperature under ambient light. To prevent buffer mediated reduction, all experiments were conducted in purified water.

The sample was agitated via rocking to avoid yeast cell sedimentation. For control experiments in which the mixtures were kept in the dark, the vials were wrapped with aluminum foils and placed in the dark room. These samples were analyzed by UV-Vis absorption spectroscopy, Transmission Electron Microscopy (JEOL 200CX TEM and JEOL 2010 TEM) and Environmental Scanning Electron Microscopy (FEI/Philips XL 30 FEG-ESEM). For TEM analysis, solutions were dropped on the copper grid, washed with distilled water several times and dried. For SEM specimen preparation, yeast cells were first settled on a silicon substrate. After four hours fixation with 2 % (v/v) glutaraldehyde, 2 % (v/v) paraformaldehyde, 5 % sucrose in 0.1 M sodium cacodylate buffer, the specimen was rinsed in distilled water, dehydrated in 100 % dry ethanol and critical point dried in CO_2. Specimens were examined in FEI/Philips XL 30 FEG-ESEM with and without surface carbon coating layers.

Genetic Engineering of M13 Virus and Silver Reduction by the Engineered Virus. To display tetraglutamic acid (-EEEE) on the n-terminus of the p8 protein on M13 bacteriophage (producing so-called E4 phage), a small DNA duplex encoding the amino acids was made using an oligonucleotides 5'-CTACTACAAGGATCCTCCTCCT CCTCTGCAGCGAAAGACAGCA-3' and the extension primer, 5'- GATGCTGTCTTTCGCTGCAG-3'. The duplex was digested with *Pst*I and *Bam*HI and ligated into M13SK phage vector, and confirmed by DNA sequencing. The E4 phage was incubated in an aqueous solution 1mM $AgOOCCH_3$ for two hours at room temperature under ambient light. All experiments were performed in purified water and E4 phage was dialyzed against purified water overnight to prevent buffer effect. These samples were analyzed by UV-Vis absorption spectroscopy and Transmission Electron Microscopy (JEOL 200CX TEM and JEOL 2010 TEM). For TEM analysis, solutions were dropped on the copper grid, washed with distilled water several times and dried.

Molecular Simulation of the Hexamer Peptides . Monte Carlo (MC) simulations of the hexamer peptides were performed using the OPLS-AA force field (Jorgensen, W.L., MCPRO, Version 1.68, Yale University, New Haven, CT, 2002). The effects of the aqueous solution environment were included through a solvation energy term in the Monte Carlo energy calculation. The solvation energy of each peptide conformation was calculated as the sum of a polar term, evaluated from the solution of the Poisson-Boltzmann equation, and a non-polar term modeled as proportionate to the molecular surface area. Poisson-Boltzmann calculations were carried out using a multigrid solver with a grid spacing of 0.3 A. Atomic charge and radius parameters were taken from the OPLS-AA force field. Internal and external dielectric constants were set to 1 and 80, respectively, in order to remain consistent with the OPLS force field. Each simulation included equilibration for 100k MC steps prior to averaging over 1M MC steps in the NPT ensemble. Conformations were saved periodically from the resulting ensemble and subsequently used to evaluate average properties of the peptides.

Chapter 2.3 Results and Discussion

When the hexa-glutamic acid expressed (clone named as E_6) or hexa-aspartic acid expressed (clone named as D_6) engineered yeasts were incubated in an aqueous solution of $AgOOCCH_3$ for 24 hours at room temperature, the solution turned an orange color as shown in Fig. 2.1A. Reduction of the silver ions was evident by a gradual and steady increase of the reddish color. The characteristic reddish colors of the solution and absorption peak at ~400 nm are due to surface plasmon resonance of silver nanoparticles and are dependent on the size and shape of the particles. Interestingly, without any known reducing agent in solution, silver ions were bio-reduced by the genetically engineered yeast. Contrary to E_6 or D_6 yeasts, little color change was seen for yeast expressing hexa-glycine (clone named as G_6) (Fig. 2.1B), and solutions without yeast did not show any color change. To prevent the buffer mediated reduction, all our experiments were conducted in purified water (Millpore Mill-Q, 18.2 MΩ-cm) without the presence of any buffer salts. These control experiments indicate that the carboxylic acid groups of glutamic acid or aspartic acid are involved in the reduction of silver ions. Typically, the carboxylic acid groups in block copolymer systems have been utilized for silver deposition because of their binding affinity to positive silver ions. However, in all the cases, the post treatment with a reducing agent, such as H_2[29] and $NaBH_4$[30], or UV[28] and γ- radiation[31], was necessary. To our knowledge, there is no prior report of carboxylic acid mediated silver reduction in water at ambient conditions. Previous report about silver nanoparticles organization on Tobacco mosaic virus (TMV)[32] showed the importance of glutamate and aspartate in site-specific mineralization of silver, but contribution of these peptides to the silver reduction itself was not considered. To understand the reduction mechanism, we conducted control experiments in which the mixtures were kept in the dark. Interestingly, even after a few days, no reduction was evident in these samples (Fig. 2.1). All the control reactions were also conducted with rocking to prevent cell sedimentation. Conversely, mixtures kept under ambient light but with UV energy blocking polymer coatings, exhibited significant silver reduction. This polymer coating effectively blocked UV light with wavelength below 300 nm. To further reduce the effect of UV light, the same experiments were done under white fluorescent light in dark room. The solution also showed significant silver reduction. (Fig. 2.2). This result suggests that the reduction of silver ions is the cooperative result of the carboxylic acid and ambient light. Among ambient light, it would be visible light that assumes the most significant role in the reduction process. Even though the un-induced cells, named UI, expressed no surface peptides, the yeast solution changed colors with absorption peak comparable to D_6. However, the adsorption peak in E6 samples is much higher than uninduced sample. In the case of sample UI, the reduction of silver ion is possibly due to negative charge and the presence of polysaccharide on the yeast surface. Previously other groups demonstrated polysaccharides and their derivatives are shown to photo-chemically synthesize metal nanoparticles such as gold and silver[33-35] using UV light as a reducing agent. However, the growth of silver particles with un-induced cells was less controlled than peptide-assisted nucleation, as witnessed by further electron microscopy analysis. Furthermore, the electron microscopy analysis using TEM and SEM is believed to be more accurate than the UV/Vis absorbance in comparing the reduction capability.

Transmission electron microscopy (TEM) analysis (Fig.2.3C~2G) showed homogeneous silver nanoparticles with sizes of approximately 10-20 nm coated on the cell wall of yeast expressing peptides. Consistent with the color change and UV-Vis absorption spectroscopy trends, the average particle size was larger and the distribution density greater for the E_6 than for the D_6 solution. An electron diffraction pattern (Fig. 2.3H) and a high resolution TEM (HRTEM) image (Fig. 2.3I) confirmed that the particles coating the yeast were crystalline silver nanoparticles. The silver nanoparticles were not aggregated but stabilized by the expressed peptides. For the un-induced yeast (Fig. 2.3A, B), the morphological features were quite different from that of induced ones. No obvious coating layer was observed and silver nanoparticles were not bound to the surface of the yeast and aggregated to large irregular particles (Fig. 2.4)

As mentioned above, the silver ion reduction in this case could have been mediated by the negative charge or polysaccharide of the yeast surface. It is likely that the silver nanoparticles formed by polysaccharides were not strongly bound to the yeast surface due to the weak interaction between the silver particles and the polysaccharides[33]. This could also explain why the number of silver nanoparticles near the yeast surface was much less than that of D_6 even though UV-Vis absorption and color change were similar. Scanning Electron Microscopy (SEM) analysis (Fig. 2.5A-C, E-G) also demonstrates that engineered yeast provided a template for silver nanoparticle growth and the density of nanoparticles could be controlled by means of genetic engineering of expressed peptides. Silver nanoparticles appeared as bright dots due to their electron dense metallic character. Conversely, a lack of nanoparticles was noticed in E_6 yeast not exposed to silver solution (Fig. 2.5D, H).

These results suggest that the combination of carboxylic acid-containing peptides and ambient light facilitate the reduction of silver into nanoparticulates. Although an exact photoreduction mechanism is still under investigation, we believe that the energy barrier for silver reduction is lowered when silver atoms are bound to peptides containing carboxylic groups. Carboxylic groups are nucleophilic such that their binding with silver ions induces partial electron transfer displacing the Fermi level of silver cluster toward the more negative potentials. This hypothesis is supported by experimental results from other groups. It was reported that when silver ions are bound to carboxylic acid group, UV photo-reduction of silver ion become more facile[36]. In this regard, silver ion binding to carboxyl groups catalyzes the reduction of silver ions, as in the case of silver ion-catalyzed amine oxidation[37] and silver ion-catalyzed amino acid oxidation[38]. We believe that water could be an electron source for the initial nucleation of silver. Recently, solvated electrons in water have been observed[39] as well as water dissociation mechanisms, that may account for these water-derived electrons. Like the proposed mechanism in photochemical reductions of Fe(III) complexes of polycarboxylates, the carboxylate radical activated by the visible light can be possibly involved.[40] In our system, once a silver atom is formed, it becomes easier for silver ions to be photochemically reduced due to the increased reduction potential of silver clusters and metallic characteristic of silver atoms. However, the exact mechanism is still under investigation.

Surprisingly, silver ions exposed to E_6 yeast result in greater nanoparticle formation than those exposed to D_6 yeast. Assuming a similar binding affinity of Ag^+ to the carboxylic acid, the different reduction kinetics appears counterintuitive. In order to understand differential reduction between E_6 and D_6 yeast, we explored the local conformation of these peptides. When present as an individual neutral amino acid, silver ion affinity of glutamate was calculated to be slightly higher than aspartic acid using hybrid density functional theory[41]. This difference may be amplified when aggregated over six residues. In addition, Monte Carlo simulations show a structural difference between the peptides. The additional alkyl link in glutamic acid allows for slight increases in conformational freedom and non-polar surface area, resulting in a more folded backbone conformation. This gives rise to a pocket-like structure in hexa-glutamic acid (Fig. 2.6.), while hexa-aspartic acid on average assumes a more linear conformation. We hypothesize that the pocket-like structure of E_6 peptides creates a greater local concentration of carboxylic acid residues and therefore, a greater level of silver ions. This may increase particle formation as the silver redox potential depends on the number of Ag in the cluster. The redox potential of a single silver ion is -1.8 V and increases as the atom number in a cluster increases up to 0.799 V for bulk silver[42]. Taken together, silver ions bound to carboxyl groups reduce more easily while simultaneously increasing the local concentration of silver ions, which may further reduce the energy barriers to reduction. As a result of these cooperative mechanisms, silver ions can be photo-reduced by the carboxylic acid group even under ambient light.

The importance of fixing peptides to a biological template was demonstrated by observing the nanoparticle growth of soluble peptides. We tested the reduction ability of various concentrations of soluble hexa-glutamic acid peptide in silver solution (1 nM - 1 mM peptide solution, 1 mM - 8 mM $AgOOCCH_3$ solution). According to the absorption data, reduction was only observed at 1 mM peptide and 8 mM $AgOOCCH_3$ solution (Fig. 2.7). Considering the approximate number of hexa-glutamate peptides on the yeast (5×10^4 peptides/cell) and the yeast concentration (1 O.D. $\sim 2 \times 10^7$ cells/ml), the total concentration of the peptides expressed on all the yeasts in solution is $\sim 10^{12}$ peptides/ml. Conversely, the soluble peptide experiments at 1 mM contained 6×10^{17} peptides/ml. Indeed, there are no prior reports on the silver ion reduction mediated by soluble glutamic or aspartic acid peptides. Therefore, the fixing of the peptides in a biological scaffold on the yeast surface may be an additional factor in the reduction mechanism. Enhanced reaction rate has been observed before in other constrained systems including "membrane catalysis" [43, 44]and "micelle catalysis"[45] when one of two reactants remains fixed on a two-dimensional surface. This may be explained by the increased collision probability of reactants towards a fixed target[46-48]. The yeast biological templates inherently provide a two-dimensional tethering effect, so we can expect more efficient reactions on our biological scaffolds. To further investigate peptide-mediated reduction, we expanded this rationale to template silver nanowires on an M13 bacteriophage surface that has increased surface peptide density.

In order to template silver nanowires, we engineered a tetraglutamic acid peptide (-EEEE, called E4) onto the n-terminus of p8, the major coat protein of M13 bacteriophage. Roughly 2700 copies of the p8 major coat protein self-assemble into the capsid of the wild type virus, resulting in 5 fold rotation symmetry along the length of virus. Previously, the E4 virus was utilized as a biological template to grow and assemble cobalt oxide nanowires for nanostructured Li ion battery electrodes[13]. There has also been an effort to coat TMV more densely with silver by genetic insertion of two cysteine residues, but the resultant template was not a fully covered nanowire but a string of nanoparticles[49]. In their study, the spacing between nearest neighbor peptides expressed for TMV is similar to that of M13 virus. We speculate that the different concentration of metal ions and viruses and the different binding character may explain the difference in morphology in those two studies. We anticipate that the higher density of glutamate expressed on peptides of the engineered M13 bacteriophage (as compared to that of the yeast) can lead to the formation of nanowires. Indeed, computational simulation of p8 protein assembly shows that the distance between the helically arranged nearest neighbors of the tetraglutamate is around 3 nm at 100% incorporation[10].

When E4 virus was incubated in an aqueous solution of 1 mM silver acetate for two hours at room temperature, the solution turned red as shown in Fig. 2.8A. The appearance of a red color clearly indicated the reduction of silver ions. Alternatively, a silver solution incubated with wild type phage (M13KE) exhibited a turbid yellow color, and revealed that large and irregular precipitates were formed. UV-Vis spectra showed no absorption peak between 200 nm and 800 nm. The reduction of silver ions by wild type viruses was presumably due to the negatively charged surface of the virus[50] as with the yeast surface.

TEM analysis shows the detailed structure of nucleated silver on the virus particles. Wire-like structures were observed along the length the E4 (Fig. 2.8B). Conversely, wild-type virus produced large and irregular silver particles (Fig. 2.9). The length of silver wires on the E4 virus corresponds to the length of the virus particles, and the thickness is approximately 30 nm. The high resolution TEM image in Fig. 2.8D shows the silver wire formed on the E4 virus. The crystallographic structure of silver wires made by the E4 virus was determined by SAED in combination with HRTEM.

A diffraction image (Fig. 2.8D) shows the single crystal patterns of <100> and <112> are superimposed. Diffraction spots from (200), (020), and (220) planes of square symmetry correspond to the [001] zone while the (111), (220) and (311) diffraction spots of rectangular symmetry correspond to the [112][32]zone. The additional spots can be explained by double diffraction. This analysis suggests that five 111 twin boundaries are located cyclically with D5h symmetry along the longitudinal axis of Ag wire[51]. The formation of the crystals may be associated with the highly oriented p8 proteins and the five-fold symmetry of the arrangement of p8 proteins. The nucleation and growth process seem to have an analogy to the molecular epitaxy in biomineralization[52] and epitaxial growth in vacuum technology. In contrast, we previously reported the regulation of the crystal orientation on the viruses where the textured assembly of nanoparticles was transformed into single crystal nanowires via heat-annealing based on the mechanism of orientated aggregation-based crystal growth[10]. Here, the higher density of incorporated peptides allows the nucleated silver to grow in the thermodynamically most favorable single crystalline form without post annealing on the scaffold.

Chapter 2.4 Conclusion

The genetically engineered scaffolds not only mediate the reduction of silver ions but also act as templates for the synthesis of nanostructures. Our results demonstrate that short peptides containing carboxylic acid functional groups facilitate reduction under ambient light and the reduction ability is dependent on the local concentration of silver ions associated with the conformation of peptide. Additionally, this study suggests that tethering peptides to a biological scaffold enhances the reduction ability, and the surface density of the peptides on the scaffold determine the final nanostructure of silver. We anticipate that this study will contribute to the understanding of the spontaneous reduction of metal ions in biological systems and facilitate the implementation of environmentally benign biological methods for fabricating technologically important nanomaterials.

Chapter 2.5 Figures

Figure 2.1. Characterization of yeast solutions incubated in 1 mM $AgCOOCH_3$ solution. Yeast cell concentration is 1 O.D. Yeast solutions are named for corresponding clones. Expressed peptides are: E_6 - hexa-glutamic acids, D_6 – hexa-aspartic acids, G_6 – hexa-glycine acids, UI- uninduced clone with no surface expressed peptides, E6 dark - hexa-glutamic acids, incubated in the dark. (A) Photograph of the yeast solutions shows color change resulting from silver nanoparticles formation. (B) UV-Vis absorption spectra of the same solutions. Peak at 260 nm comes from DNA of yeast cells.

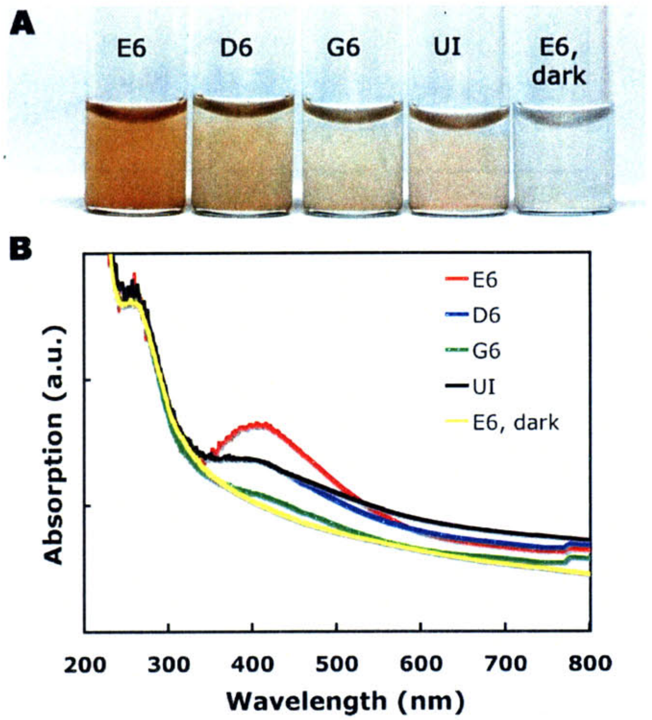

Figure 2.2. **UV-Vis absorption spectra of the E_6 yeast with and without UV-light blocking polymer coatings under white fluorescent light in dark room. Yeast solutions are incubated in 1 mM $AgOOCCH_3$ solution.**

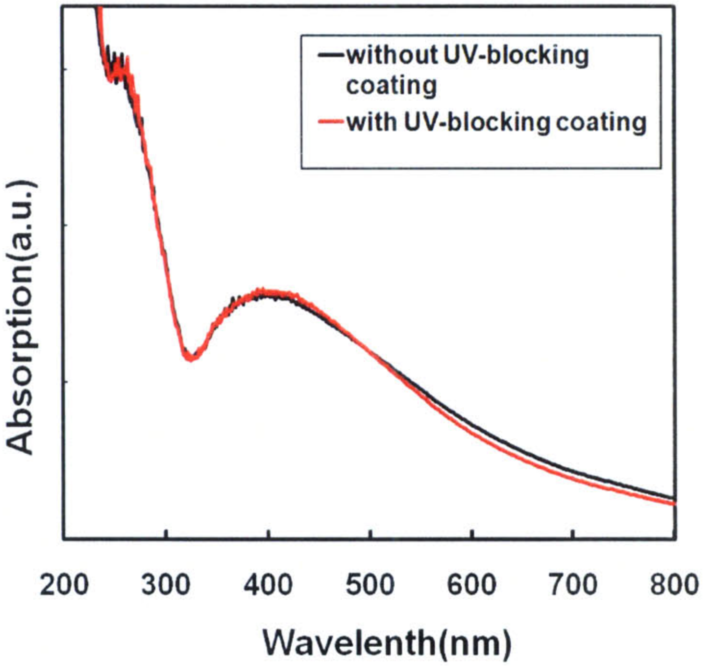

Figure 2.3. TEM analysis of silver reduction by engineered yeast. For all solutions, yeast cell concentration is 1 O.D. and $AgOOCCH_3$ concentration is 1mM. (A) Un-induced(UI). (B) Un-induced(UI) high magnification. (C) D_6. (D) D_6 high magnification. (E) E_6. (F) E_6 high magnification. (G) Low magnification image of E_6 showing several cells coated with silver nanoparticles layer. (H) Electron diffraction pattern confirms the crystalline nature of the silver nanoparticles. (I) High Resolution TEM image of silver nanoparticles.

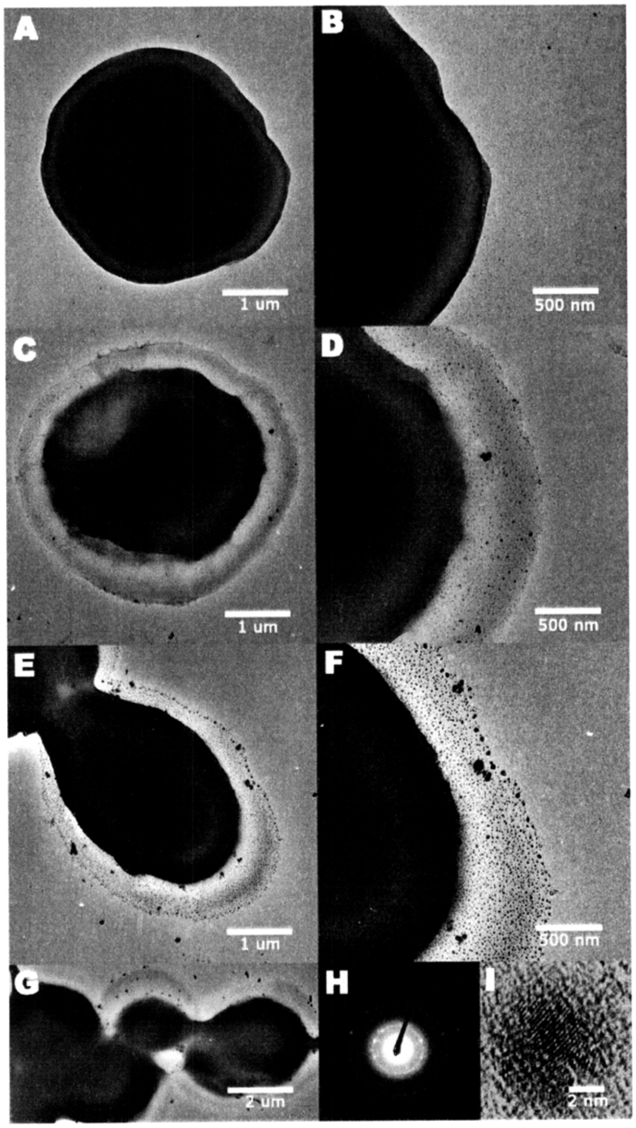

Figure 2.4. Silver nanoparticles synthesized by un-induced yeast solution. Particles are aggregated and not bound to yeast surface peptides.

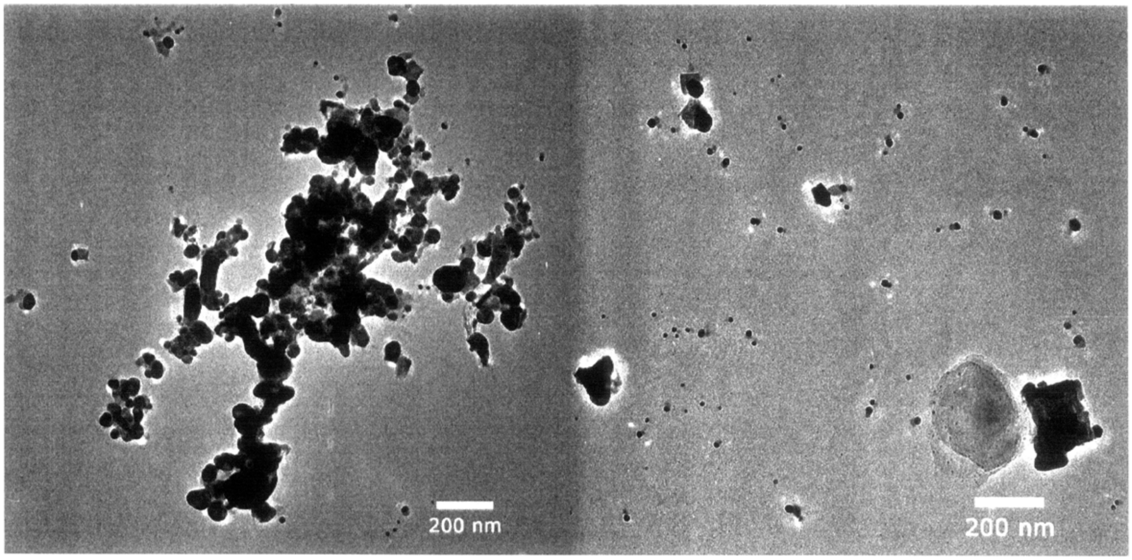

Figure 2.5. Scanning electron micrographs of yeast cells. The yeast solutions are prepared as those in Fig. 3.3, except control sample. Control sample is pristine E_6 yeast not exposed to silver solution. (A)-(D) Low magnification images (5000-30000X) of yeast cells with carbon 10nm coating layer: (A)-(C) E_6, (D) control sample. (E)-(H) High magnification images (80000X) without coating layer: (E) E_6, (F) D_6, (G) Un-induced (UI), (H) control sample. Yeast cells were not coated with conducting materials to visualize small particle features.

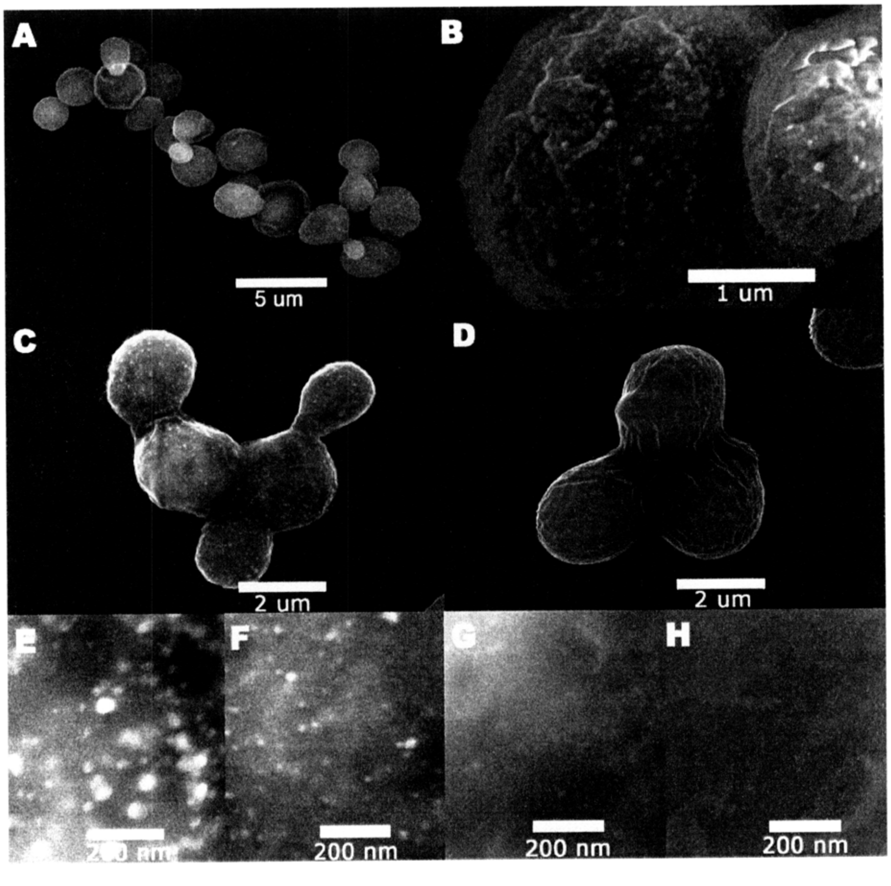

Figure 2.6. Average conformations of (A) hexa-aspartic acids(D_6) and (B) hexa-glutamic acids(E_6) from Monte Carlo simulations. Atom colors are: grey – carbon, white – hydrogen, red – oxygen, blue – nitrogen. Blue spheres indicate counter ions ($Z = +1$) placed in simulation to balance charge during the simulation.

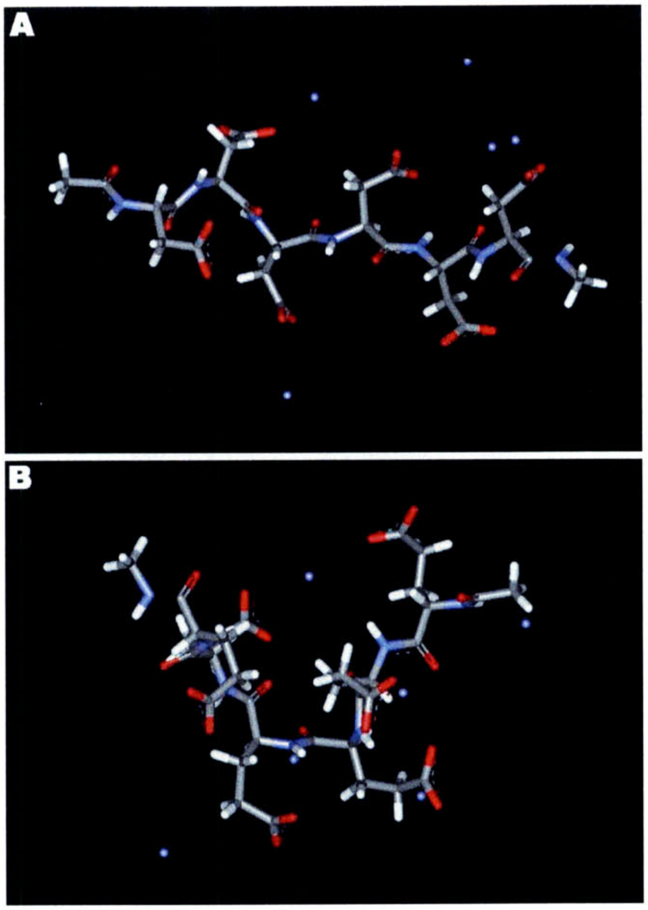

Figure 2.7. UV-Vis absorption analysis of the silver reduction by soluble hexa-glutamic acid peptide. (A) Various peptide concentrations. Concentration of $AgOOCCH_3$ is 8 mM. (B) Various $AgOOCCH_3$ solution concentrations. Concentration of hexa-glutamic acid solution is 1 mM.

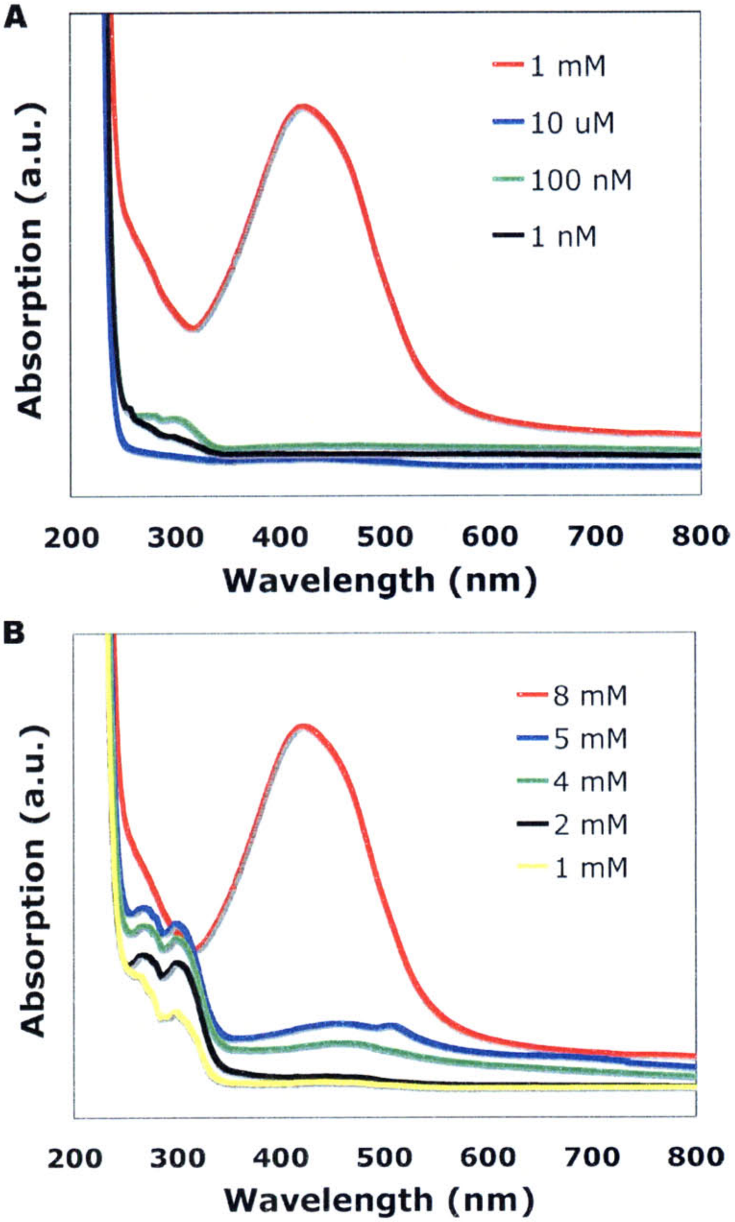

Figure 2.8. Silver reduction by engineered virus (A) photographs of the silver solution reduced by E4 virus (left) and wild type virus (B) TEM image of the virus based silver wires (C) High resolution TEM image of the virus based silver wire (D) High resolution TEM image of the virus based silver wire and diffraction pattern (inset).

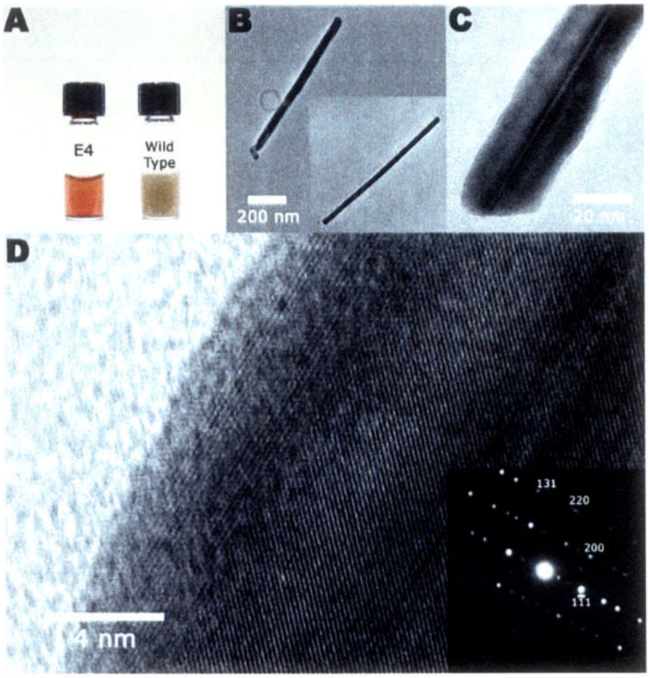

Figure 2.9. Silver nanoparticles produced by wild-type M13 viruses. Large and irregular silver particles are generated.

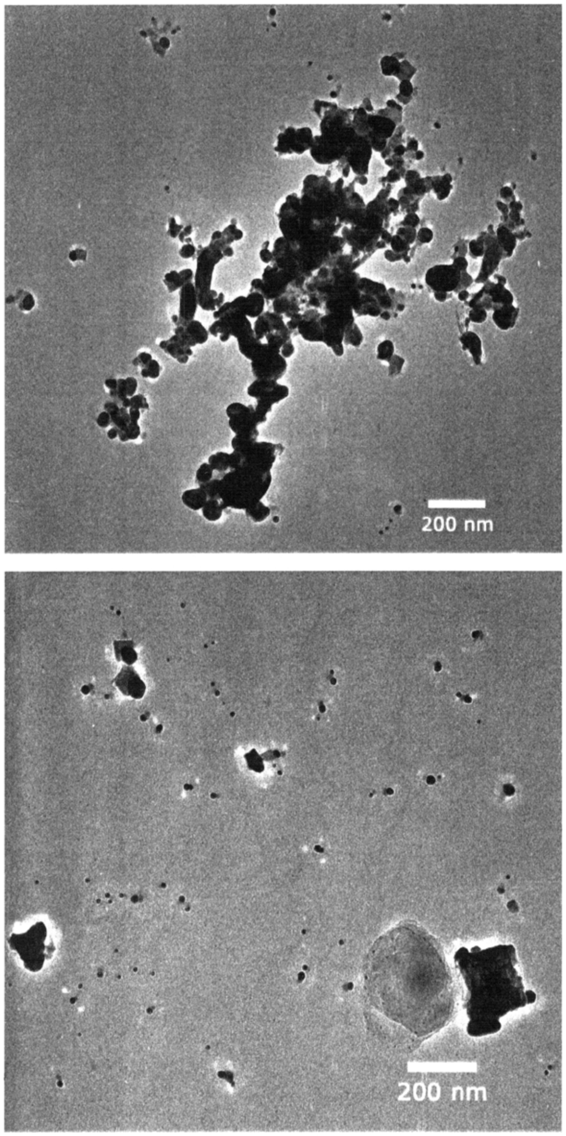

Chapter 3

Synthesis of Nanostructured Amorphous Iron Phosphates (a-$FePO_4$) Nanowires Enabled by Virus for Lithium Ion Battery Cathode Electrodes

Chapter 3.1 Introduction

Although the lithium ion battery has a high energy density, it is considered as a low-power device (slow charge/discharge). Lithium ion battery electrodes store and release electrical energy by insertion and extraction of Li^+ ions and electrons through the electrode materials. Therefore, increasing transport of Li^+ ions and electrons in electrodes can enhance energy storage at high charge and discharge rates. For high power applications, controlling nanostructure has become a critical process in developing electrode materials to boost transport in composite electrodes[19, 53] especially for the electrically insulating transition metal phosphate cathode materials. Among them, iron phosphate based materials have elicited attention as promising Li ion battery positive electrode materials due to their lower toxicity, lower cost, and improved safety through improved chemical, thermal, and structural stability for high power applications[54]. However, their practical use has been constrained due to kinetic limitations, which result in poor charge and discharge rate capability and fading of capacity upon prolonged cycling. To address the rate limitation of these materials, most researchers have focused on tailoring particle size[55, 56] to reduce both the ionic and electronic path within the particles and enhancing electronic conductivity with surface carbon coating layers[57] or conducting nanoparticles additives[58, 59]. The best result for iron phosphate was reported by adopting mesoporous structures with residual carbon to enhance both ionic and electronic transport. This mesoporous iron phosphate could deliver 110 mAh/g at 1C and 85 mAh/g at 3C rate[60]. However, the fabrication of nanosized particles is still challenging since the materials require at least 350 °C for crystallization and carbon coating. Despite the recent advances in novel synthesis, the smallest particle size remains 20-40 nm[56].

Biological systems offer capabilities for environmentally benign materials synthesis. An M13 virus-based biological toolkit has been developed for the design of nanoarchitectured structures and materials[7, 11-13]. Our group has shown that M13 bacteriophage (phage or virus) can be used for battery device fabrication with improved performance by synthesizing electrochemically active anode nanowires and organizing the virus on a polymer surface[13, 20]. Here we demonstrated virus-enabled low temperature synthesis of nanostructured amorphous iron phosphate (a-$FePO_4 \cdot nH_2O$, n=0 or 1) materials for lithium ion battery cathodes.

Chapter 3.2 Experimental

Synthesis of virus-based electrode E4 viruses were amplified using *Escherichia coli* bacterial medium and purified by standard PEG/NaCl precipitation method. (i) For the a-$FePO_4 \cdot H_2O$ synthesis, 200 μl aqueous virus solution ($2x10^{11}$ PFU/ml) was incubated with 1 mM, 1 ml $FeCl_3 \cdot 6H_2O$ for 24 hours at 4°C. Growth completed after reacting with 1 mM, 1 ml Na_3PO_4 at pH=7.5 for 24 hours at 4 °C. The final solution was filtered and washed with water several times. The collected powder was dried in a 100 °C vacuum oven overnight. (ii) For the (Ag) a-$FePO_4 \cdot H_2O$ synthesis, 1 ml virus solution in 0.1 M TBS buffer ($2x10^{11}$ PFU/ml) was dialyzed against pH=9.5 water overnight, followed by incubation with 1 mM, 1 ml silver acetate ($AgOOCCH_3$) solution for 12 hours in the dark at room temperature. All solutions were aqueous after the virus dialysis. The Ag nanoparticles (NPs) were formed by reducing with 5 mM, 1 ml sodium borohydride ($NaBH_4$) for 4 hours at room temperature. This Ag NPs-loaded virus solution was dialyzed against pure water (Millipore Milli-Q, 18.2 MΩ-cm) at room temperature to remove remaining ions. (Ag)a-$FePO_4 \cdot H_2O$ viral nanowires were synthesized on these Ag NPs loaded E4 virus using $Fe(NO_3)_3 \cdot 9H_2O$ precursor. The Ag NPs-loaded E4 structure was incubated with 1.33 mM, 9 ml $Fe(NO_3)_3 \cdot 9H_2O$ to have final concentration of 1 mM for 24 hours at 4°C in order to suppress hydrolysis of Fe^{+3} ions into oxide/hydroxide. Amorphous iron phosphate nanowires were produced after reacting with 1 mM, 12 ml Na_3PO_4 at pH=7.5 for 24 hours at 4 °C. The final solution was filtered and washed with water several times. The collected powder was dried in a 100 °C vacuum oven overnight. (iii) For the (AgCl)a-$FePO_4$ synthesis, the procedure was the same for the growth of (Ag)a-$FePO_4 \cdot H_2O$ nanowires, but $FeCl_3 \cdot 6H_2O$ precursor was used instead of $Fe(NO_3)_3 \cdot 9H_2O$.

Structural and Chemical analysis The microstructure of nanowires was analyzed with Transmission Electron Microscopy (JEOL 200CX TEM). For TEM analysis, solutions were dropped on copper grids, washed with distilled water several times and dried. Chemical composition was determined by DCP-AES (Luvak, Boylston, MA). For Thermo Gravimetric Analysis (TGA), a RGA Q50 (TA instrument) apparatus was used. Samples placed on a platinum pan were preheated to 100 °C and held for 5 min to remove surface absorbed water. After cooling down to 30°C, samples were heated to 700 °C at a heating rate of 10 °C /min in 90 ml/min nitrogen flow and 10 ml/min helium flow. X-Ray Diffraction (XRD) was done using Cu K_α radiation and a Rigaku RU300 powder diffractometer.

Electrochemical tests For positive electrodes preparation, viral a-$FePO_4$ nanowires were mixed with Super P (TIMCAL, SUPER P® Li) carbon black and polytetrafluoroethylene (PTFE) binder. (A) For mixing ratio of powder tested: Super P carbon: PTFE = 80:15: 5. Detailed mass ratio of each component in electrodes are: (i) For a-$FePO_4 \cdot H_2O$, a-$FePO_4 \cdot H_2O$: virus: Super P carbon: PTFE=66.64: 13.36: 15: 5. (ii) For Ag nanowire mixed a-$FePO_4 \cdot H_2O$, a-$FePO_4 \cdot H_2O$: virus: Ag: Super P carbon: PTFE=63.3: 12.7: 5: 15: 5. (iii) For (Ag)a-$FePO_4 \cdot H_2O$, a-$FePO_4 \cdot H_2O$: virus: Ag: Super P carbon: PTFE=67.6: 8.3: 4.1:15:5. (iv) For (AgCl)a-$FePO_4$, a-$FePO_4$: virus: AgCl: Super P carbon: PTFE=61.3: 14.5: 4.2: 15: 5. (B) For mixing ratio of powder tested: Super P carbon: PTFE = 70:25: 5. Detailed mass ratio of each component in electrodes are: (i) For a-$FePO_4 \cdot H_2O$, a-$FePO_4 \cdot H_2O$: virus: Super P carbon: PTFE=58.31: 11.69: 25: 5. (ii) For (Ag)a-$FePO_4 \cdot H_2O$, a-$FePO_4 \cdot H_2O$: virus: Ag :Super P carbon: PTFE= 59.15: 7.28: 3:57: 25: 5. (iii) For (AgCl)a-$FePO_4$, a-$FePO_4$: virus: AgCl: Super P carbon: PTFE=52.9: 13.4: 3.7: 25: 5.The mixture was roll milled and punched into disks with diameters of 8 mm. The typical electrode thickness was 20 to 40 μm. The cell was assembled in an argon filled glove box using lithium foil as a negative electrode, a microporous polymer separator (Celgard 3501^{TM}) and liquid electrolyte mixtures of 1 M $LiPF_6$ in ethylene carbonate: dimethyl carbonate (EC: DMC) = 1: 1 in volume ratio (Ferro Corporation). The testing cell was a coin cell configuration. The assembled cell was galvanostatically tested using a Solatron Analytical 1470E potentiostat. Rates are reported in C-rate convention, where C/n is the rate (current per gram) corresponding to complete charging or discharging to the theoretical capacity of the materials in n hours. Here, 1C corresponds to 178 mA/g for (AgCl)a-$FePO_4$ and 161 mAh/g for a-$FePO_4 \cdot H_2O$ and (Ag)a-$FePO_4 \cdot H_2O$. At each rate, the test cell was fully charged before starting the first discharge by charging at C/10 rate to 4.3 V and applying constant voltage at 4.3 V until the current density was lower than C/100. Impedance measurements of the testing cell before and after galvanostatic test was done using Princeton Applied Research PARSTAT® 2273 potentiostat and impedance analyzer. The impedance response was obtained by applying 10 mV ac potential excitation in a frequency range from 10^5 to 0.1 Hz.

Chapter 3.3 Results and Discussion

Virus-enabled nanostructured cathode materials were first demonstrated by templating amorphous iron phosphate (a-$FePO_4 \cdot nH_2O$) on the E4 virus. E4 is a modified M13 virus that has tetraglutamate (EEEE-) fused to the amino terminus of each copy of pVIII major coat protein. Due to the presence of extra carboxylic acid groups compared with wild-type M13 virus (M13KE), the E4 virus exhibits increased ionic interactions with cations, and can serve as a template for materials growth[13, 18, 20]. Since only one gene (gVIII in Fig. 4.2A) has been modified for the desired peptide motif on pVIII, we call this E4 clone a one-gene system.

Initial trials for the synthesis of virus enabled amorphous iron phosphates at room temperature were not successful. The interaction between carboxylic acid groups and Fe^{+3} ions was reported not very fast[27], hence prolonged incubation of Fe^{+3} with E4 virus was required to make uniform carboxylic groups-Fe^{+3} ions conjugates along the E4 virus. However, Fe^{+3} ions are easily hydrolyzed in aqueous system resulting yellowish solution of iron oxide/hydroxide. Short incubation time of 1 or 2 hours could prevent hydrolysis, however, the reaction products were not continuous nanowires along the virus but free particles aggregates which was formed non-specifically in the bulk of solution. In order to make uniform nanowires along the virus, incubation of Fe^{+3} ions with E4 virus was done at 4℃ to suppress hydrolysis of Fe^{+3} ions during the synthesis process. To test the feasibility of 4℃ low temperature process for the stable E4 virus- Fe^{+3} ions conjugate formation without hydrolysis, solution containing Fe^{+3} ions were stored at 4℃ for 8 days. Solution containing Fe^{+3} ions stored in the presence of E4 virus did not show color change to yellow while the same solution without virus showed clear color change after 8 days. In Fig. 3.1A, E4 virus looked stained with Fe^{3+} ions indicating formation of E4 virus- Fe^{3+} ions conjugates. In the solution without virus, needle-like crystals of iron oxide/hydroxide were formed in Fig. 3.1B. There were no needle-like crystals in the solution containing E4 virus. Therefore we speculate that Fe $^{3+}$ ions-E4 virus conjugates formation could suppress Fe $^{3+}$ ions hydrolysis at 4 ℃.

Synthesis process optimization for the growth of viral amorphous iron phosphates resulted in 24 hours of Fe $^{3+}$ ions incubation with E4 virus and 24 hours of growth after addition Na_3PO_4 at 4 ℃ for the growth of a-$FePO_4 \cdot H_2O$ viral nanowires. For structural analysis of a-$FePO_4 \cdot H_2O$ viral nanowires, transmission electron microscope (TEM) analysis was done. Broad amorphous peaks confirmed amorphous nature of $FePO_4$. Figure 3.2A shows TEM images of a-$FePO_4 \cdot H_2O$ nanowires with particle sizes of 10 to 20 nm in diameter templated on the virus. In TEM-EDX analysis for the same nanowires (Fig. 3.2B), Fe, P and O peaks were clearly identified. The chemical analysis by direct current plasma atomic emission spectroscopy (DCP-AES) confirmed the atomic ratio of Fe to P as 1: 1. Although viruses themselves have phosphate groups in their DNA (7270 phosphate group per one virus particle), the fraction of phosphate groups from DNA is below 1%. To determine structural water content in the synthesized nanowires, thermo gravimetric analysis (TGA) was performed. Generally, hydrated a-$FePO_4$ (a-$FePO_4 \cdot nH_2O$, n=2-4) is precipitated in aqueous solutions containing Fe^{3+} and PO_4^{3-} ions around pH=7-8 and anhydrous structures can be obtained through the dehydration of a-$FePO_4 \cdot nH_2O$ by thermal annealing at 400 °C. Most structural water in a-$FePO_4 \cdot nH_2O$ is removed from the structure around 200 °C[61]. Figure 3.3A is a TGA curve of bare virus alone, and viruses mainly decomposed between 200 ~ 500 °C remaining 13 wt% residues. Based on this TGA curve of virus alone and the TGA curve from the synthesized viral amorphous iron phosphates, the structural water content was determined as 10 wt%, which corresponds to n=1 in a-$FePO_4 \cdot nH_2O$.

Therefore, the nanowires described above was denoted a-$FePO_4 \cdot H_2O$ in the following. Virus content was determined as 16.7 wt%.

Before testing viral a-$FePO_4 \cdot H_2O$ as a lithium ion battery cathode, electrochemical response of bare virus in the voltage window of cathode was evaluated first. In Fig. 3.4, there was virtually no capacity observed at a rate of 15 mA/g (current corresponds to ~ C/10 rate for a-$FePO_4 \cdot H_2O$ electrodes). At a very slow rate of 1.5 mA/g (current corresponds to ~ C/100 rate for a-$FePO_4 \cdot H_2O$ electrodes), signs of irreversible oxidation was observed when the potential is over 4 V. Thus, we concluded that the virus is electrochemically inactive under most testing conditions used in this study.

Electrochemical performance of viral a-$FePO_4 \cdot H_2O$ as a lithium ion battery cathode was evaluated. (Fig. 3.5) In first discharge profile in Fig. 3.5 (A), specific capacity at a rate of C/10 was 100 mAh/g, but rate capability was not very good as shown in Fig. 3.5(A) and (B). In Fig. 3.5(B), there is a capacity loss at 2nd cycle, but capacity retention was stable after 2nd cycle. Capacity loss at the 2nd cycle is a characteristic of this a-$FePO_4.nH_2O$ material[61-63]. a-$FePO_4 \cdot H_2O$ nanowires templated on the virus shows slightly improved specific capacity compared to a-$FePO_4 \cdot H_2O$ powder sample synthesized by the same procedure without virus, possibly due to the nanosized particles formation on the virus coat protein. However, these results are still not yet satisfactory since the capacity is below 50 % of the theoretical value when tested faster than C/2 rate. Since a-$FePO_4.nH_2O$ is electrically insulating, this non-satisfactory response is possibly related to the lack of effective electron transport through the composite electrode which could prevent full electrochemical utilization of the active materials. Accordingly, we attempted to increase electronic conductivity of our cathode materials by dispersing silver nanoparticles. For this purpose, we have used two different biological approaches to incorporate silver nanostructures into the a-$FePO_4$ materials.

In the first method "entanglement", separate virus template (also E4) to grow silver nanowires was used and solution of Ag nanowires grown on E4 virus (detailed growth will be presented in Chapter 5) was mixed with a-$FePO_4 \cdot H_2O$ solution for a-$FePO_4 \cdot H_2O$/Ag network. In the second method the "heterostructure", both materials nucleated on the same wire. Amorphous iron phosphate nanowires were produced on silver nanoparticles (Ag NPs) loaded E4 virus. Uniformly distributed Ag NPs loading along the coat protein of E4 virus (Fig. 3.6A) was initially intended to increase electronic conductivity[13, 58, 59]. Very fine (~5 nm) nanoparticles were uniformly distributed along the virus. When $Fe(NO_3)3 \cdot 9H_2O$ was used as iron precursor, (Ag)a-$FePO_4 \cdot H_2O$ viral nanowires were synthesized. Structural water content was confirmed using TGA. TGA (Fig. 3.6B) also determined virus content as 10.4 wt%. Ag NPs content was 5.1 wt% by DCP-AES. Surprisingly the viral nanowires produced on Ag NPs-loaded E4 were anhydrous as synthesized when $FeCl_3 \cdot 6H_2O$ was used as iron precursor.(Fig 3.7B) Figure 3.7A shows TEM images of these nanowires with particle size of 10 to 20 nm in diameter templated on the virus. Atomic ratio of Fe to P was also 1:1 by DCP-AES. X-ray powder diffraction (XRD) of a-$FePO_4$ nanowires on Ag-NPs loaded E4 (Fig. 3.7 C left) before electrochemical test showed only peaks indexed as silver chloride (AgCl). From XRD result, these nanowires were denoted as (AgCl)a-$FePO_4$. We speculate that the dehydration of a-$FePO_4 . nH_2O$ is related to the chlorination of Ag NPs, which could occur during the incubation with the iron chloride precursor. Part of chlorinated AgCl was reduced to metallic Ag after electrochemical test. (Fig 3.7C right) The reduced metallic Ag could enhance local electronic conductivity as Au nanoparticles could in Co_3O_4/Au heterostructured nanowires[13]. Although the exact mechanism of dehydration is under investigation, dehydration of structural water without thermal treatment was accomplished by low-temperature and environmentally benign chemistry. The dehydrated structure increases the theoretical capacity to 178 mAh/g, making it a good cathode material.

The electrochemical performance of various viral a-$FePO_4$ nanowires as a lithium ion battery cathode was evaluated and compared (Fig. 3.8). In Fig. 3.8, all electrodes were prepared with mixing ratio of power tested: Super P carbon: PTFE = 80: 15: 5 and specific discharge capacity at C/5 rate for 10 cycles is presented. With the addition of Ag nanowires, specific capacity increased from 80 mAh/g (without Ag nanowires) to 90 mAh/g. Specific capacity improvements were more pronounced for the heterestructured nanowires. The first discharge capacity of (Ag)a-$FePO_4 \cdot H_2O$ viral nanowires was 120 mAh/g and the capacity was stabilized to 105 mAh/g. Although Ag nanowires can provide local a-$FePO_4 \cdot H_2O$ nanowires/Ag nanowires network in the entanglement method, they cannot make a percolating networks since Ag nanowires tend to aggregate by themselves rather than making well dispersed network throughout the structure. In addition, due to the high gravimetric density of Ag metal (10.5 g/cm^3), it is difficult to exceed the percolation threshold volume with the amount of 5 wt% even if it is well dispersed. The beneficial effect of Ag NPs in heterostructure method over Ag nanowires thus can be considered that efficient inter- a-$FePO_4 \cdot H_2O$ particles- bridge provided by Ag NPs uniformly dispersed throughout the entire system is more advantageous than locally limited network formation by Ag nanowires in enhancing overall electronic conductivity through the whole composite electrode. The highest specific capacity was obtained with the anhydrous (AgCl)a-$FePO_4$ viral nanowires that have higher theoretical capacity than other nanowires in this study. The heterostructured (AgCl)a-$FePO_4$ viral nanowires electrodes gave the highest first discharge capacity of 145 mAh/g, however, showed poor capacity retention upon cycling. The capacity decreased to ~100 mAh/g within 10 cycles. This poor cycling property might be associated with the volume change during the reduction of AgCl (density = 5.56 g/cm^3) to metallic Ag (density = 10.5 g/cm^3) that occurred during electrochemical test as shown in Fig. 3.7(C). Although reduced metallic Ag could increase local electronic conductivity if the contacts are intact, the volume change could disrupt intimate contacts between particles increasing internal resistance.

To accommodate the volume change and thus improve cycling property, electrodes were prepared with increased carbon content. Increased carbon content could ensure the contacts between particles even when there is a volume change during the electrochemical test. In Fig. 3.9A, the improvement in the capacity retention of (AgCl)a-$FePO_4$ viral nanowires are clearly demonstrated as expected. Since the theoretical capacity has been increased due to dehydration, the discharge capacity was higher than that of a-$FePO_4 \cdot H_2O$ nanowires test rates from C/10 to 10C (Fig. 3.9B). Nyquist plot in Fig. 3.9C shows the high-medium frequency impedance response of (AgCl)a-$FePO_4$ viral nanowires before and after electrochemical test. The size of semicircles in medium frequency represents bulk resistance while the high frequency semicircles are associated with the particle to particle contacts with size of semicircle reflecting particles contact resistance[60, 64]. In most cases, both contact impedance and charge transfer impedance increase with cycling[64]. In Fig 3.9(C), (AgCl)a-$FePO_4$ viral nanowires electrodes did not show significant particle to particle contact impedance before test. After 35 cycles of test, high frequency impedance associated with particle to particle contacts increases, however, bulk resistance decreases with cycling for (AgCl)a-$FePO_4$. This unusual behavior could be caused by the reduction of AgCl to Ag with cycling. The reduced metallic Ag enhanced local electronic conductivity, in other words, decreased bulk resistance in the composite electrodes as expected.

The electrochemical power performance of (AgCl)a-$FePO_4$ viral nanowires as a lithium ion battery cathode was evaluated. (Fig 3.10A and B) The first discharge capacity at a low discharge rate of C/10 was 165 mAh/g (93 % of the theoretical value) and that of 1C discharge rate was 110 mAh/g (Fig. 3.10A). The rate performance is also presented as a Ragone plot (Fig. 3.10B). In most electrode materials, specific energy decreases substantially as one applies more power (high rates) drawing more current from the electrodes[65]. These rate performance values are similar to the best reported values for a-$FePO_4$ synthesized at high temperature[60]. Even with this one gene system, the nanostructuring of a-$FePO_4$ nanowires by the virus enabled an enhanced performance.

Chapter 3.4 Conclusion

Amorphous iron phosphate nanowires for lithium ion battery cathode were synthesized using genetically engineered M13 virus, E4 virus. This biological template enabled elaborate materials nanostructure design as well as low temperature, environmentally benign synthesis. By implementing heterostructures with silver, we demonstrated experimentally that uniformly distributed Ag nanoparticles appeared more advantageous that locally limited network formation by Ag nanowires in enhancing overall electronic conductivity through the whole composite electrodes. Electrochemical property was further improved by dehydration of structural waters. The synergetic use of biological template and synthetic chemistry could enable the synthesis of anhydrous a-$FePO_4$ without thermal treatment by low-temperature and environmentally benign chemistry. The electrochemical properties are similar to the best reported values for a-$FePO_4$ synthesized at high temperature. In this study, we paved the important way for the practical applications of biological approaches in designing and fabricating energy devices, which may be a promising alternative to the traditional processing techniques that consume energy and are costly.

Chapter 3.5 Figures

Figure 3.1. Changes in Fe $^{3+}$ ions stored at 4℃ for 8 days. (A) With virus. Virus looked stained with Fe $^{3+}$ ions indicating formation of E4 virus- Fe $^{3+}$ ions conjugates. (B) Without virus. Without virus, Fe^{+3} ions were hydrolyzed to needle-like crystals.

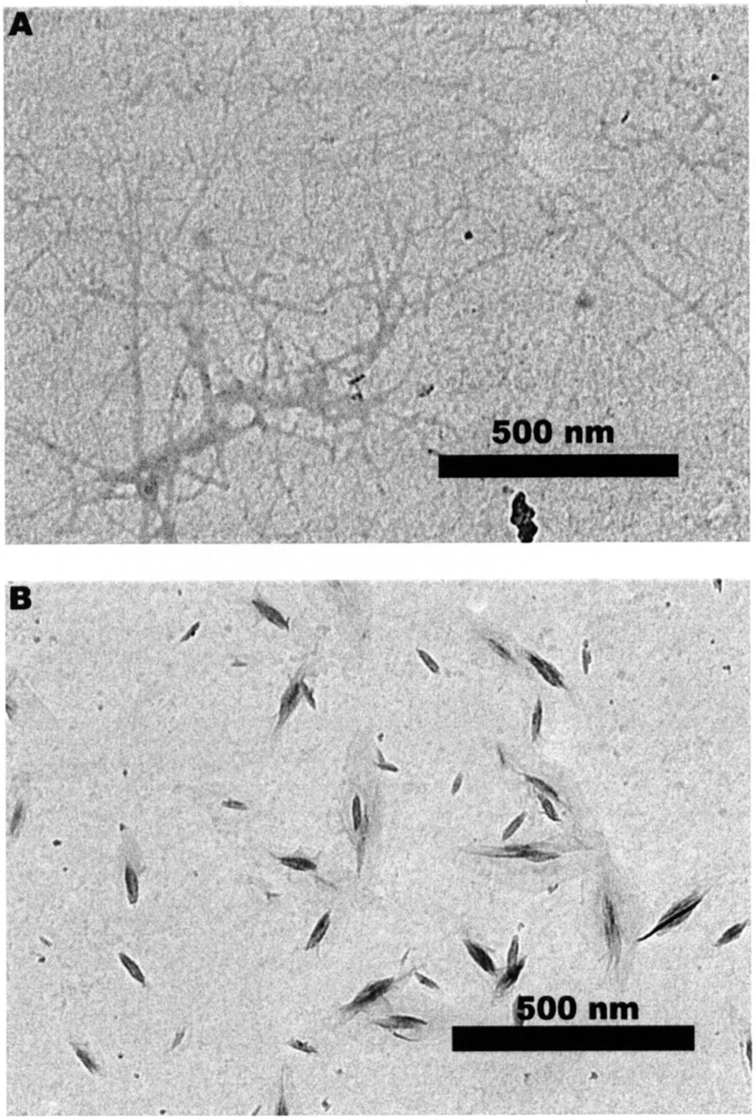

Figure 3.2. a-$FePO_4 \cdot H_2O$ nanowires templated on the virus (A) TEM images of a-$FePO_4 \cdot H_2O$ nanowires on E4 virus. Particle size was 20-30 nm. (B) EDX showing the presence of Fe, P and O in the template nanowires.

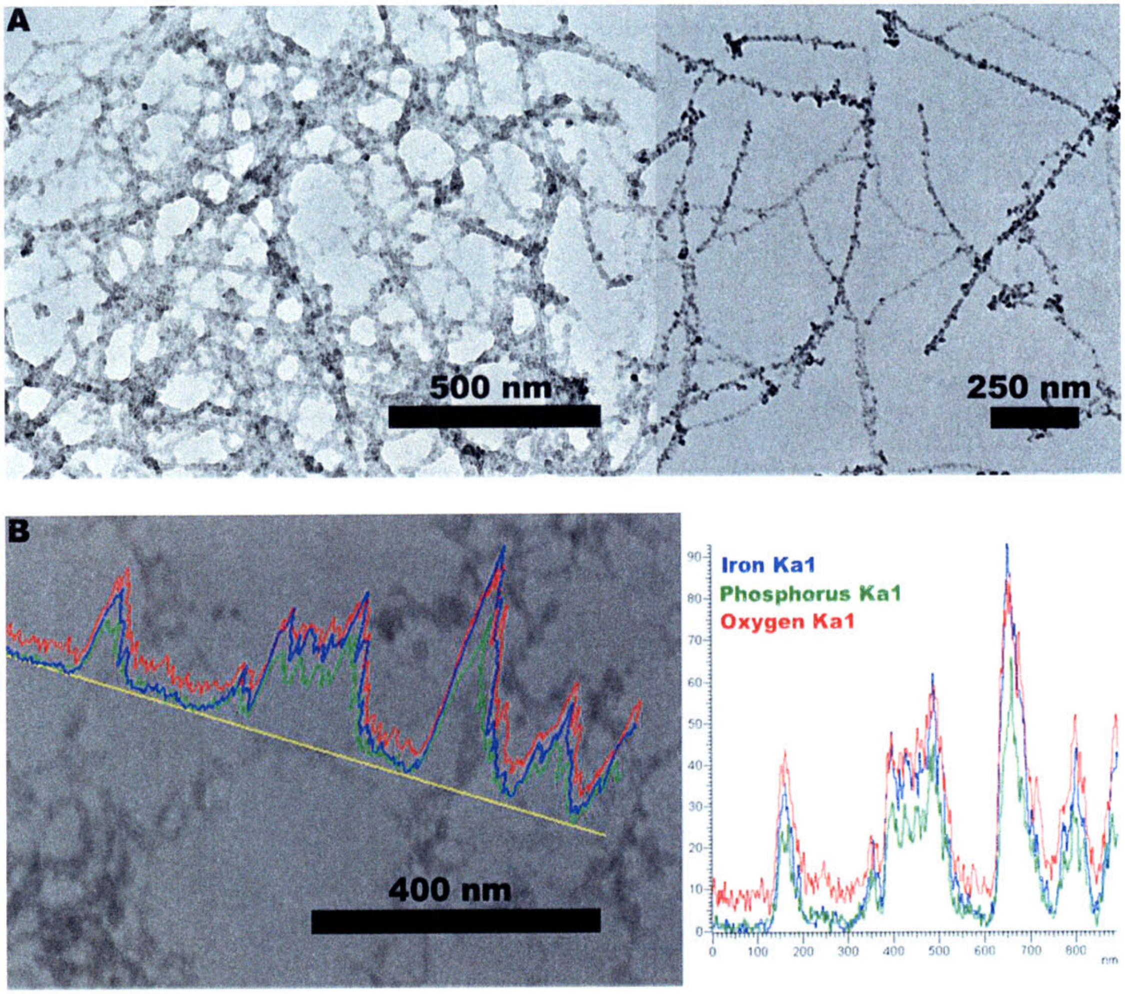

Figure 3.3. Thermo Gravimetric Analysis (TGA) curve of (A) Virus only. Virus mainly decomposes at temperature range 200~500℃ remaining 13.0 wt% residues. (B) a-$FePO_4 \cdot H_2O$ templated on E4 virus. Weight loss below 200℃ is form the structural water.

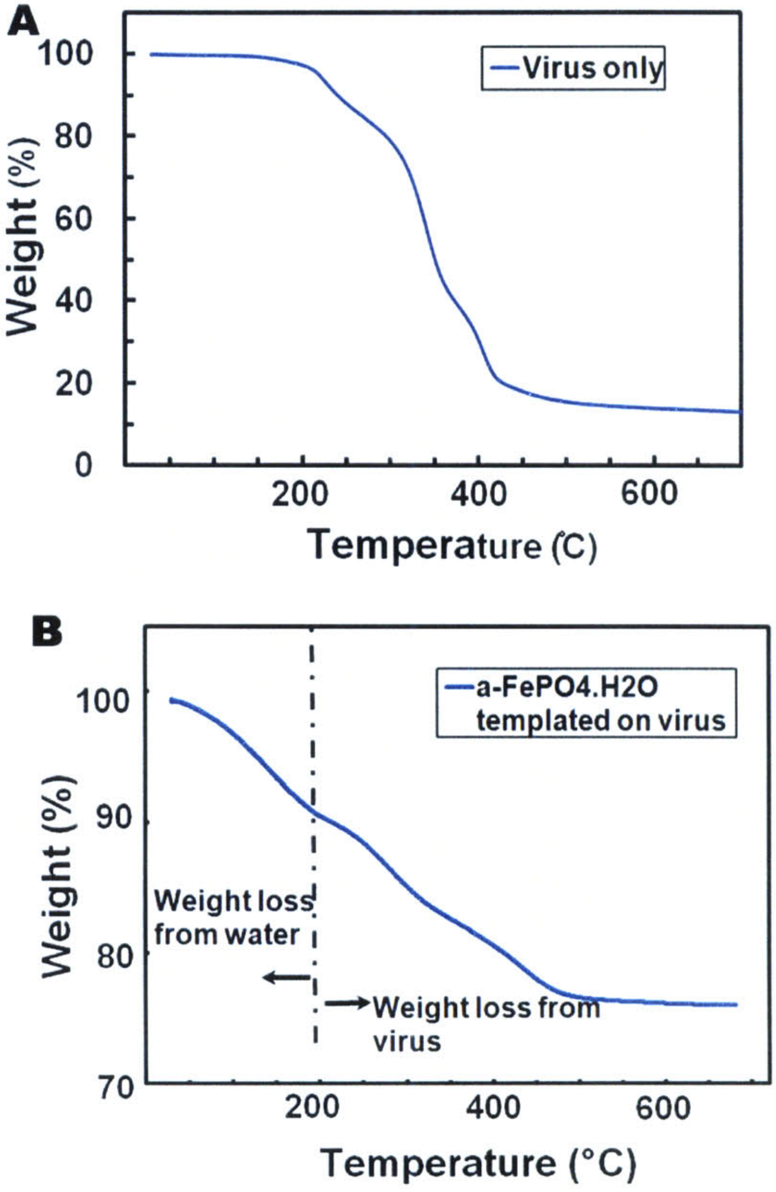

Figure 3.4. Electrochemical response of the bare virus tested between 1.5 and 4.3 V. Electrodes was prepared with mass ratio of powder tested (bare virus): Super P carbon: PTFE= 70: 25: 5.

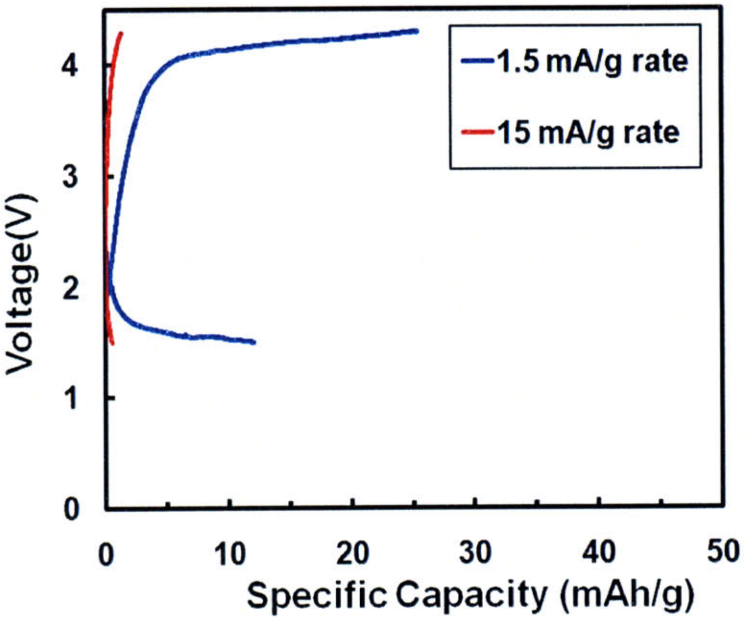

Figure 3.5. Electrochemical property of a-$FePO_4 \cdot H_2O$ viral nanowires template on E4 virus tested between 2.0 and 4.3 V. Electrodes was prepared with mass ratio of powder tested: Super P carbon: PTFE= 80: 15: 5. (A) First charge/discharge curves at rates of C/10, C/5, C/2 and 1C. (B) Specific discharge capacity upon cycling at different rate: C/10, C/5, C/2 and 1C. (C) Specific discharge capacity upon cycling at C/5 for ten cycles.

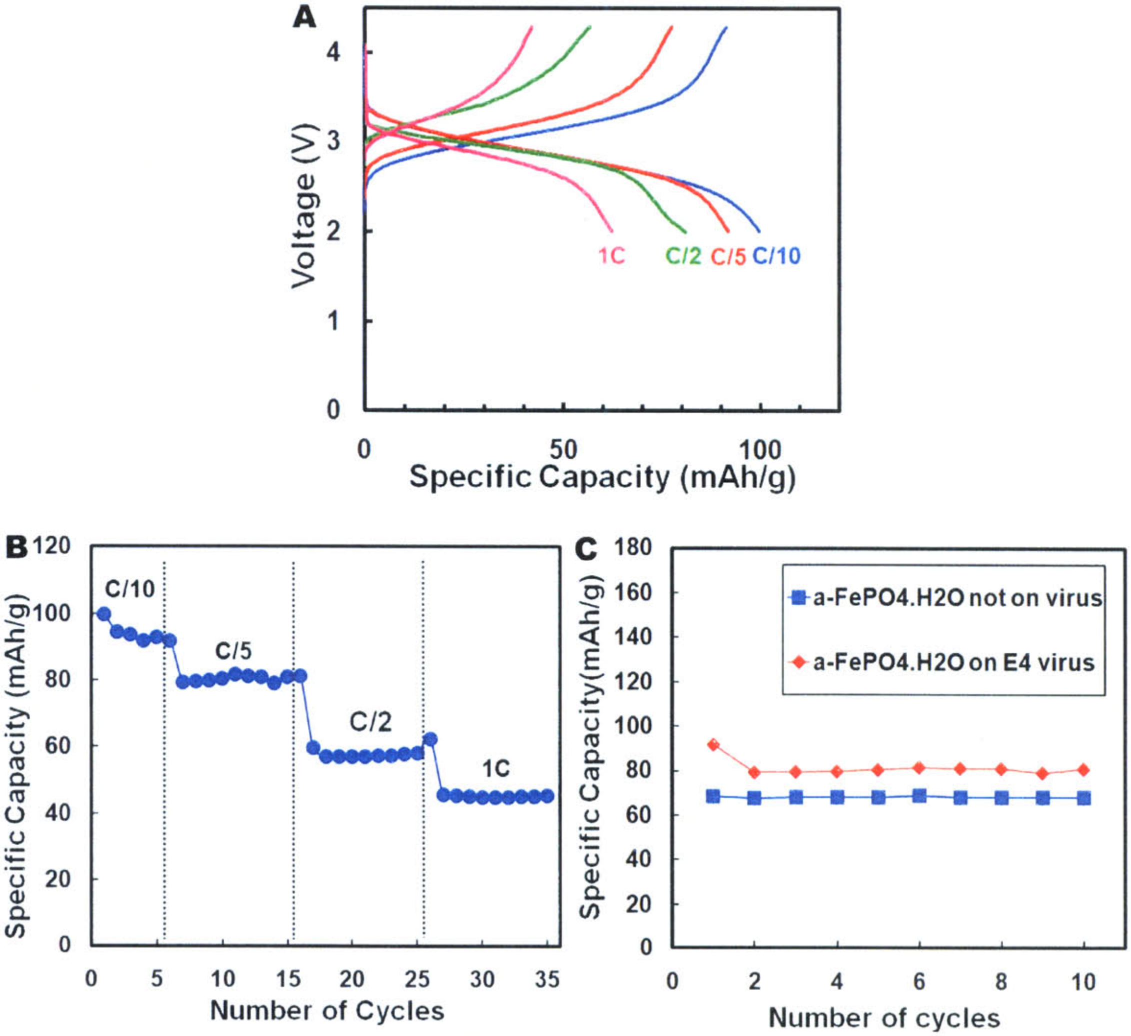

Figure 3.6 Characterization of (Ag)a-$FePO_4 \cdot H_2O$ viral nanowires (A) Transmission Electron Microscope (TEM) images of silver nanoparticles (Ag NPs) grown on E4 viruses. (B) TGA curve of the (Ag)a-$FePO_4 \cdot H_2O$ viral nanowires.

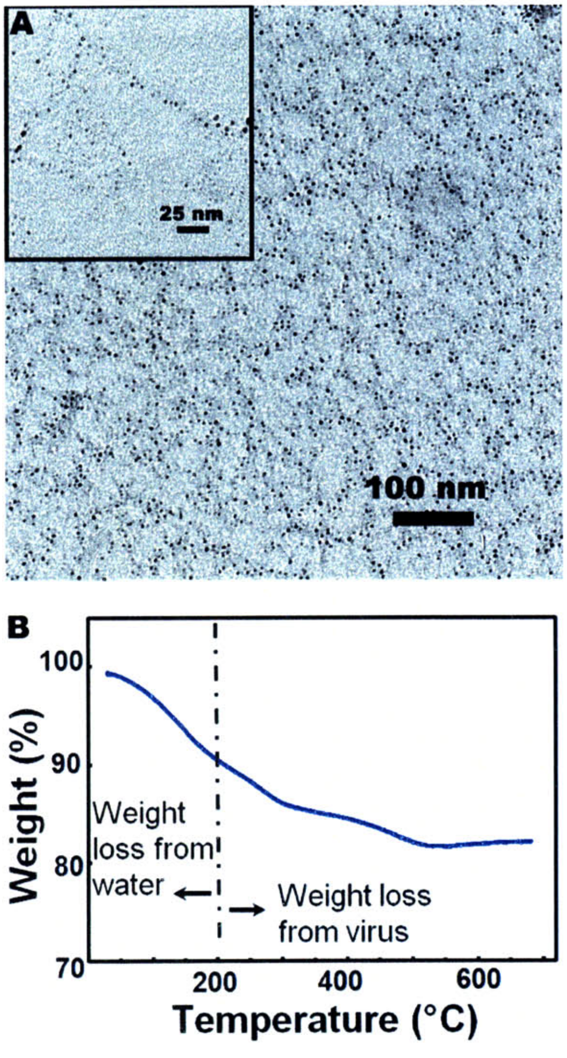

Figure 3.7. Characterization of (AgCl)a-$FePO_4$ nanowires cmplated on E4 virus. (A) TEM images of templated (AgCl)a-$FePO_4$ nanowires on E4 viruses. Inset: Magnified images of the same nanowires. (B) TGA curve of (AgCl)a-$FePO_4$ nanowires synthesized on Ag NPs loaded E4. For comparison, TGA curve of a-$FePO_4 \cdot H_2O$ grown on E4 virus (without Ag NPs) is also presented. Virus content was determined as 19.1 wt% (C) Xray powder diffraction (XRD) of (AgCl)a-$FePO_4$ nanowires on Ag NPs-loaded E4 virus electrode synthesized using $FeCl_3 \cdot 6H_2O$ precursor before and after electrochemical test. The AgCl content was determined to be 5.3 wt% by DCP-AES. After electrochemical testing for 100 discharge/charge cycles at a rate of 1C on the right, part of AgCl was reduced to Ag. Before test, only peaks from AgCl were identified and no peak corresponded to Ag metal, indicating chlorination of Ag NPs.

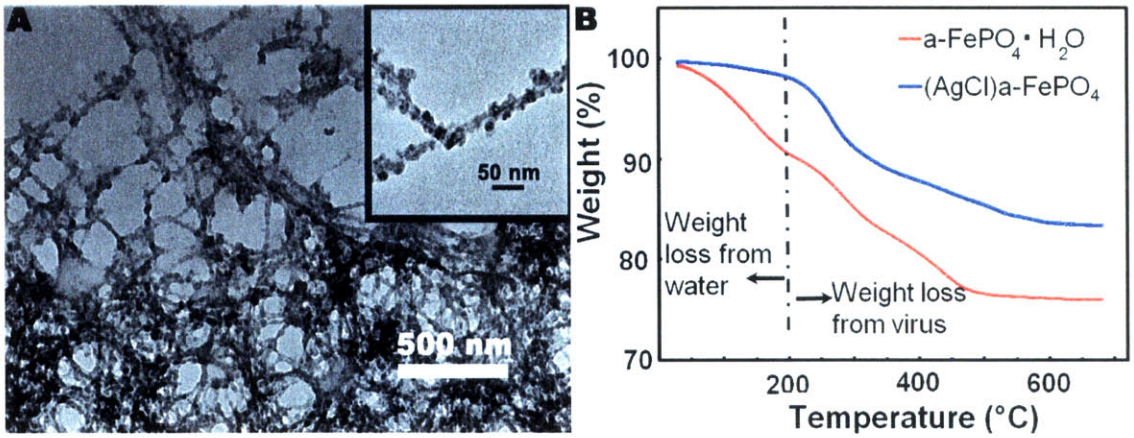

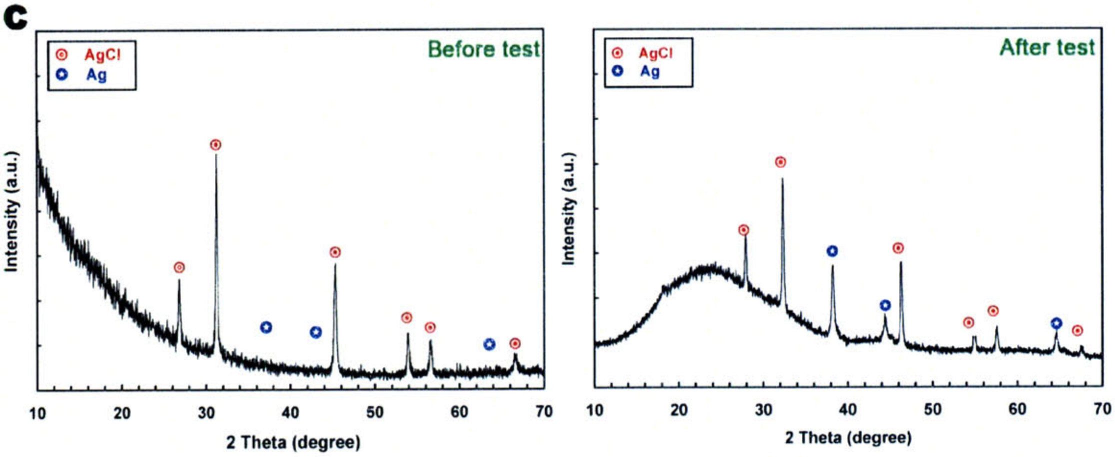
c
AgCl
Ag
Before test
Intensity (a.u.)
10
20
30
40
50
60
70
2 Theta (degree)
AgCl
Ag
After test
Intensity (a.u.)
10
20
30
40
50
60
70
2 Theta (degree)

Figure 3.8. Comparison of discharge capacity of various nanostructured viral cathodes tested between 2.0 and 4.3 V at C/5 rate for ten cycles. Electrodes were prepared with mass ratio of powder tested: Super P carbon: PTFE= 80: 15: 5. Beneficial effect of uniformly distributed conducting naoparticles and dehydration were clearly shown.

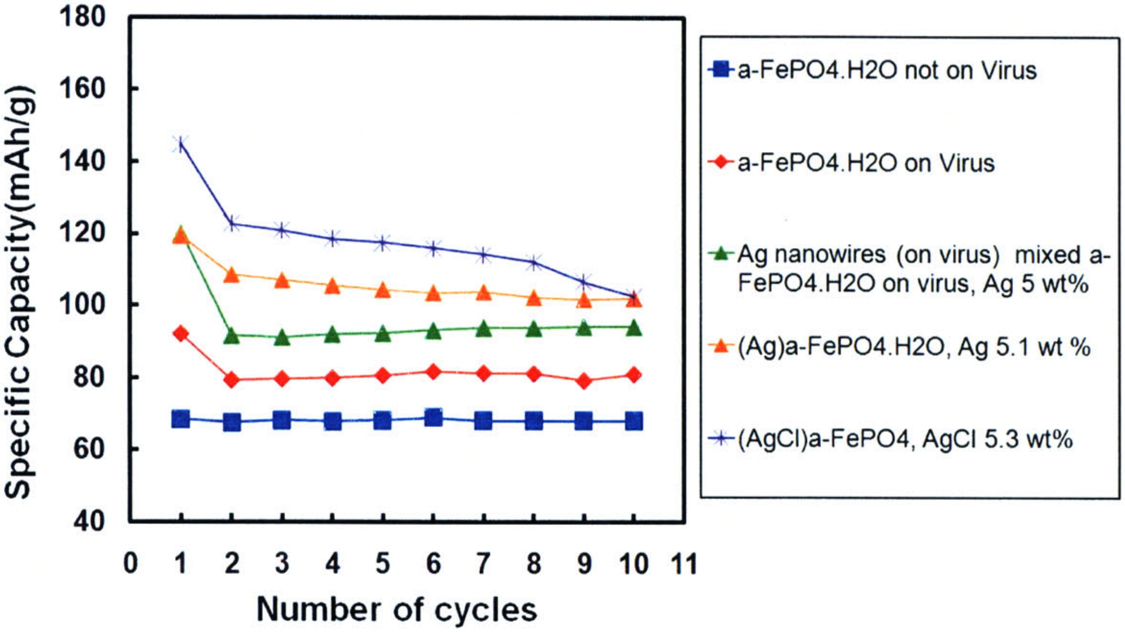

Figure 3.9. Electrochemical performance of heterostructured viral nanowires on E4 tested between 2.0 and 4.3 V. Electrodes were prepared with mass ratio of powder tested: Super P carbon: PTFE= 70: 25: 5. (A) Comparison of specific discharge capacity upon cycling at different rate: C/10, C/5, C/2 and 1C. (B) Rate performance of (AgCl)a-FePO$_4$ viral nanowires and a-FePO$_4$·H$_2$O viral nanowires. (C) Nyquist plot: impedance response of a-FePO$_4$·H$_2$O and (AgCl)a-FePO$_4$ viral nanowires.

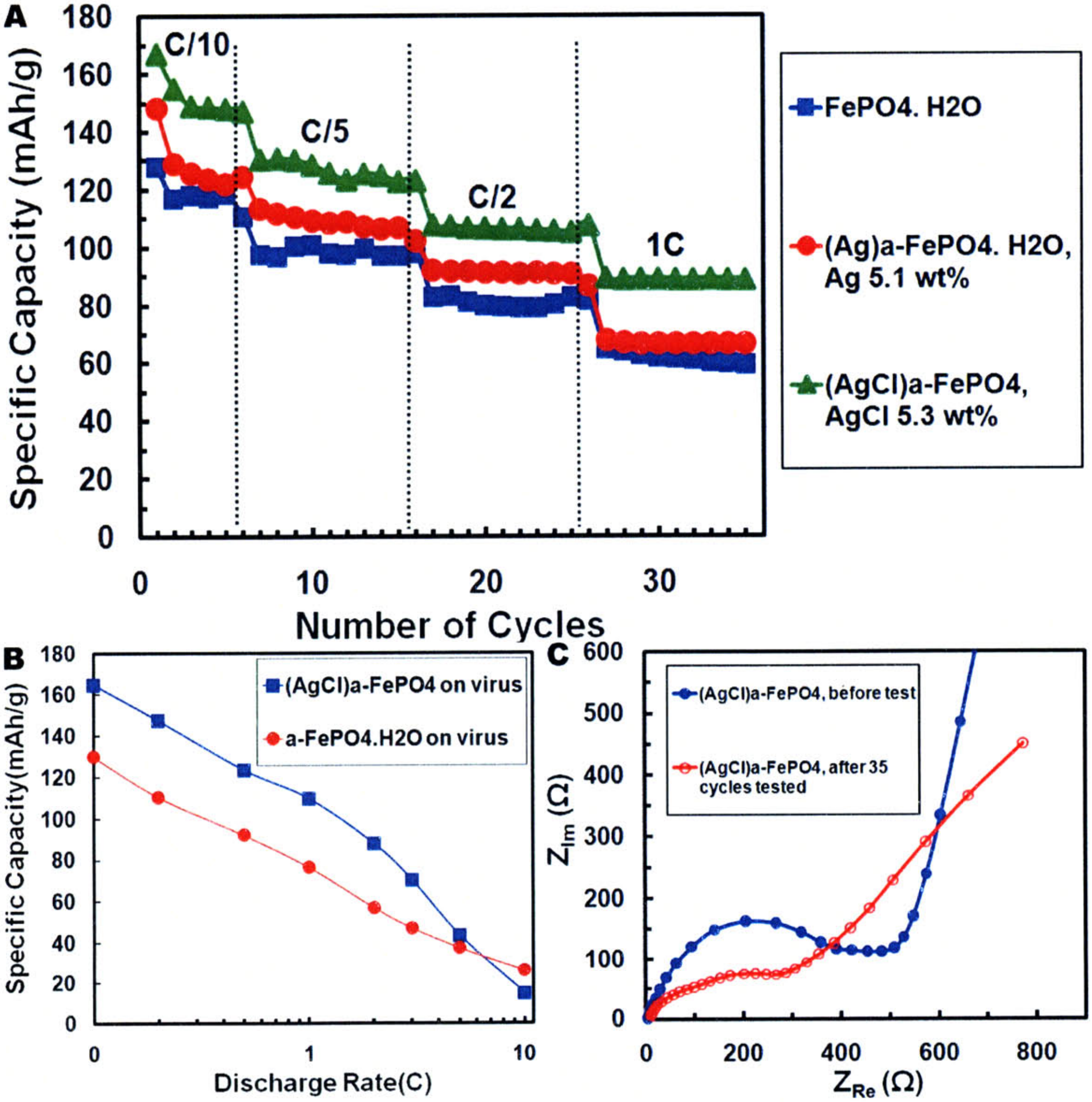

Figure 3.10. Electrochemical power performance of (AgCl)a-$FePO_4$ viral nanowires on E4 tested between 2.0 and 4.3 V. Electrodes were prepared with mass ratio of powder tested: Super P carbon: PTFE= 70: 25: 5. Active materials loading was 2.63 mg/cm^2. (A) First discharge curves at different rates. (B) The Ragone plot representing rate performance in terms of specific power vs specific energy (only active electrode mass included in the weight).

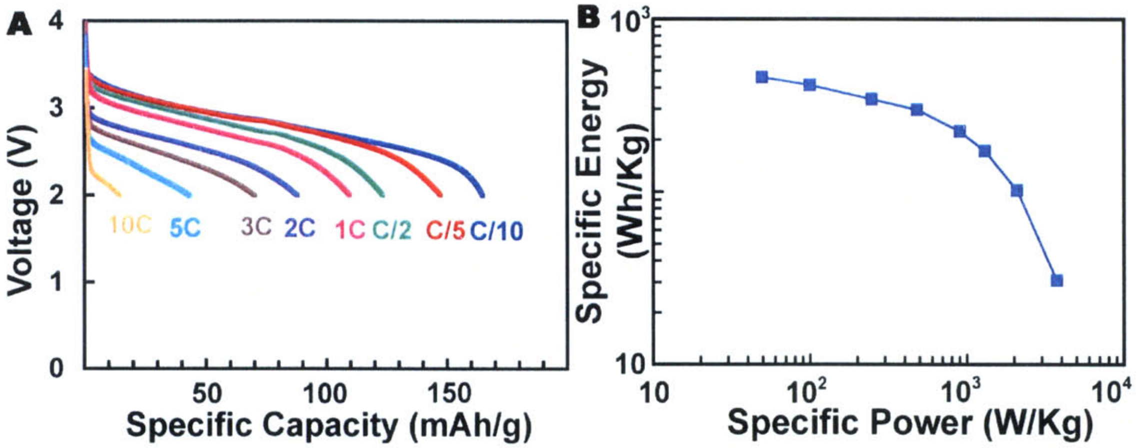

Chapter 4

Fabricating Genetically Engineered High-Power Lithium Ion Batteries Using Multiple Virus Genes

Chapter 4.1 Introduction

In chapter 3, the nanostructuring of a-$FePO_4$ nanowires by the virus enabled an enhanced performance even with one gene system. However, high power performance and capacity retention upon cycling of both the biologically and traditionally synthesized electrodes are still inferior to commercially available c-$LiFePO_4$ cathodes. Since our particles were already 10-20 nm in diameter, our strategy for improved performance was to improve the electronic conductivity in the cathode by achieving better electrical contact between the active materials. Although metallic Ag nanoparticles can locally enhance the electronic conductivity, more important for improved high power performance is a percolating network throughout the electrodes. It is known that incorporation of well-dispersed materials with high conductivity and high aspect ratio leads to efficient percolating networks[66, 67]. Carbon nanotubes (CNTs) have been shown to meet these needs[67], thus well-dispersed single wall CNTs (SWNTs) in water were used. However, conventional composite electrode fabrication processes inevitably suffer from aggregation of carbon particles thereby diminishing contact with the active materials[67]. To achieve better electrical wiring to our biologically derived a-$FePO_4$, a specific affinity was engineered between the conducting material and active material. In designing nanostructured electrodes with better electrical wiring for high power batteries, multifunctionality of the virus is required. Multifunctional viruses have been engineered with desired modifications on different positions of the protein coat[11, 12, 21]. Here we developed a genetically programmed multifunctional virus as a versatile scaffold for the synthesis and assembly of materials for high power batteries. In chapter 4, only anhydrous viral (AgCl)a-$FePO_4$ nanowires were be used and denoted as a-$FePO_4$ nanowires.

Chapter 4.2 Experiment

Phage-display Library Screening As-prepared HiPco (HPR 111.1 from Rice University) single-walled carbon nanotubes (SWNTs) were used in this study. SWNTs were suspended in water with 2 w/v% (w/v%=g/100 ml) sodium cholate surfactants and sonicated, followed by ultra-centrifugation to disperse suspended SWNTs individually in a similar way reported previously[68]. The final concentration of SWNTs-solution was adjusted to be 0.005 w/v%. For the phage-display experiment, SWNTs were prepared in a form of thin films on glass substrates as previously described[69] and a commercially available 12-mer phage-display library kit (Ph.D.-12™ Phage Display Peptide Library Kit, New England Biolabs) was used. In brief, ten microliters of phage-library solution (phages of 1.5×10^{10} with 2.7×10^{9} different sequences) were diluted with 250 μl of Tris-buffered saline (TBS, 100 mM Tris-HCl, 150 mM NaCl, pH 7.5) with different concentration of Tween 20 (TBS-T, Tween 20 concentration of 0.1-0.5 v/v%), applied to SWNTs films and incubated for an hour with gentle rocking. The SWNTs film was rinsed with one milliliter of TBS-T ten times to wash off unbound phages. Bound phages were eluted by incubating with 100 μl of 0.2 M Glycine-HCl, pH 2.2, for eight minutes and carefully transferred into 1.5 ml-microcentrifuge tube and immediately neutralized with 15 μl of 1 M Tris-HCl, pH 9.3. The eluted phages were amplified and the same procedures were repeated for further rounds with increasing Tween 20 concentration. After each round of panning, the numbers of eluted and amplified phages counted as plaque-forming units (PFU) were measured using agar plates containing X-gal/isopropyl-β-D-1-thiogalactopyranoside (IPTG)/tetracycline to set the input number of phage for each round the same. Also plaques from each round were amplified and DNA sequenced.

Binding affinity test In the binding test, phages with the same input number of 5 × 10^8 PFU, diluted with 250 μl of TBST 0.3 (TBS, 100 mM Tris-HCl, 150 mM NaCl, pH 7.5, Tween 0.3 v/v%), were incubated with SWNTs films for one hour with gentle rocking. Then, the SWNTs film was rinsed with one milliliter of TBST 0.3 ten times to remove unbound phages. Bound phages were eluted by incubating with 100 μl of 0.2 M Glycine-HCl, pH 2.2, for eight minutes, carefully transferred into 1.5 ml-microcentrifuge tube and immediately neutralized with 15 μl of 1 M Tris-HCl, pH 9.3. The eluted phage-solutions were serially diluted and plated on agar plates containing X-gal/isopropyl-β-D-1-thiogalactopyranoside (IPTG)/tetracycline. The plates were incubated at 37 °C overnight and the numbers of eluted phages were counted as PFU from blue plaques.

Genetic engineering of multifunctional M13 phage For the E4 phage, tetraglutamic acids were engineered onto the N-terminus of pVIII protein of M13 as previously described[18]. The oligonucleotide pairs used for EC#1 and EC#2 were were 5’-GTACCTTTCTATTCTCACTCTCATGGTCATCCGTATCAGCATCTTCTGCGTGTGCTGGGTGGAGGTTC-3’, 5’GGCCGAACCTCCACCCAGCACACGCAGAAGATGCTGATACGGATGACCATGAGAGTGAGAATAGAAAG-3’ and 5’-GTACCTTTCTATTCTCACTCTGATATGCCGCGTACTACTATGTTCCGCCGCCGCGTGGTGGAGGTTC-3’, 5’-GGCCGAACCTCCACCACGCGGCGGCGGAGACATAGTAGTACGCGGCATATCAGAGTGAGAATAGAAAG-3’, respectively. The oligonucleotides were synthesized, phosphorylated (Operon Biotechnologies) and annealed to form DNA duplexes. The E4-phage vectors were extracted from E4 phage using miniprep kit (QIAprep Miniprep, QIAGEN) and double-digested with Acc65 I and Eag I. Double-digested vectors were purified by means of agarose-gel electrophoresis, dephosphrylated with Antarctic phosphatase and ligated with DNA duplexs. (All enzymes were purchased from New England Biolabs. Inc.) Ligated vectors were electrotransformed into XL-1 blue electrocompetent cells (Stratagene) and incubated at 37 °C for an hour and plated. The inserted gVIII and gIII genes were confirmed by DNA sequencing. DNA sequencing was done at MIT Biopolymers lab.

Synthesis of virus-based electrode The genetically engineered viruses were amplified using *Escherichia coli* bacterial medium and purified by standard PEG/NaCl precipitation method. For the anhydrous a-$FePO_4$ synthesis, 1 ml virus solution in 0.1 M TBS buffer ($2x10^{11}$ PFU/ml) was dialyzed against pH=9.5 water overnight, followed by incubation with 1 mM, 1 ml silver acetate ($AgOOCCH_3$) solution for 12 hours in the dark at room temperature. All solutions were aqueous after the virus dialysis. The Ag NPs were formed by reducing with 5 mM, 1 ml sodium borohydride ($NaBH_4$) for 4 hours at room temperature. This Ag NPs-loaded virus solution was dialyzed against pure water (Millipore Milli-Q, 18.2 MΩ-cm) at room temperature to remove remaining ions. The Ag NPs-loaded E4 structure was incubated with 1.33 mM, 9 ml $FeCl_3 \bullet 6H_2O$ to have final concentration of 1 mM for 24 hours at 4°C in order to suppress hydrolysis of Fe^{+3} ions into oxide/hydroxide. Amorphous iron phosphate nanowires were produced after reacting with 1 mM, 12 ml Na_3PO_4 at pH=7.5 for 24 hours at 4 °C. The resulting viral nanowires were collected through filtration and washed with water and acetone. For viral a-$FePO_4$/SWNTs hybrid nanowires synthesis, viral a-$FePO_4$ suspension was reacted with the SWNTs suspended in water with 2 w/v% sodium cholate (SC) surfactants for 3 hours. The final solution was filtered and washed with water and acetone. The collected powder was dried in 100 °C vacuum oven overnight.

Structural and Chemical analysis The microstructure of nanowires was analyzed with Transmission Electron Microscopy (JEOL 200CX TEM and JEOL 2010F TEM). For TEM analysis, solutions were dropped on copper grids, washed with distilled water several times and dried. For high-resolution TEM (HRTEM) imaging, surfactants were removed by washing with acetone. Chemical composition was determined by DCP-AES (Luvak, Boylston, MA). For Thermo Gravimetric Analysis (TGA), a RGA Q50 (TA instrument) apparatus was used. Samples placed on a platinum pan were preheated to 100 °C and held for 5 min to remove surface absorbed water. After cooling down to 30°C, samples were heated to 700 °C at a heating rate of 10 °C /min in 90 ml/min nitrogen flow and 10 ml/min helium flow. X-Ray Diffraction (XRD) was done using Cu K_α radiation and a Rigaku RU300 powder diffractometer.

Electrochemical tests For positive electrodes preparation, viral a-$FePO_4$ nanowires were mixed with Super P (TIMCAL, SUPER P® Li) carbon black and polytetrafluoroethylene (PTFE) binder in a mass ratio of 70: 25: 5. The detailed mass ratio of each component in electrodes is a-$FePO_4$: Super P carbon: PTFE: virus: AgCl = 52.9: 25: 5: 13.4: 3.7. In case of viral a-$FePO_4$/SWNTs hybrid electrodes, the mixing ratio was 90: 5: 5. The detailed mass ratio of each component in electrodes are: (i) for 5 wt% SWNT samples, a-$FePO_4$: virus: AgCl :SWNT: Super P carbon: PTFE: = 64.6: 16.4: 4.5: 4.5: 5: 5. (ii) for 10 wt% SWNT samples, a-$FePO_4$: virus: AgCl :SWNT: Super P carbon: PTFE: = 61.2: 15.5: 4.3: 9: 5: 5 The mixture was roll milled and punched into disks with diameters of 8 mm. Typical electrode thickness was 20 to 40 μm. The cell was assembled in an argon filled glove box using lithium foil as a negative electrode, a microporous polymer separator (Celgard 3501™) and liquid electrolyte mixtures of 1 M $LiPF_6$ in ethylene carbonate: dimethyl carbonate (EC: DMC) = 1: 1 in volume ratio (Ferro Corporation). The testing cell was a coin cell configuration. The assembled cell was galvanostatically tested using a Solatron Analytical 1470E potentiostat. Rates are reported in C-rate convention, where

C/n is the rate (current per gram) corresponding to complete charging or discharging to the theoretical capacity of the materials in n hours. Here, 1C corresponds to 178 mA/g.

Chapter 4.3 Result and Discussion

Since the major coat protein of the E4 virus serves only as a template for a-$FePO_4$ nanowires growth, additional genetic modification was required to engineer the E4 virus to have a binding affinity for SWNTs. In this context, the p3 protein (pIII), a minor coat protein located at one end of the virus (Fig. 4.1A), is an ideal tool since gene III can be independently controlled from gene VIII to insert foreign DNA encoding pIII-displayed peptides. Moreover, the peptide sequences identified through the phage-display with a pIII phage-display library can be directly inserted into the E4 virus without losing functionality[12]. Therefore, phage-display experiments to search for peptide sequences with a strong binding affinity for SWNTs were done first, and then genetic engineering into the E4 virus to produce a multifunctional virus structure. Several consensus sequences were obtained from separate phage-display screening experiments. Among them, sequences N'-HGHPYQHLLRVL-C', named as MC#1, and N'-DMPRTTMSPPPR-C', as MC#2, were selected for further experiments. The sequence MC#1 started with histidine (H), whose appearance in the first position was often observed in CNTs-binding sequences[70]. Also it contained several aromatic residues (H and Y), which were expected to favorably bind to graphene surface via π-stacking interaction[71]. The sequence MC#2 is quite different from MC#1 and the clone MC#2 showed approximately four times higher binding affinity than the clone MC#1 whose binding affinity is already two and a half times higher than wild-type M13KE in the binding affinity tests[72] (Fig. 4.1B and C). Binding affinity was measured by the number of plaque-forming units (PFU). The PFU number is proportional to the binding affinity.[73] The strong binding of the sequence MC#2 can be explained by the location of the hydrophobic segments of the sequence. The calculated hydrophobicity plot (Fig. 4.2) shows a tri-block structure with hydrophilic regions on both ends and the hydrophobic region in the middle of the sequence. The plot was based on Hopp-Woods scale with the averaging group length of five[74]. It has been demonstrated that a tri-block structure of hydrophilic/hydrophobic/hydrophilic polymers worked well to suspend SWNTs[70, 75].

To genetically engineer E4 virus as a multifunctional biological platform, the selected sequences, MC#1 and MC#2, were independently fused onto the amino-terminal portion of the pIII of E4 virus, producing clones EC#1 and EC#2 respectively. Since two genes (gIII and gVIII in Fig. 4.1A) have been engineered with desired modification on both pIII and pVIII proteins, we called it a two-gene system.

A schematic diagram for constructing the genetically engineered high power lithium ion battery using the multifunctional two-gene virus system is illustrated in Fig. 4.3. All viruses were loaded with Ag NPs and $FeCl_3 \cdot 6H_2O$ was used as a precursor to synthesize anhydrous a-$FePO_4$. Formation of anhydrous a-$FePO_4$ on the pVIII preceded the interaction with SWNTs. The synthesis procedure of anhydrous a-$FePO_4$ nanowires on the multifunctional viruses was the same for the growth on the one-gene system in chapter 3. Viral a-$FePO_4$ solutions were then incubated with the SWNT suspensions to form a-$FePO_4$/SWNTs hybrid nanostructures. The photograph in Fig 4.3 is the actual assembled lithium ion battery powering a light emitting diode (LED) using Li metal as a negative electrode. The virus-enabled high power battery could power a green LED with a small amount of active materials loading of 3.21 mg/cm^2.

The morphology of hybrid a-$FePO_4$/SWNTs nanowires on the EC#2 virus is shown in Fig. 4.4 C-E. In the high-resolution TEM image (Fig. 4.4E and F), 6~8 SWNTs are bundled with diameters of 4-5 nm. The TEM images show that a-$FePO_4$ nanowires templated on the multifunctional virus were tethered to SWNTs mainly through the pIII attachment, however, they made multiple contacts with neighboring SWNTs due to close positioning. To explore the effect of specificity, we also mixed the one-gene system (E4) viral nanowires solution with SWNTs. Most viral a-$FePO_4$ nanowires on E4 did not make contact with SWNTs, and even if they did, the contact did not seem to be specific binding with SWNTs (Fig. 4.5). Moreover, SWNTs aggregated by themselves when there was no specific binding affinity on pIII, suggesting that SWNTs specific viruses enhanced dispersion of SWNTs in solution. Similar observation has been reported showing that SWNTs specific peptides can disperse SWNTs while non-specific pepetides cannot[70].

The electrochemical properties of viral a-$FePO_4$/SWNTs hybrid materials with 5 wt% SWNTs were evaluated and compared. (Fig. 4.6 and Fig 4.7) Positive electrodes were prepared by mixing viral a-$FePO_4$/SWNTs hybrid composites with Super P® carbon black and PTFE binder in a mass ratio of 90: 5: 5. The addition of 5 wt% extra carbon was used to increase the total volume making the powder easier to handle. Without extra carbon, the electrodes showed slightly higher polarization at high rates, but the difference was not substantial. As demonstrated in the first discharge profiles (Fig. 4.6A and Fig. 4.7A for full discharge/charge curves), electrochemical performances show remarkable improvement as the binding affinity to the SWNTs increases. Specific capacity at a low discharge rate of C/10 increased from 143 mAh/g (E4) to 160 mAh/g with EC#1 and to 170 mAh/g with EC#2. The performance improvement is more pronounced at higher rates. Discharge profiles of the two-gene system show much lower polarization and maintain much higher capacity than those of the one-gene system at high rates. When compared with the best reported capacity for a-$FePO_4$ at a high rate of 3C (80 mAh/g)[60], EC#2 showed a capacity of 134 mAh/g confirming substantially improved high power performance. Moreover, when we cycled EC#2 between 1.5 and 4.3 V, the first discharge capacity at 10C reached 130 mAh/g. No published data for a-$FePO_4$ is available to compare with at a rate higher than 3C, but this capacity value obtained for the two-gene system is comparable to the capacity from state-of-the-art c-$LiFePO_4$. The power performance of the multifunctional virus based cathode was further compared using a Ragone plot. Fig. 4.6B shows that two-gene system based materials delivered much higher energy than the one-gene system at high power. At a specific power of 4000 W/kg (approximately corresponds to a rate of 10C), the energy density of EC#1 and EC#2 was two times and three times higher respectively than that of E4. Again, the high power performance scales with binding affinity. In Fig. 4.6B inset, rate performance of E4 virus based cathodes with either Super P carbon or SWNTs were tested. It is well known that well-dispersed SWNTs by themselves make better electrical wiring to active materials due to better percolation networks than carbon black powders[67], confirming the importance of nanoscale electrical wiring. Figure 4.6C shows stable capacity retention of a-$FePO_4$/SWNTs hybrid electrodes upon cycling at 1C. Up to 50 cycles, there was virtually no capacity fade observed. A slight capacity loss after the first cycle is a characteristic of a-$FePO_4$ materials[60, 61]. When cycled at C/10 rate again after the sample was tested for several cycles at rates from C/10 to 10C, the original capacity was recovered confirming structural stability (Fig. 4.7B). Structural stability of viral a-$FePO_4$/SWNTs hybrid nanostructures was induced by materials specific binding and stiff/robust carbon nanotubes and brought about excellent retention at low SWNTs content of 5 wt%. Electrochemical test results of a-$FePO_4$/SWNTs hybrid electrodes with 10 wt% SWNTs are shown in Fig. 4.8. As shown in full discharge/charge curves at rates from C/10 to 10C (Fig 4.8A), electrochemical property improved slightly with the increase of SWNTs content from 5 wt% to 10 wt% for clone EC#2. Specific capacity at C/10 rate was 177 mAh/g and that of 10C was 126 mAh/g (For SWNTs 5 wt%: specific capacity at C/10= 170 mAh/g, at 10C = 114 mAh/g). However, the electrochemical performance improvement with SWNTs content was more remarkable for E4 virus. When compared with Fig. 4.7A, a-$FePO_4$/SWNTs hybrid electrodes on E4 virus showed much less polarization along with discharge capacity increase with the increase of SWNTs contents from 5 wt% to 10 wt%. The power performance changes with SWNTs content were also compared using a Ragone plot. (Fig. 4.8B) For two-gene system EC#2 clone, the specific power vs energy curve just slightly moved up while that of one-gene system E4 clone showed substantial improvement. At a specific power of ~4000 W/Kg (corresponding to a rate of ~10C), the energy density increases about twice with the increase of SWNTs content from 5 wt% to 10 wt%. In accordance with the Ragone plot, the specific discharge capacity upon cycling at different rates of C/10, 1C, 10C and C/10 in Fig 4.8C showed much substantial improvement in discharge capacity and cycleabiltiy for E4 clone with the increase of SWNTs content. These results indicate that the specific binding site of two-gene system virus with SWNTs could be already saturated with 5 wt% SWNTs and further addition of SWNTs only slightly increased electrochemical performance of the system. Since one-gene system E4 virus has no specific affinity for SWNTs, the increase of SWNTs content could give higher chance to make intimate electrical contact with a-$FePO_4$ active materials leading remarkable improvement in electrochemical performance.

Chapter 4.4 Conclusion

There have been efforts to electrically address electrode materials with poor electronic conductivity through nanoscale wiring of active materials[59, 76, 77]. However, the wiring tools used so far were functionalized for a single component, either active materials[59, 77] or conducting materials[76]. The wiring did not completely exploit specificity but depended on random occurrence of contacts between either conducting networks or active materials. By developing this two-gene system with a universal handle to pick up electrically conducting carbon nanotubes, we facilitated a method to realize nanoscale electrical wiring for high power lithium ion batteries using basic biological principles. This biological scaffold could further extend possible sets of electrode materials by activating classes of materials that have been excluded because of their extremely low electronic conductivity. This versatile platform could also be conjugated with Li-containing positive electrodes, which is underway in our lab. Since the density of SWNTs is 1.33 g/cm^3 [67], it would decrease the volumetric energy density of the hybrid electrodes. However, although we adopted SWNTs to show that we can do nanoscale wiring by using genetic engineering, we expect that we could optimize the fraction of the conducting additives by using even better conducting nanowires with high aspect ratio and higher density.

Chapter 4.5 Figures

Figure 4.1. Biological toolkits: genetic engineering and biomolecular recognition. (A) A schematic presentation of the multifunctional M13 virus is shown with its important proteins genetically engineered in this study. The gene VIII protein (pVIII), a major capsid protein of the virus, is modified to serve as a template for a-$FePO_4$ growth and the gene III protein (pIII) is further engineered to have a binding affinity for single-walled carbon nanotubes (SWNTs). (B) Binding affinity for single-walled nanotubes (SWNTs) of various phages with different peptide inserts on the pIII was measured by the number of plaque-forming units (PFU). The M13KE has no insert on its pIII while phage clones MC#1 and MC#2 display peptides N'-HGHPYQHLLRVL-C' and N'-DMPRTTMSPPPR-C' on the pIII, respectively. (C) Digital camera images of the titration result. The individual blue plaques correspond to bacteria infected by one active phage particle and the number of plaques gives the count of active phage particles (shown in Fig. 4.1C).

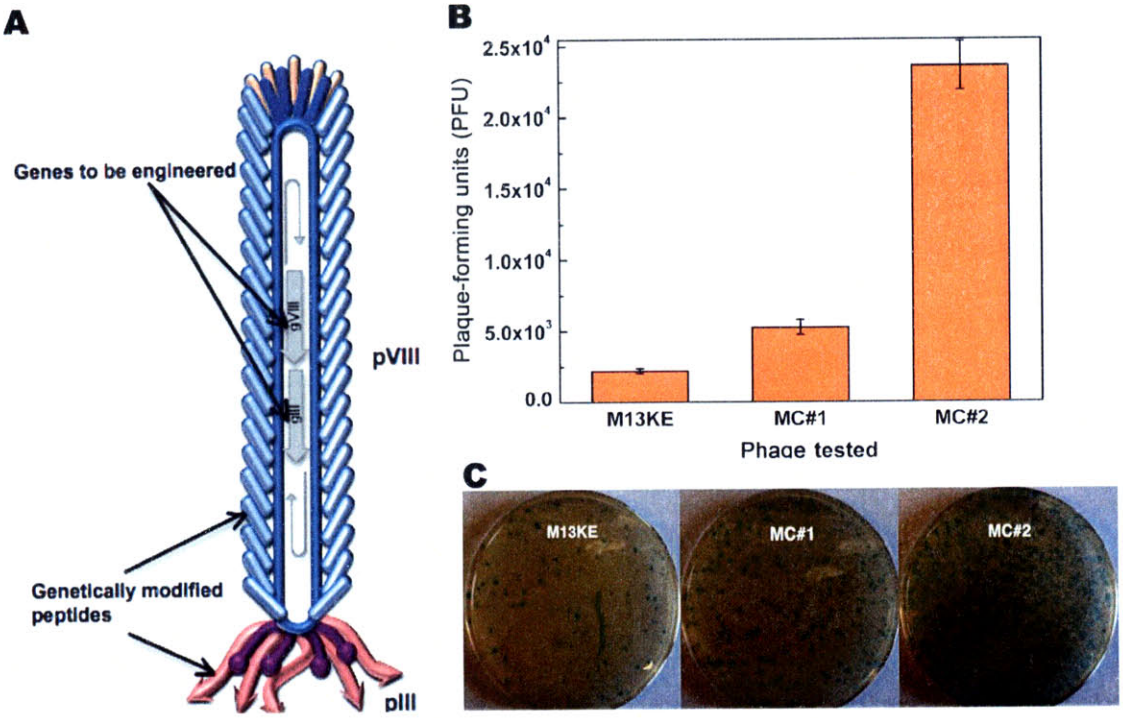

A
Genes to be engineered
gVIII
gIII
pVIII
Genetically modified peptides
pIII
B
Plaque-forming units (PFU)
2.5x10^4
2.0x10^4
1.5x10^4
1.0x10^4
5.0x10^3
0.0
M13KE
MC#1
MC#2
Phage tested
C
M13KE
MC#1
MC#2

Figure 4.2. Hydrophobicity as a function of amino acid location of the sequence EC#2, N'-DMPRTTMSPPRC'. Here positive values correspond to hydrophobic regions while negative values represent hydrophilic regions. The hydrophobicity plot shows a tri-block structure with hydrophilic regions at both ends of the sequence. Here a three glycines (GGG)-linker sequence was also considered to fully calculate the hydrophobicity.

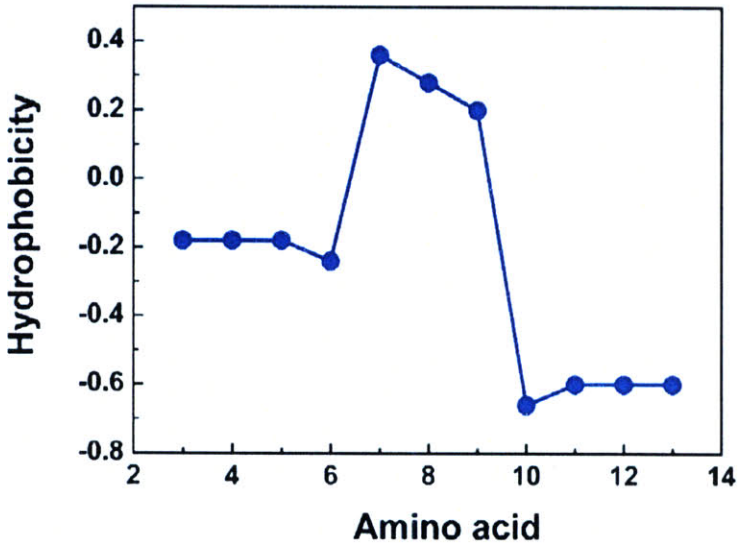

Figure 4.3 Schematic diagram for fabricating genetically engineered high-power lithium ion battery cathodes using multifunctional viruses (two-gene system) and a photograph of the battery used to power a greed LED. The biomolecular recognition and attachment to conducting SWNT networks make efficient electrical nanoscale wiring to the active nanomaterials enabling high power performance. These hybrid materials were assembled as a positive electrode in a lithium ion battery using lithium metal foil as a negative electrode to power a green LED. Active cathode materials loading was 3.21 mg/cm^2. The 2016 coin cell which is 2 cm in diameter and 1.6 mm in thickness was used. LED power dissipation was 105 mW.

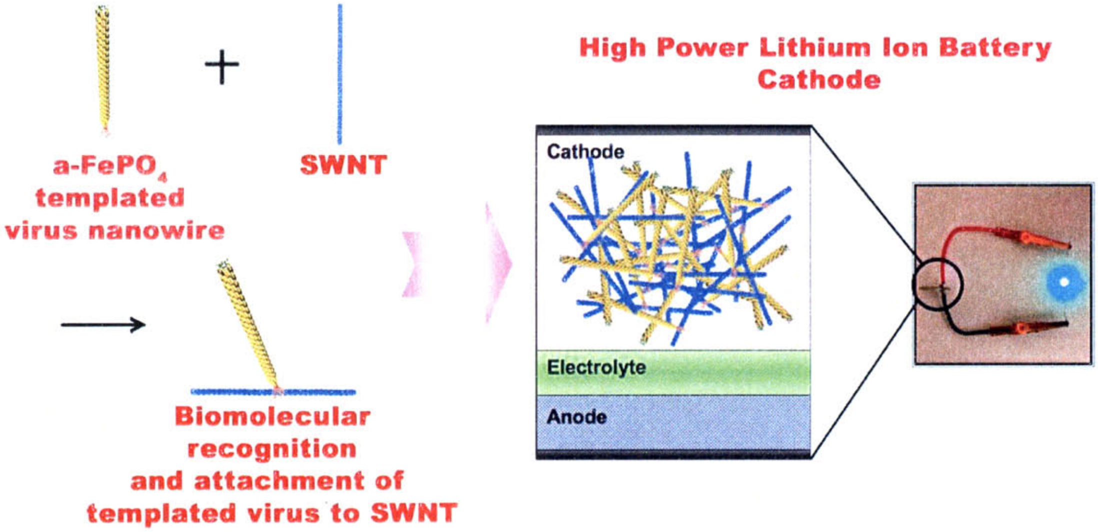

Figure 4.4. Morphology of the a-$FePO_4$ grown on the multifunctional viruses/SWNTs hybrid nanostructures. TEM images of the following. (A) a-$FePO_4$ nanowires templated on EC#2 viruses (before interacting with SWNTs). EC#2 virus is a two-gene system virus with the strongest binding affinity to SWNTs. (B) SWNTs only (before interacting with viral a-$FePO_4$). (C)-(E), a-$FePO_4$ grown on EC#2 attached to SWNTs. (C) Low magnification (10,000). (D) Higher magnification (30,000). (E)-(F) High resolution TEM (HRTEM) images (800,000). For HRTEM imaging, surfactants were removed by washing with acetone. Material specific tethering of the viral a-$FePO_4$ to the SWNTs is visualized. Amorphous nature of $FePO_4$ was also confirmed.

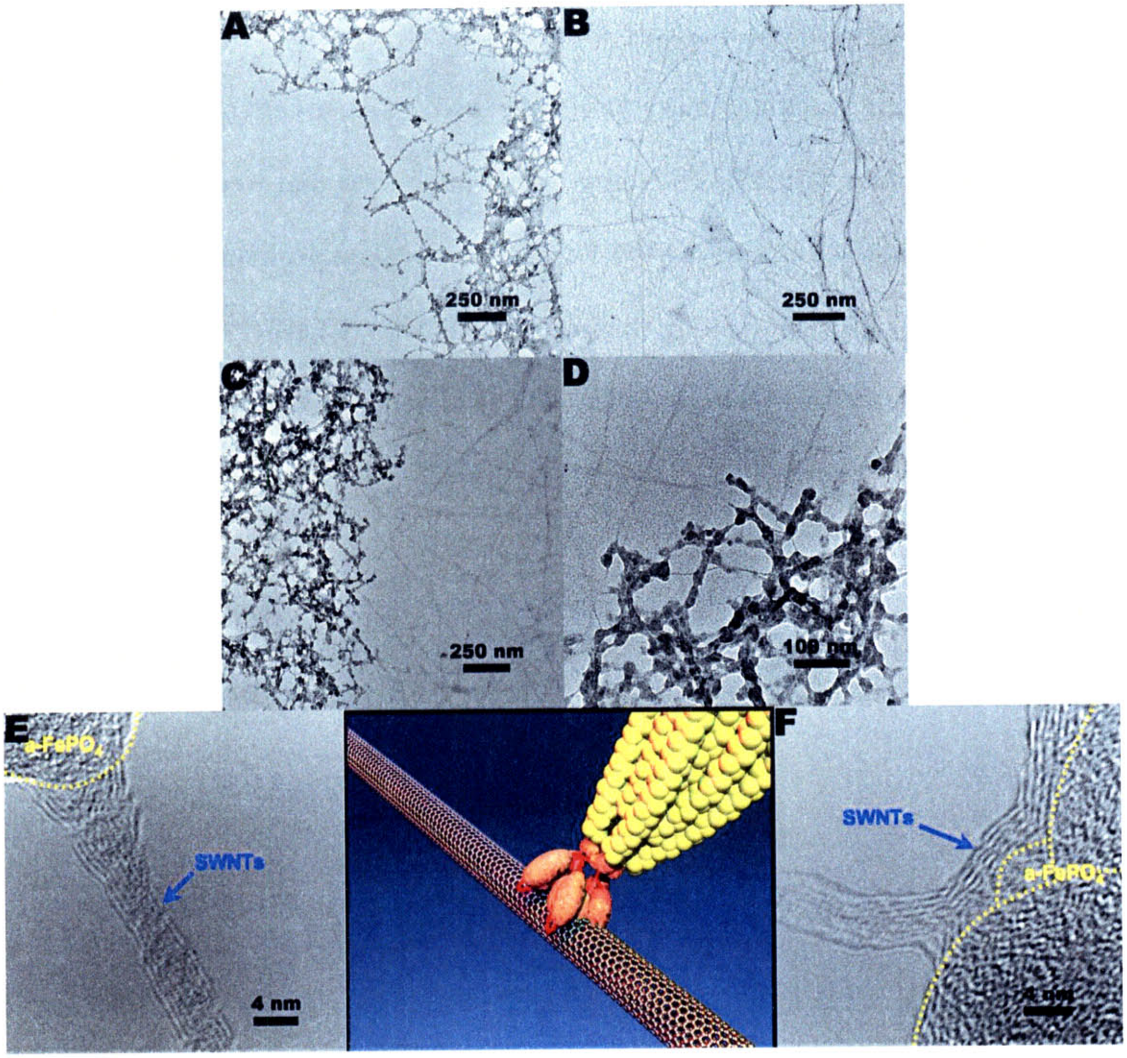
A
250 nm
B
250 nm
C
250 nm
D
100 nm
E
a-$FePO_4$
SWNTs
4 nm
F
SWNTs
a-$FePO_4$
4 nm

Figure 4.5. TEM images of the one-gene system a-$FePO_4$ viral nanowires that were mixed with SWNTs without specific affinity (E4 virus used). (A) a-$FePO_4$ nanowires did not appear to make contact with SWNTs. (B) a-$FePO_4$ nanowires that were in close proximity to SWNTs but do not contact with SWNTs. Most a-$FePO_4$ morphologies were similar to images in Fig. 4.5A and B not making contact with SWNTs. (C) a-$FePO_4$ nanowires seen in contact with aggregated SWNTs bundles. SWNTs were not well dispersed but were aggregated with each other.

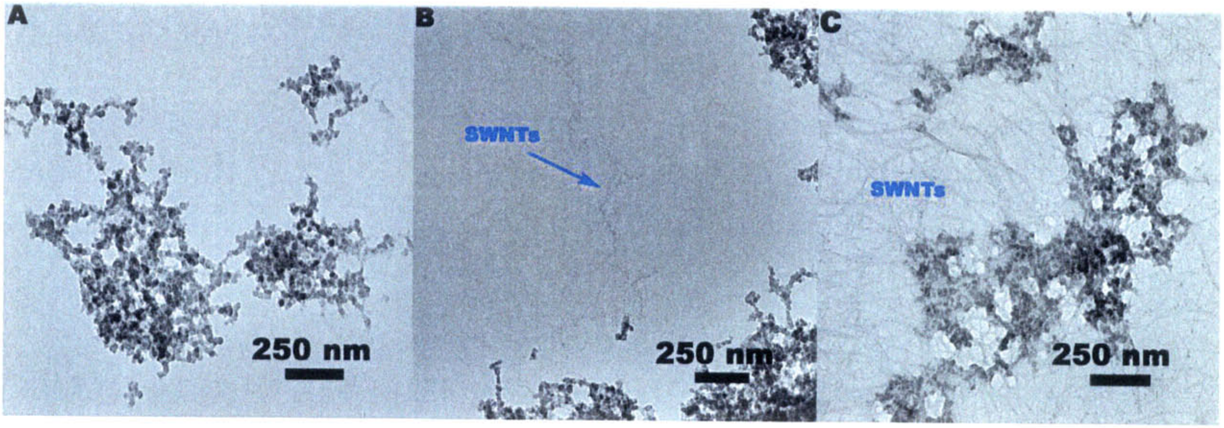

Figure 4.6. Electrochemical properties of the a-$FePO_4$ viral nanowires in two-gene systems tested between 2.0 and 4.3 V. Rate capabilities and capacity retention upon cycling of the a-$FePO_4$ nanowires/SWNTs hybrid electrodes templated on different clones are presented. SWNTs content was 5 wt% for all electrodes. (A) First discharge curves at different rates. Active materials loading were E4: 2.34 mg/cm^2, EC#1: 2.31 mg/cm^2, EC#2: 2.62 mg/cm^2. (B) Ragone plot showing improvement in high power performance with higher binding affinity towards SWNTs (only active electrode mass included in the weight). Inset: Comparison of rate capability of E4 virus based cathodes with either Super P carbon or SWNTs. Electrode with well-dispersed SWNTs even with much smaller amount exhibited improved rate performance due to better percolation networks than carbon black powders. (C) Capacity retention for 50 cycles at 1C rate. There was no obvious fading for at least 50 cycles. Active materials loading were E4: 2.90 mg/cm^2, EC#1: 2.22 mg/cm^2, EC#2: 2.27 mg/cm^2.

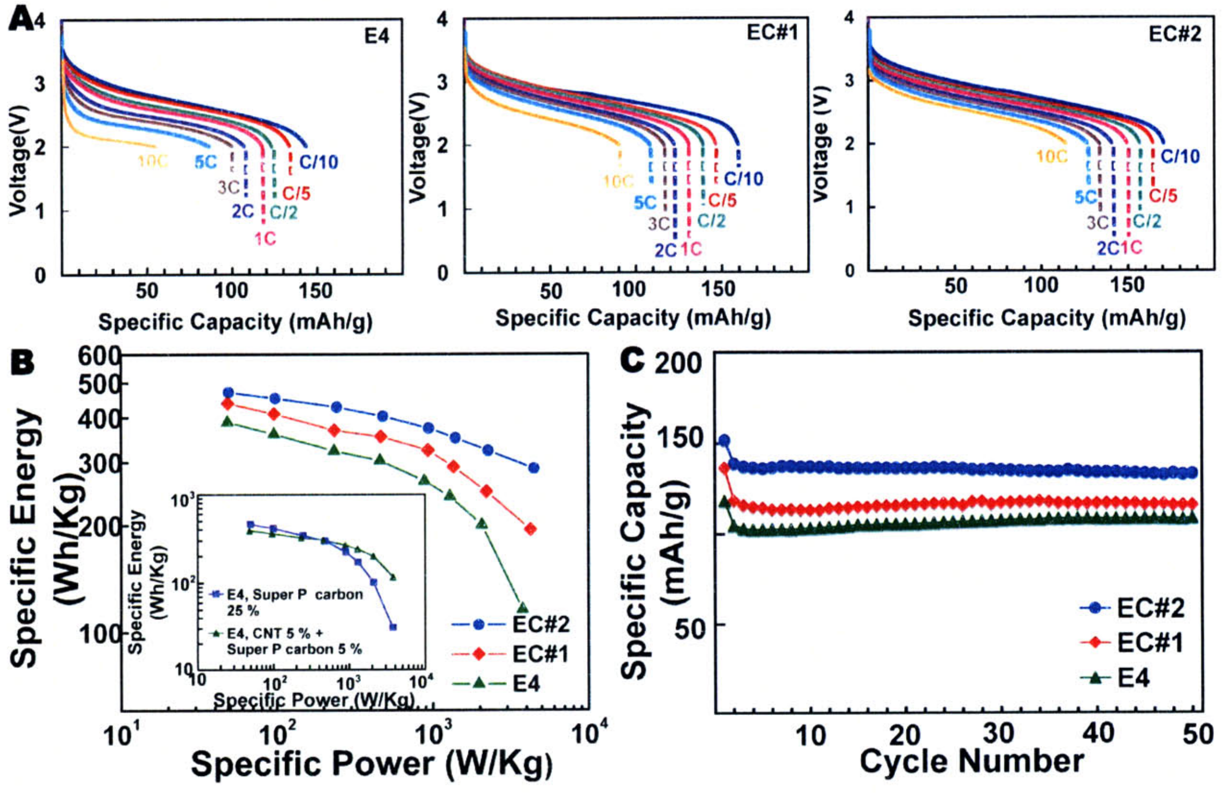

Figure 4.7. Electrochemical properties of the a-$FePO_4$ viral nanowires in two-gene systems tested between 2.0 and 4.3 V. All a-$FePO_4$/SWNTs hybrid materials had 5 w% SWNTs. Active materials loading were E4: 2.34 mg/cm^2, EC#1: 2.31 mg/cm^2, EC#2: 2.62 mg/cm^2. (A) Full discharge/charge curves at rates of C/10, 1C and 10C. (B) Specific discharge capacity upon cycling at different rates; C/10, 1C, 10C and C/10. Electrodes using multifunctional viruses showed stable capacity retention upon cycling and recovery of original high capacity when cycled at C/10 rate again.

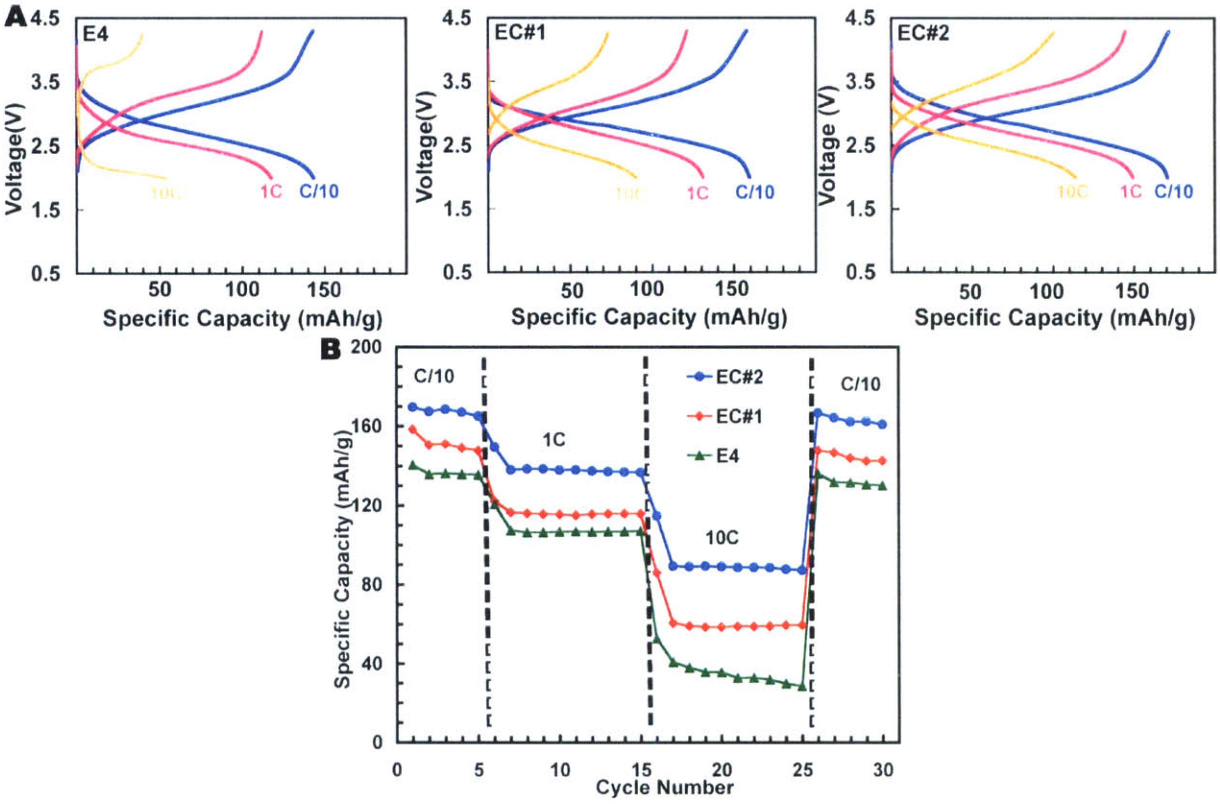

Figure 4.8. Electrochemical properties of the a-$FePO_4$ viral nanowires in two-gene systems tested between 2.0 and 4.3 V. (A) Full discharge/charge curves at rates from C/10 to 10C. All a-$FePO_4$/SWNTs hybrid materials had 10 w% SWNTs. Active materials loading were E4: 2.10 mg/cm^2, EC#2: 2.30 mg/cm^2. (B) Ragone plot showing high power performance of a-$FePO_4$ viral nanowires with different binding affinity to SWNTs and different SWNT contents. (C) Specific discharge capacity upon cycling at different rates; C/10, 1C, 10C and C/10.

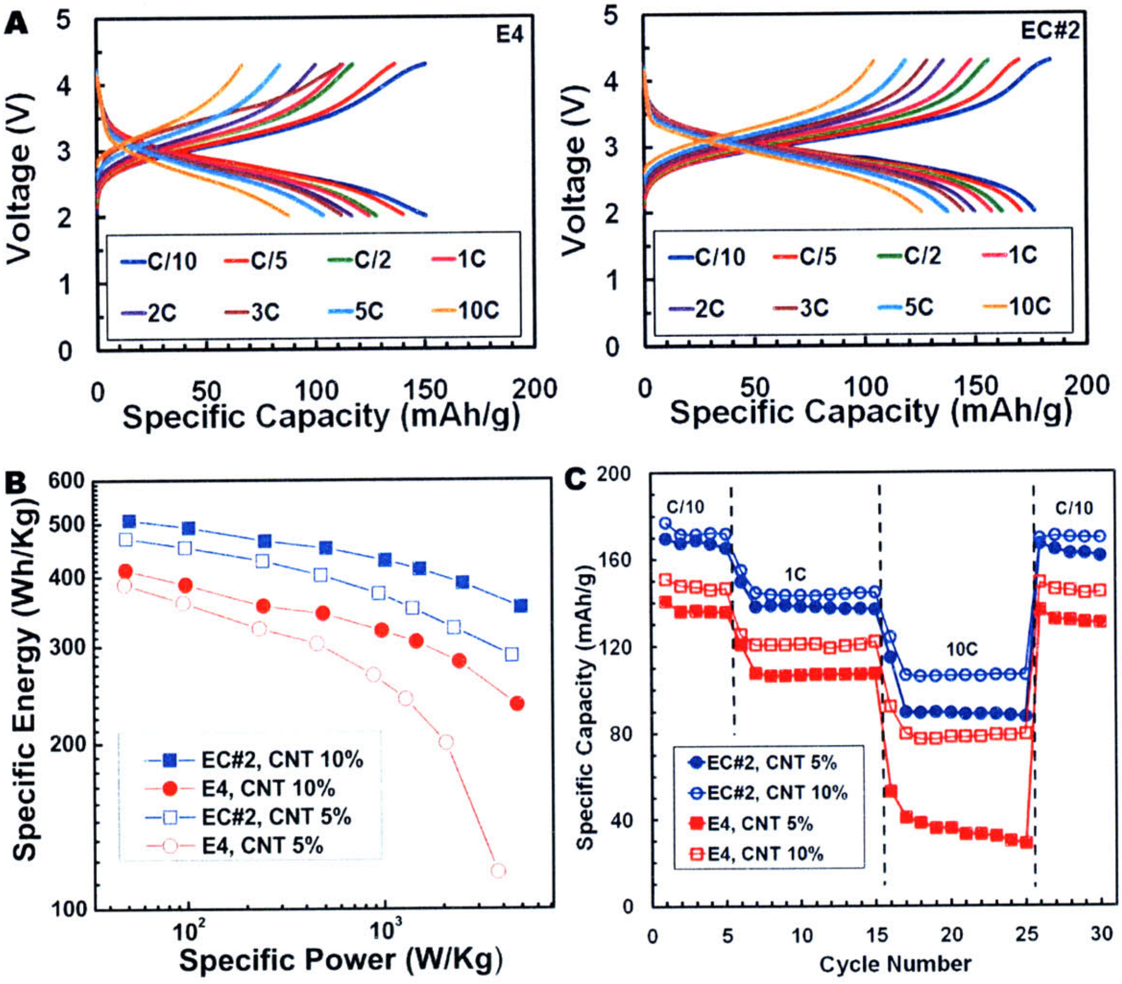

Chapter 5

Biologically Activated Noble Metal Alloy Nanowires for Lithium Ion Battery Anodes

Chapter 5.1 Introduction

The amount of energy stored in the lithium ion battery clearly depends on the cell's output potential and capacity, which is determined by thermodynamics and chemistry of the system[19]. To minimize the cell voltage reduction and thereby maximize the energy density, anodes materials with very negative potential and high capacity have been searched for and studied. Metals or intermetallic compounds that can be alloyed with lithium appeared as promising candidates due to the high theoretical capacity[78, 79]. Major challenges in these materials lie in the mechanical stress related to large volume changes and structural changes accompanying with lithium uptake and release. This mechanical stress results in pulverization and rapid capacity fading[80] which renders these materials not very practical for prolonged usage. Among those materials capable of alloying with lithium, silver (Ag) and gold(Au) react with lithium in a very low voltage range[81]. As seen in binary alloy phase diagrams of Ag-Li and Au-Li systems[82, 83] (Fig 5.1), Ag and Au have several alloy phases with lithium and could alloy with very high percentage of Li (up to $AgLi_9$ and Au_4Li_{15}). However, little is known on the electrochemical response of Au and Ag with lithium. The available reports are mostly limited to the thin film concept[81, 84-86] mainly due to challenges associated with the mechanical stress problem as in most lithium based alloy materials. When the tested electrodes were prepared by normal fabrication process from powder, the capacity of Ag electrodes rapidly decayed below 100 mAh/g within 10 cycles[78]. Although thin film concept could relieve stress related problem, the total energy stored in thin film battery is not high enough for practical application due to the limited amount of materials in thin film.

There is prevailing evidence already that nanostructured materials can improve electrochemical property of electrodes materials compared to the bulk counterparts. One-dimensional functional nanomaterials such as SnO_2[87] and Si[80] have shown improved performance as anodes for lithium ion batteries. In addition to excellent surface activity provided by high surface-to-volume ratio, small diameter of nanowires relieved mechanical stress associated with large volume changes and reduced Li ion diffusion length allowing facile Li ion transport. Regarding the synthesis of high surface-to-volume ratio and small diameter nanowires, the inherent structural characteristic of M13 virus makes this biological building block an excellent template for the synthesis of various functional nanowires. Here, we report the synthesis and electrochemical activity of noble metal and metal alloy nanowires using multiple virus clones for lithium ion battery anode materials.

The wild type filamentous M13 virus has a high aspect ratio with approximately 6.5 nm in diameter and 880 nm in length[16]. Roughly 2700 copies of p8 coat protein self-assemble into the capsid of the wild-type virus, resulting in 5 fold symmetry along the length of virus. Computational simulation of p8 protein assembly shows that the distance between the helically arranged nearest neighbors of each protein is around 3 nm at 100 % incorporation[10]. In addition to these structural advantages, the functionality of subunit proteins of M13 virus can be altered through genetic engineering. Previously, the virus has been engineered to display peptides which have affinity to specific target materials and used to bind, organize and further nucleate those specific materials[10, 12, 17]. For example, gold-binding virus was selected through an evolutionary screening process called biopanning. Virus with a gold-binding peptide motif on the p8 major coat protein was named p8#9 and used for assembling gold nanoparticles[12]. In addition to the biomolecular recognition of specific materials identified through biopanning, the surface functionality of M13 virus can be modified independently through genetic engineering. E4 virus is a modified M13 virus that has tetraglutamate (EEEE) fused to the amino terminus of each copy of p8 major coat protein. Due to the presence of extra carboxylic acid groups compared with wild type M13 virus (M13KE), the E4 virus exhibited increased ionic interactions with cations and can serve as a template for materials growth. With this E4 virus, materials specificity was diminished, but versatility was enhanced. Our group reported successful nanowires synthesis of several function materials such as Co_3O_4[13], a-$FePO_4$[88] and single crystalline Ag nanowires[18] on E4 template. Using two M13 clones for specificity (p8#9) and versatility (E4), we have synthesized nanowires of noble metal and their alloys with control over diameter, morphology and compositions in this work. The virus-enabled synthesis of noble metal nanowires was remarkably facile and high-yield compared to traditional method[89]. The biologically derived nanowires with diameter below 50 nm showed electrochemical activity towards lithium even when the electrodes were prepared from bulk powder forms. By showing characteristic electrochemical response with noble metals and their alloys, the M13 biological platform proved itself as a useful toolkit for study on the basic materials property.

Chapter 5.2 Experimental

Synthesis of Ag viral nanowires The genetically engineered viruses were amplified using *Escherichia coli* bacterial medium and purified by standard PEG/NaCl precipitation method. For the viral Ag nanowires synthesis, 50 μl E4 virus solution in 0.1 M TBS buffer ($2x10^{11}$ PFU/ml) was dialyzed against pH=9.5 water overnight, followed by incubation with 2 mM, 1 ml silver acetate ($AgOOCCH_3$) solution for 12 hours in the dark at 37℃. All solutions were aqueous after the virus dialysis. The Ag nanowires were formed by reducing with 10 mM, 1 ml sodium borohydride ($NaBH_4$) for 4 hours at room temperature. The resulting viral nanowires were collected through filtration and washed with water several times. The collected powder was dried in a 100 °C vacuum oven overnight. Au and Au_xAg_{1-x} alloy nanowires were templated on gold-binding p8#9 virus[12]. The clone p8#9 has peptides insert on p8 major coat protein; the inserted peptide sequence VSGSSPDS was selected from screening a p8 phage display library on gold substrate[12]. Detailed synthesis methods of Au and alloys are described elsewhere[89]. For all alloy materials, composition was determined in EDX quantitative analysis.

Structural and Chemical analysis The microstructure of nanowires was analyzed with Transmission Electron Microscopy (JEOL 200CX TEM and JEOL 2010F TEM). For TEM analysis, solutions were dropped on copper grids, washed with distilled water several times and dried. Chemical composition was determined by Direct Current Plasma-Atomic Emission Spectroscopy (DCP-AES, Luvak, Boylston, MA). For Thermo Gravimetric Analysis (TGA), a RGA Q50 (TA instrument) apparatus was used. Samples placed on a platinum pan were preheated to 100 °C and held for 5 min to remove surface absorbed water. After cooling down to 30°C, samples were heated to 700 °C at a heating rate of 10 °C /min in 90 ml/min nitrogen flow and 10 ml/min helium flow. X-Ray Diffraction (XRD) was done using Cu K_α radiation and a Rigaku RU300 powder diffractometer.

Electrochemical tests For positive electrodes preparation, viral a-$FePO_4$ nanowires were mixed with Super P (TIMCAL, SUPER P® Li) carbon black and polytetrafluoroethylene (PTFE) binder in a mass ratio of 70: 25: 5. The detailed mass ratio of each component in electrodes is noble metal nanowire: virus: Super P carbon: PTFE= 59.5: 10.5: 25: 5. The mixture was roll milled and punched into disks with diameters of 6 mm. Typical electrode thickness was 20 to 40 μm. The cell was assembled in an argon filled glove box using lithium foil as a negative electrode, a microporous polymer separator (Celgard 3501™) and liquid electrolyte mixtures of 1 M $LiPF_6$ in ethylene carbonate: dimethyl carbonate (EC: DMC) = 1: 1 in volume ratio (Ferro Corporation). The testing cell was a coin cell configurations. The assembled cell was galvanostatically tested between 0 and 2.0 V at 50 mA/g current density using a Solatron Analytical 1470E potentiostat.

Chapter 5.3 Results and discussion

Synthesis of Ag nanowires was demonstrated in our previous work with E4 virus using spontaneous photo-reduction[18]. The spontaneous reduction produced straight single crystalline nanowires along the length of virus, but the product yield was not high enough for the practical application for bulk devices such as battery electrodes. To increase Ag nanowire yield, sodium borohydride ($NaBH_4$) reducing agent was introduced. In Fig.5.2A, wavy polycrystalline Ag nanowires with rough surface were generated with the forced reduction with $NaBH_4$. The nanowire size was estimated 15~20 nm in diameter. The different morphology could be associated with the increased nucleation site for forced reduction contrary to the limited nucleation and specific growth on the seed already formed in self-catalyzed spontaneous reduction. The XRD pattern in Fig.5.2B also confirmed pure silver nanowires formation without impurity. The electrochemical property of viral Ag nanowires was tested in the voltage window of 0~2.0 V against lithium foil in Fig. 5.2C. The first two discharge/charge curves are shown. The viral Ag nanowires showed pseudo plateaus at 0.08 V and 0.02 V during lithiation process while lithium removal from alloy occurred in two steps at 0.14 and 0.3 V in fairly good agreement with the previously reported values[84, 85] with slight polarization of plateaus at 0.02 V and 0.14 V. From thermodynamic viewpoint, plateaus in potential profile stem from the compositional two-phase regime. For two component system such as Ag-Li and Au-Li, Gibbs Phase Rules determines the degree of freedom in two phase equilibrium regime as zero. ($F = C-P$ when temperature and pressure are fixed. F: degree of freedom, C: number of components, P: number of phases) Therefore, the electrode potential is independent of overall composition when the composition is changed as a result of electrochemical reaction. If the test condition is near-equilibrium, all two phase equilibrium regimes in binary phage diagram Fig. 5.1 should appear as plateaus and single phase regions display gradual changes in potential profiles with the degree of lithiation[90]. However, since most electrochemical testing is done under dynamic condition, the potential profile obtained could be different from near-equilibrium condition. Among the alloy phases with Li, two phases were reported to be reversible during the reaction with lithium[84]. One unknown phase (designated as phase II) was found to be related to the plateaus at 0.06 V (alloying) and at 0.3 V (de-alloying)and AgLi β phase was associated with 0.02 V (alloying) and 0.14 V (de-alloying) plateaus[84]. Large irreversible capacity from 0.7 V down to alloying plateau appeared during the first discharge. The irreversible capacity in this voltage range was attributed to the Super P® carbon mixed during the electrode preparation process. This capacity from Super P® carbon was very irreversible and negligible in the following cycles. The viral silver nanowires delivered 534 mAh/g discharge capacity at second cycle which corresponds to alloy composition of $AgLi_{2.15}$. With the viral silver nanowires with very low potential, the first full virus-based lithium ion batteries with a viral nanowires cathode and a viral nanowires anode could be fabricated using viral a-$FePO_4$ nanowires. Since both materials are not lithiated, silver nanowires were first lithiated electrochemically and then re-assembled as a negative electrode with a virus-enabled a-$FePO_4$ positive electrode. The resulting cell stably worked with 3 V output potential (Fig. 5.3).

For the synthesis of pure gold nanowires and gold-silver alloys, gold-binding virus named p8#9 was used. This virus was selected for having peptide motif expressed on the major coat protein with specific affinity to gold[12]. In the synthesis of Au and Au_xAg_{1-x} alloy nanowires, p8#9 virus served as a template that can bind and thereby make complex with Au ions. In Fig 5.4A, pure Au nanowires with average 40 nm in diameter demonstrated rough surface when synthesized without surfactants. The electrochemical response of viral Au nanowires were examined in the alloying/de-alloying voltage range of 0~2.0 V (Fig.5.4B). In viral Au nanowires system, two well-defined plateaus were observed at 0.2 V and 0.1 V during alloying with lithium and 0.2 V and 0.45 V during de-alloying process. Even though only a little is known on the electrochemical response of Au with Li, these values are also in good agreement with the reported values[79, 81, 86]. As for the silver nanowires, large irreversible capacity from Super P® carbon was also observed between 0.7 V and 0.2 V. The specific discharge capacity was 501 mAh/g at second cycle which corresponds to the alloy composition of $AuLi_{3.69}$. The potential profile of Au when reacted with Li was strikingly similar to the one for the Ag-Li system except for the absolute values of the plateau potentials. Since Au and Ag have the same crystal structure and the alloy AuLi also has the same β phase structure with AgLi, we inferred that the similar potential profiles are an indication of the same reversible alloy structure formation of the phase II and β phase (AuLi, in this case) during the lithiation process. To find out the relevant alloy phases, XRD patterns of different stage of alloying with Li were obtained. In Fig 5.4(C), Au and ordered Au_3Li α_1 phases were identified at stage #1 of 0.2 V discharge plateau with trace of AuLi β phase. At stage #2 of 0.1 V plateau, Au_3Li α_1 phase and trace of AuLi β phase were present while the peaks from Au was decreased. Although the relation between unknown phase II for Ag-Li alloy system and Au_3Li α_1 phase is not clear, the close structural similarity of Au-Li alloys with Ag-Li alloys formed during dynamic electrochemical alloying process could be inferred.

Au-Ag alloy nanowires with different composition were produced on p8#9 in Fig 5.5 ~Fig. 5.7. TEM images in Fig 5.5A, Fig 5.6A and Fig 5.7A showed nanowires with well-defined surfaces. We assumed that these morphological changes are related to the addition of CTAB surfactant during the alloy synthesis. Surfactants such as CTAB serve as a surface stabilizer reducing surface energies, thus can enhance the uniformity of surface morphology. In Fig. 5.5A, Au_xAg_{1-x} alloy nanowires with 25 nm in diameter are shown. EDX line scan in Fig 5.5B clearly verified the formation of Au_xAg_{1-x} alloy and the quantitative EDX analysis determined the atomic ratio as 1:1. This alloy composition thus was assigned as $Au_{0.5}Ag_{0.5}$. EDX point analysis of the same nanowires confirmed that the nanowires have uniform homogeneous composition. On the other hand, the nanowires grown on the wild-type M13 virus showed non-uniform composition along the virus even though the universal composition was the same with the nanowires on p8#9 virus. The diameter of nanowires are: 25 nm for $Au_{0.5}Ag_{0.5}$, 20 nm for $Au_{0.67}Ag_{0.33}$ and 30 nm for $Au_{0.9}Ag_{0.1}$ (Fig 5.5A, 5.6A and 5.7A). Due to the smooth surface nature, particle size variation along the virus is not large. In the first two galvanostatic test curves, the Au_xAg_{1-x} alloy nanowires did not show discrete plateaus but displayed rather gradual changes in potential from 0.2 V to 0 V during discharge and from 0 V to 0.5 V during charge as if they are single phase in two component system with potentials dependent on the composition, in other words the degree of lithiation. (Fig 5.5C, 5.6B and 5.7B) However, as Au composition increases close to 1, potential profile appeared more like pure Au.

The electrochemical responses of Au_xAg_{1-x} alloy nanowires from composition of x=0 to 1 were compared in Fig 5.8. As mentioned above, the alloys present gradual changes in potential profile instead of stepwise plateaus from both Ag and Au. As the composition approached Au: Ag = 0.5: 0.5, the potential profile showed more pseudo-single phase behavior. We speculate that the pseudo-single phase behavior in alloy system could be related to the formation of ternary alloys. Since Au-Ag-Li system has three components, coexistence of two phases (host Au_xAg_{1-x} and ternary alloys of Au-Ag-Li) leaves one degree of freedom (Gibbs Phase Rule, F=C-P=3-2=1). Therefore the potential could be dependent on the composition, thus could change with the degree of lithiation. Considering the remarkably similar crystal structures of Au with Ag and Au-Li alloys with Ag-Li alloys, the ternary alloys with the same reversible alloy structure of β phase are expected. Detailed XRD study at different stages of alloy is underway. As Au composition increased in Au_xAg_{1-x} alloys, the discharge/charge potentials increased from Ag plateaus to Au plateaus. The discharge/charge potentials were clearly dependent on the composition. Since the potential is determined by thermodynamics, the activity of Li in the materials could be changed in the homogeneous alloy structure having values dependent on the composition. The first discharge capacities of alloys were all similar with values 900 ~ 965 mAh/g, but due to high irreversible capacity from Super P® carbon, second discharge capacities dropped to 440 ~534 mAh/g depending on the alloy composition. The trend up to second cycle was similar for all alloy composition. In Fig. 5.8C, the capacity retention of the viral pure Ag, Au and alloy nanowires upon cycling at 50 mA/g current rate for 10 cycles was shown. While the pure, surfactant-free Au and Ag nanowires showed rapid capacity fading, the alloys displayed improved capacity retention. There were several reports that some alloys that make active/inactive composite structure with lithium could improve cycling performance due to the buffering effect of the inactive component[91]. Other alloys that have components both active with lithium displayed stable capacity retention when the components make intermetallic compounds of the structure with little/moderate volume change when alloyed with lithium[78]. Since both Au and Ag are able to alloy with lithium and their alloys have the same structure as Au and Ag, we assumed that the improvement of capacity retention in our alloy system is associated with CTAB surface stabilization and/or the pseudo-single phase behavior in potential profiles.

To demonstrate how the surface stabilization affects the electrochemical performance of noble metal alloys, $Au_{0.9}Ag_{0.1}$ nanowires were synthesized without CTAB surfactants. In Fig.

5.9A, surfactant-free nanowires with an average 35 nm in diameter having rough surface were templated on the virus. The electrochemical responses of the first three galvanostatic cycles from two nanowires with different surfaces were confirmed almost identical except the slight difference in specific capacities (Fig. 5.9 B and C). However, in Fig. 5.9D, capacity retention for 10 cycles showed a clear difference. The specific capacity of surfactant-free nanowires decreased rapidly within 10 cycles, while that of nanowires with CTAB-stabilized surface showed rather moderate fading. For the nanowires with CTAB-stabilized surface, particle-coalescence upon cycling could be suppressed due to presence of the surface adsorbed CTAB. In addition, nanowires grown without CTAB are more branched, thus could experience more homogenizing force by Oswald ripening which leads to poor cycling performance. Although CTAB stabilization can improve cycling performances, there can be another explanation for the better capacity retention for the Au_xAg_{1-x} alloy nanowires. Since the strain level of the system depends not only volume changes but also inhomogeniety, the inherent inhomogeniety in two-phase composition region is believed to be one of the reasons for poor capacity retention[92]. In terms of reaction homogeneity, the pseudo-single phase behavior in potential profile for Au_xAg_{1-x} alloys can be beneficial. However, it is difficult to tell in this study if both homogeneity and surface stabilization are working or only one of them is determining for better cycling performance. To clearly check the importance of surface stabilization and homogeneity in reaction, synthesis of pure Au and Ag nanowires with CTAB stabilizer and synthesis of $Au_{0.5}Ag_{0.5}$ alloy nanowires without CTAB is being investigated.

Reducing materials dimension proved to be effective in decreasing mechanical stress, however, for the nanowires with diameter below 40 nm in this study, other factors such as homogeneity and surface stabilization appeared more influencing from the fact that the Ag nanowires with rough surface showed poor cycling performance even with the smallest particle size among the tested nanowires (15~20 nm). To systematically demonstrate the effect of particle size, nanowires of the same composition but with different size are being prepared. Although the alloy nanowires with diameters below 30 nm showed moderate improvement in cycling performance up to 10 cycles, all alloy nanowires eventually failed to maintain stable capacity when tested up to 20 cycles. Tailoring alloy nanostructures on the virus template to suppress coalescence is under investigation for better cycling performance.

Chapter 5.4 Conclusion

Biological systems offer capabilities for environmentally benign materials synthesis. The two M13 viruses, genetically engineered for specificity (p8#9 virus) and versatility (E4 virus), served as a template for the synthesis of noble metal nanowires with diameters below 50 nm. The inherent structural characteristic of M13 virus enabled the synthesis of high aspect ratio nanowires. With synergetic combination of biological building block and synthetic chemistry, this facile and high yield synthesis conferred controls over particle size, morphology and compositions. The biologically derived noble metal and alloy nanowires with diameter below 50 nm showed electrochemical activities toward lithium even when the electrodes were not thin film configurations. Improvement in capacity retention was achieved by tailoring particle size, alloy formation and surface stabilization. With advantages of facile and environmentally benign synthesis, M13 biological platform proved itself as a useful toolkit for the study on the basic electrochemical property of materials.

Chapter 5.5 Figures

Figure 5.1. Binary Alloy Phase Diagram of (A) Ag-Li system[82, 93] (B) Au-Li system[83, 94]. In the graphs, blue-colored regions indicate single phase composition ranges and white regions are two phase regime.

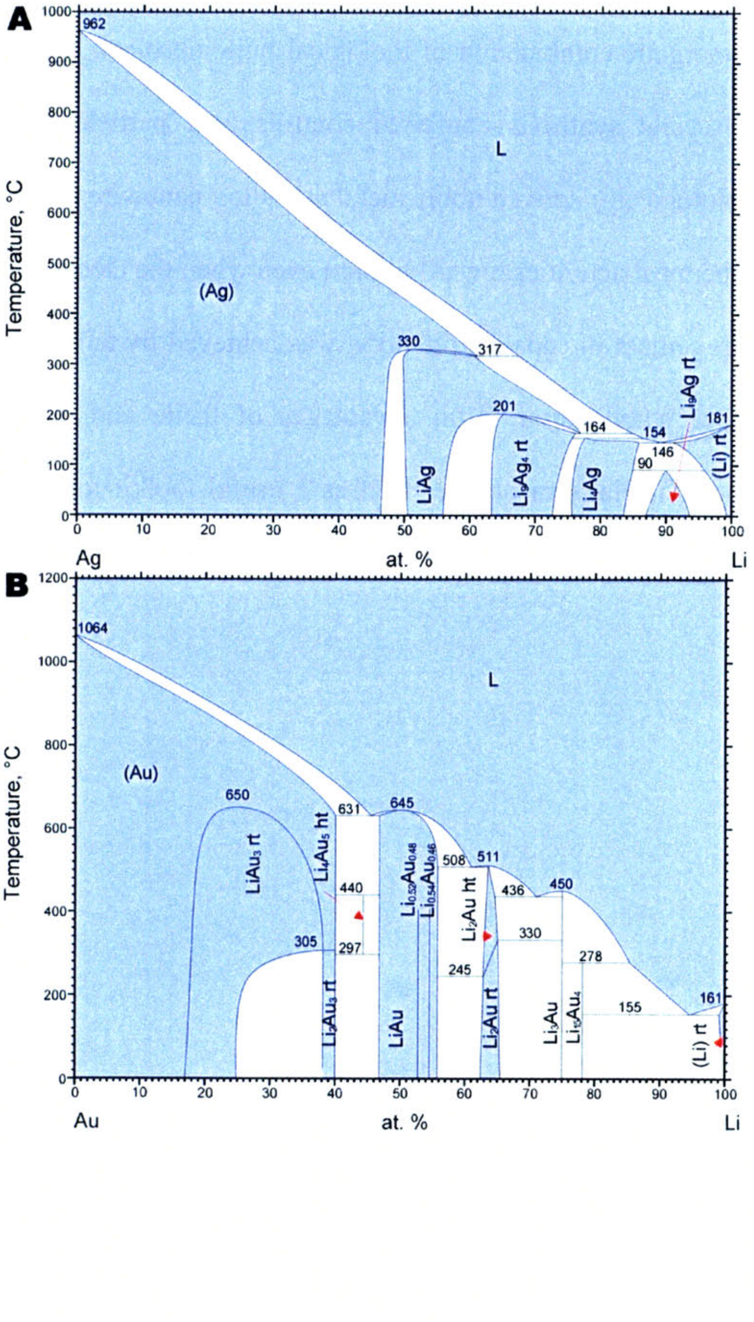

Figure 5.2. Characterization of surfactant-free Ag nanowires on E4 virus. (A) TEM images (B) XRD (C) First two discharge/charge curves tested between 0 and 2.0 V. Active material loading was 4.28 mg/cm^2. Current density was 50 mA/g.

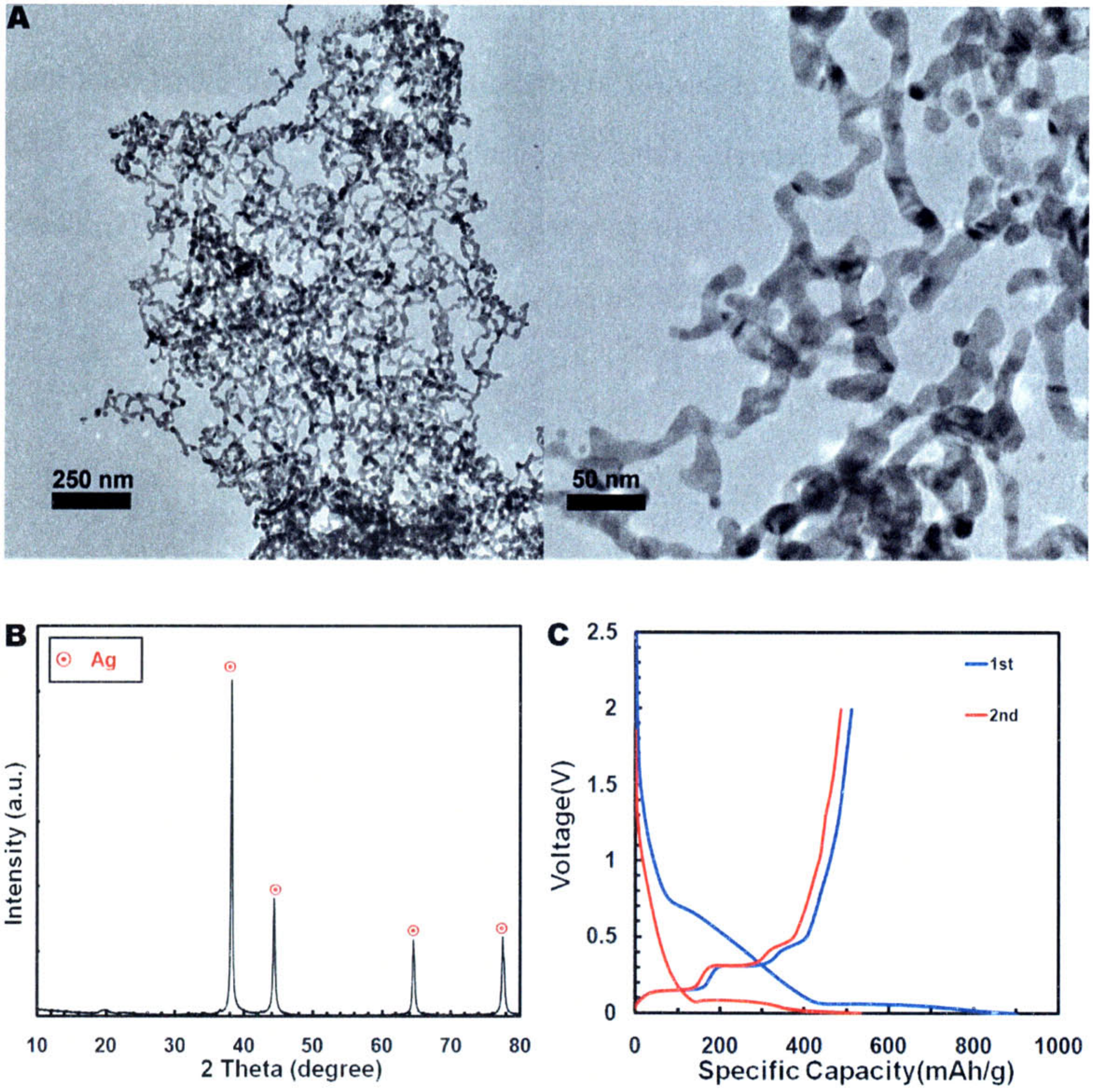

Figure 5.3. The first discharge/charge profiles of a full virus based (a viral cathode and a viral anode) battery. Battery was assembled with viral a-$FePO_4$ nanowires as a positive electrode and viral Ag nanowires as a negative electrode. Both nanowires were templated on E4 viruses. Both electrodes were mixed with Super P® carbon and PTFE with a mass ratio of 70: 25: 5. Viral Ag nanowires were first lithiated electrochemically and then re-assembled as a negative electrode with a virus-enabled a-$FePO_4$ positive electrode. The cell was galvanostatically tested in a voltage window of 1.5-4.3 V at a rate of C/10. The active materials loading was 2.10 mg/cm^2 for a positive electrode and 5.23 mg/cm^2 for a negative electrode.

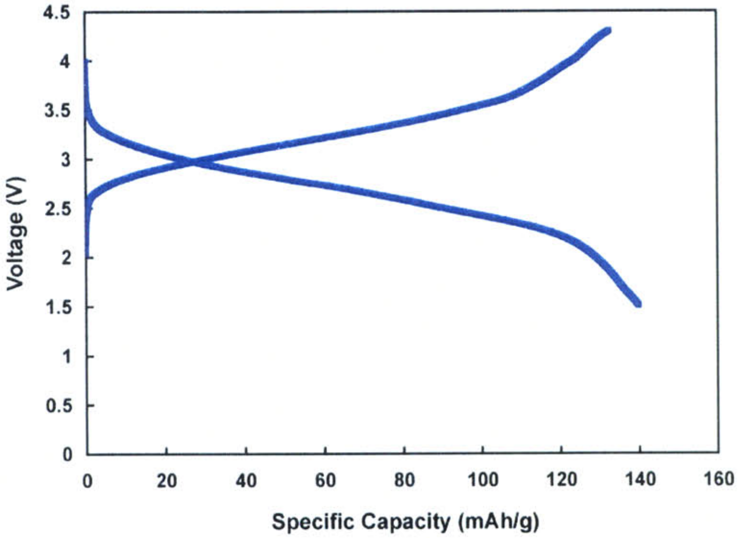

Figure 5.4. Characterization of surfactant-free Au nanowires on p8#9 virus. (A) TEM images (B) First two discharge/charge curves tested between 0 and 2.0 V. Active materials loading was 5.55 mg/cm^2 and current density was 50 mA/g. (C) XRD evolution patterns at different stages of alloying process. Stage #1 and #2 are denoted in Fig 5.4(B).

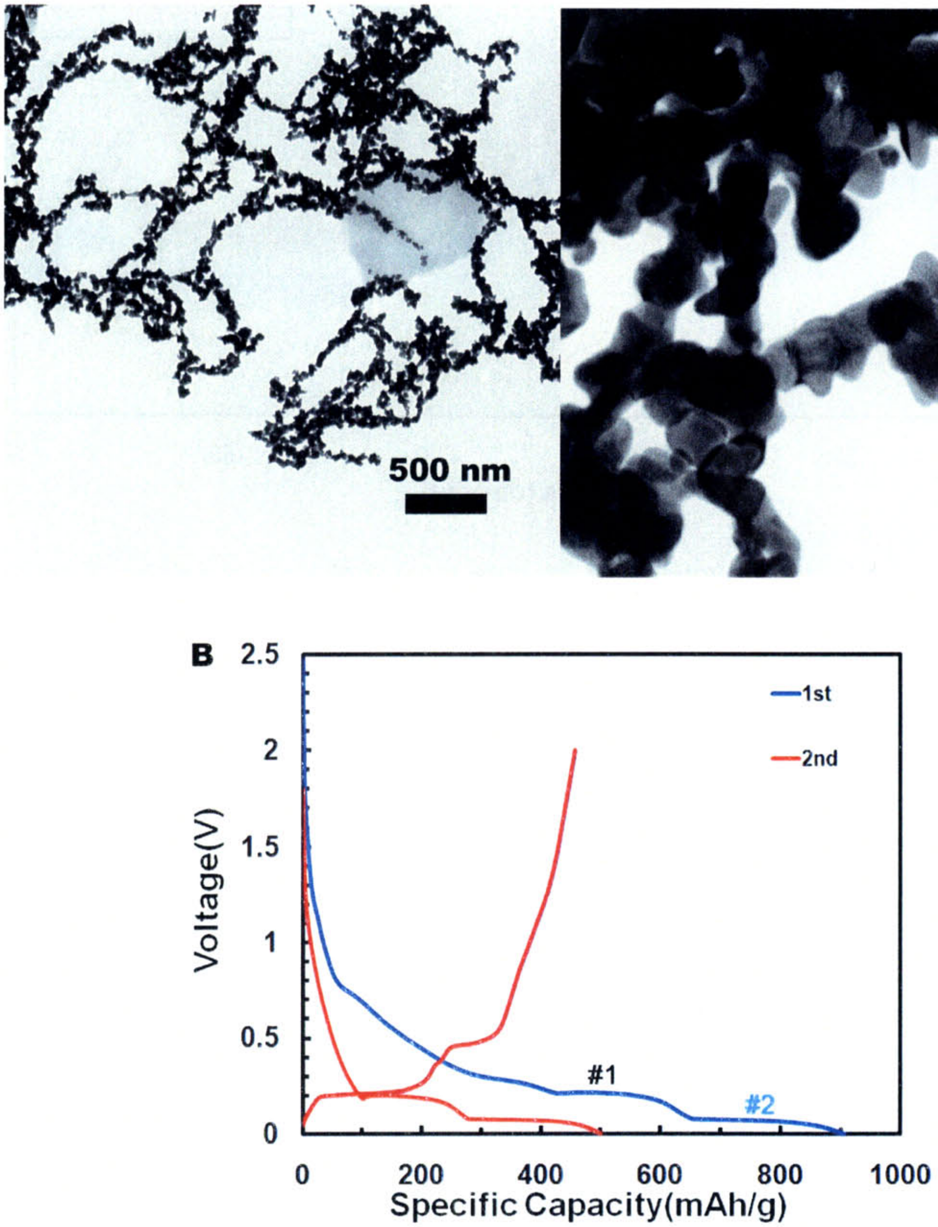

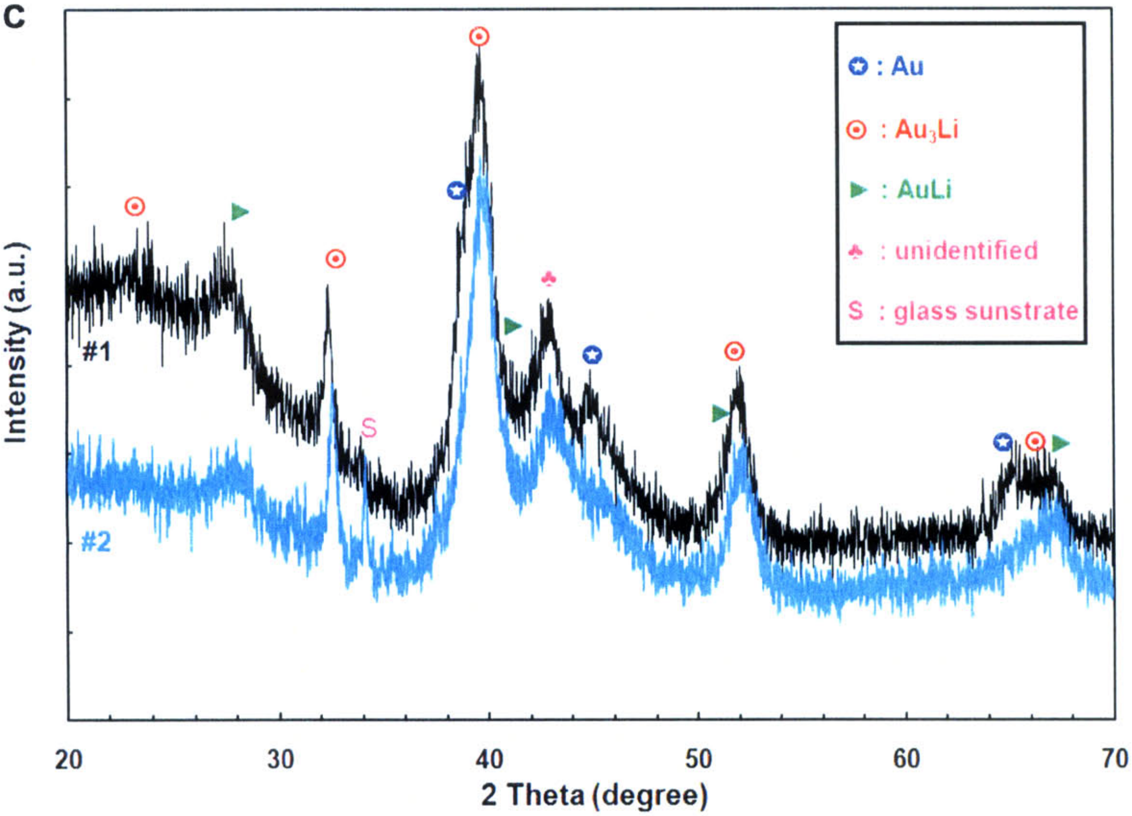
c
: Au
: Au3Li
: AuLi
: unidentified
S : glass sunstrate
S
#1
#2
Intensity (a.u.)
2 Theta (degree)
20
30
40
50
60
70

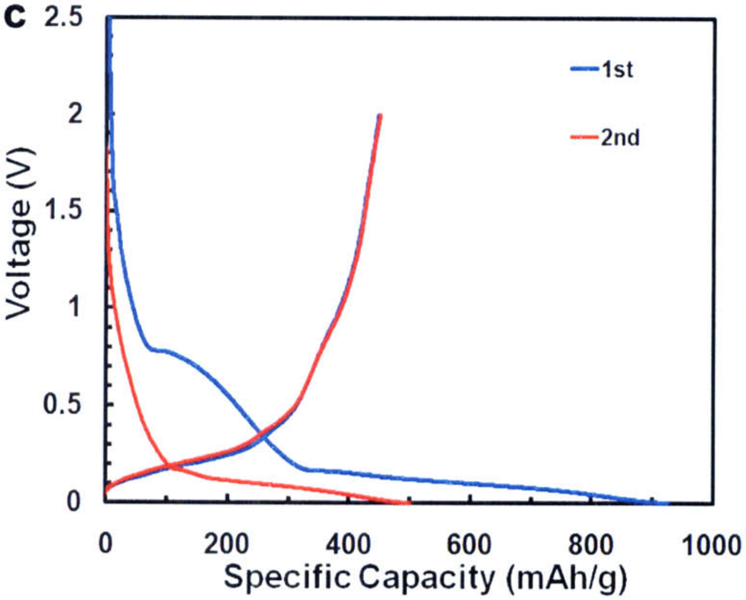
c
2.5
2
1.5
1
0.5
0
Voltage (V)
0
200
400
600
800
1000
Specific Capacity (mAh/g)
1st
2nd

Figure 5.5. A Characterization CTAB-stabilized $Au_{0.5}$ $Ag_{0.5}$ nanowires on p8#9 virus. (A) TEM images. (B) EDX line scan showing the presence of element Au and Ag in the template nanowires. (C) First two discharge/charge curves tested between 0 and 2.0 V. Active materials loading was 3.89 mg/cm^2 and current density was 50 mA/g.

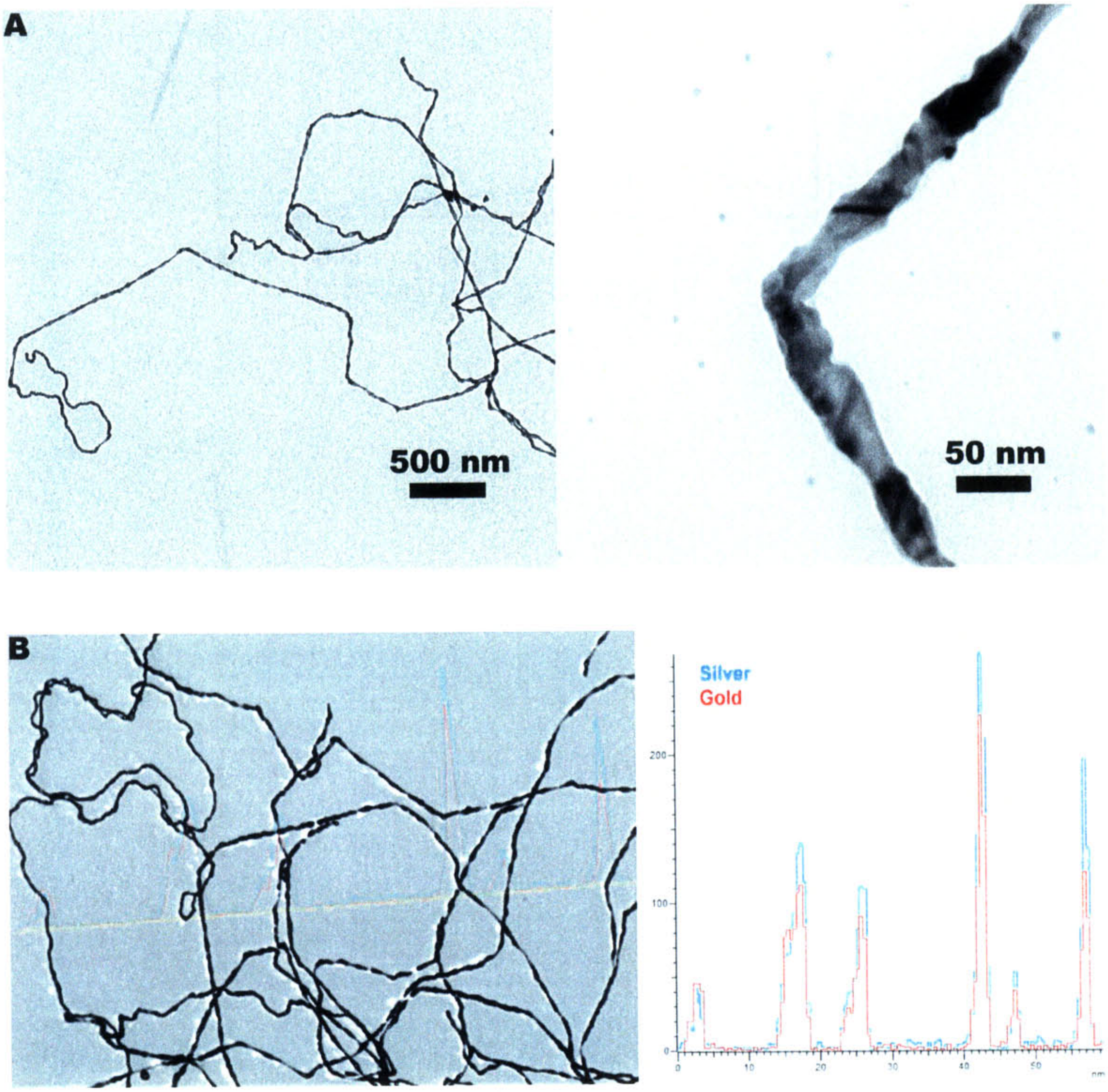

Figure 5.7. Characterization of CTAB-stabilized $Au_{0.9}Ag_{0.1}$ nanowires on p8#9 virus (A) TEM images. (B) First two discharge/charge curves tested between 0 and 2.0 V. Active materials loading was 5.11 mg/cm^2 and current density was 50 mA/g.

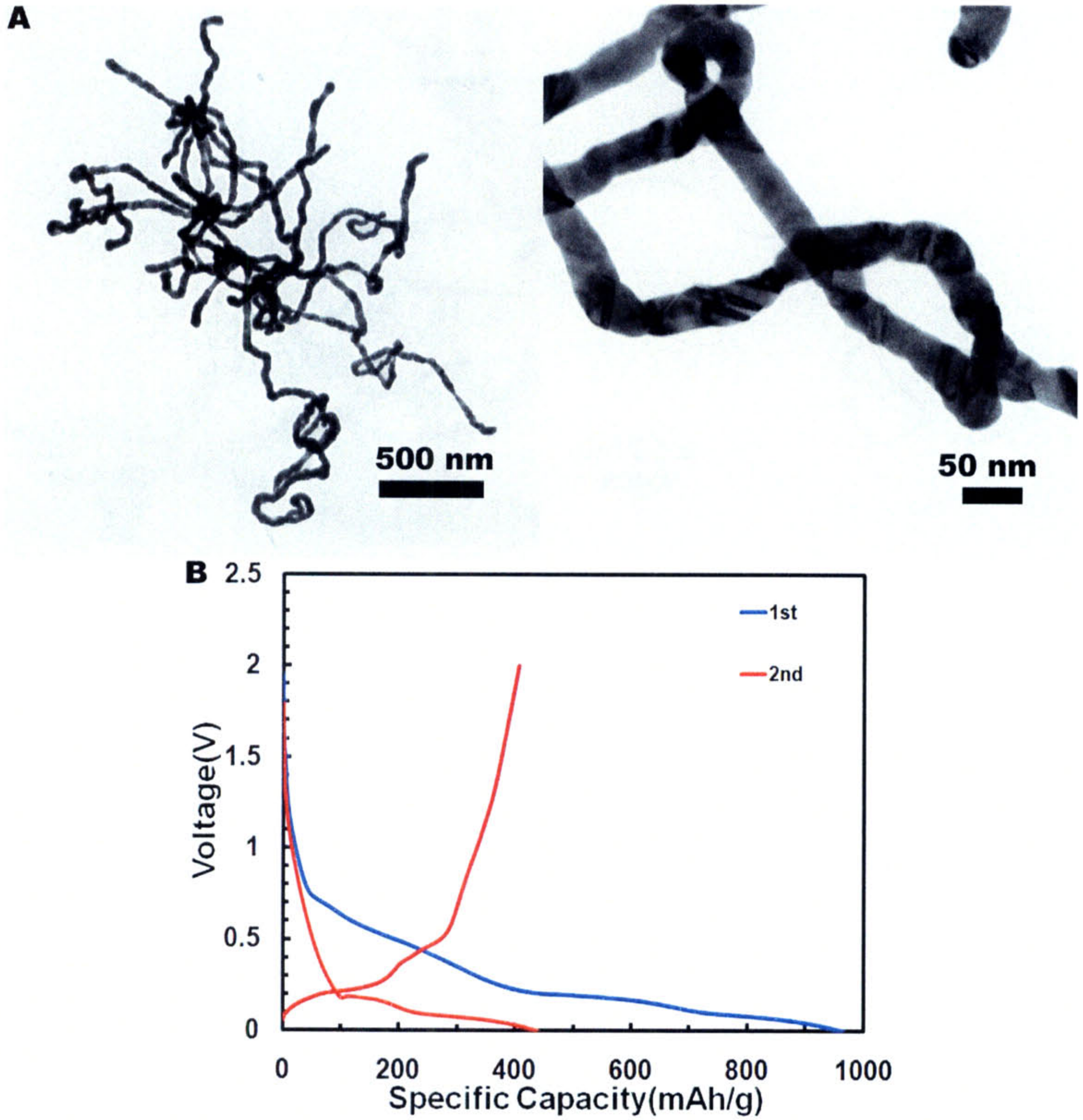

Figure 5.6. Characterization of CTAB-stabilized $Au_{0.67}Ag_{0.33}$ nanowires on p8#9 virus. (A) TEM images. (B) First two discharge/charge curves tested between 0 and 2.0 V. Active materials loading was 4.47 mg/cm^2 and current density was 50 mA/g.

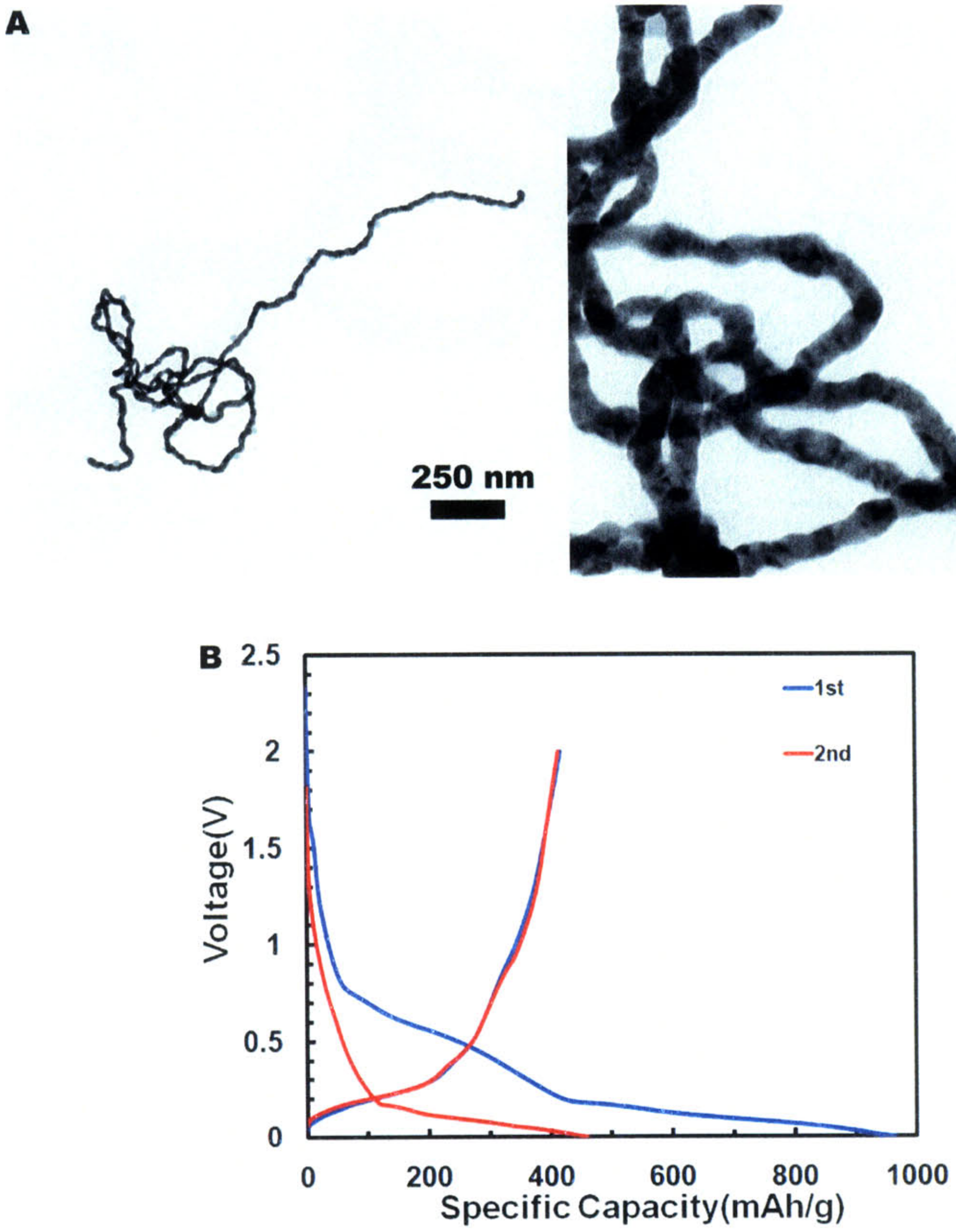

Figure 5.9. Characterization of surfactant-free $Au_{0.9}Ag_{0.1}$ nanowires on p8#9 virus. (A) TEM (comparison with Fig.5.6A for morphology) (B) First two discharge/charge curves tested between 0 and 2.0 V. Active materials loading was 5.55 mg/cm^2 and current density was 50 mA/g. (C) Comparison of third discharge/charge curves with same composition but different surface morphology. (D) Capacity retention for 10 cycles. For comparison, capacity retention of nanowires with the same composition but different surface morphology is shown.

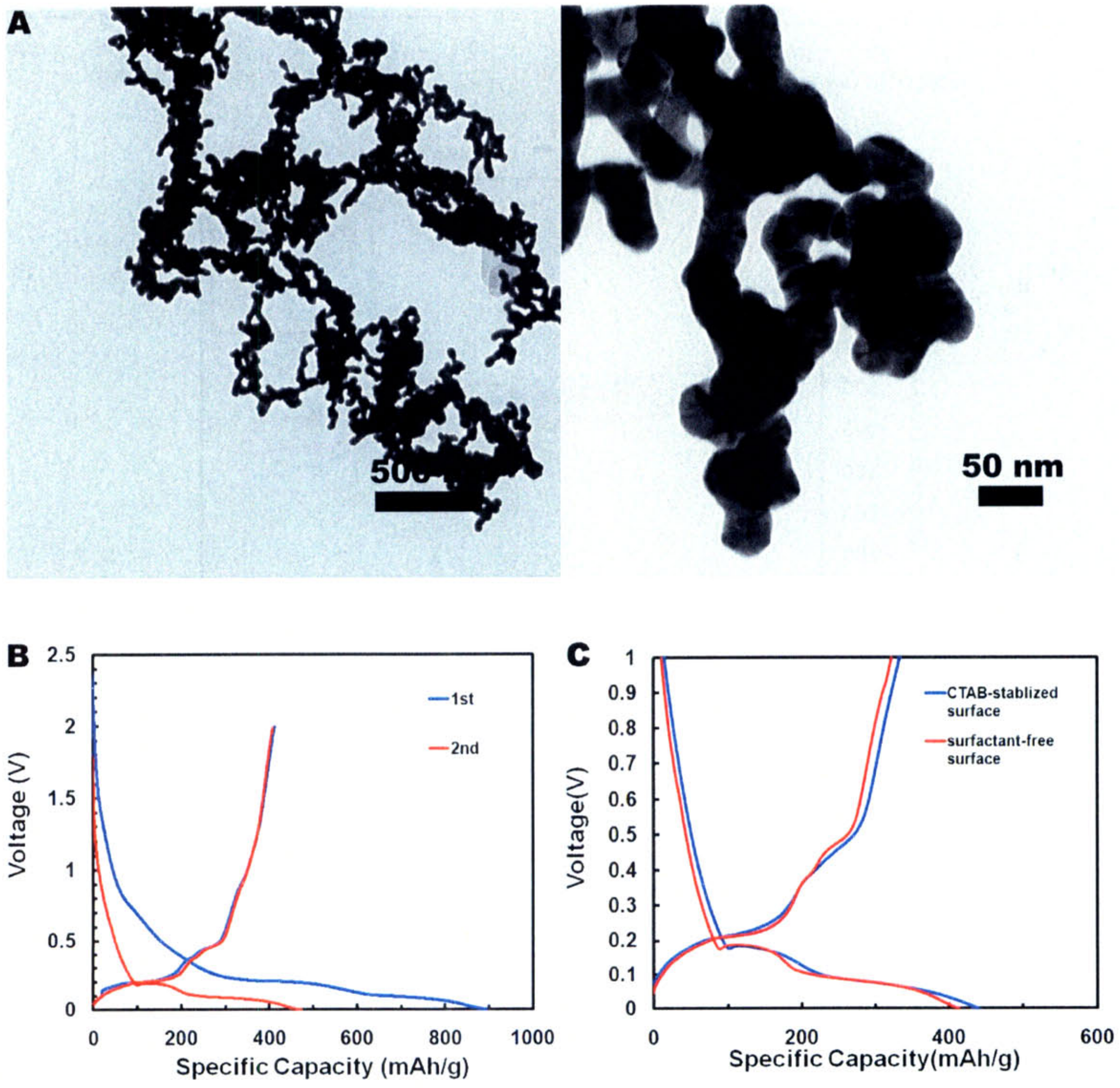

Figure 5.8. Electrochemical property with composition Au_xAg_{1-x} (x = 0, 0.9, 0.67 and 0.5) tested between 0 and 2.0 V. Current density was 50 mA/g for all test. (A) Second discharge curves. (B) Second charge curves (C) Capacity retention for 10 cycles.

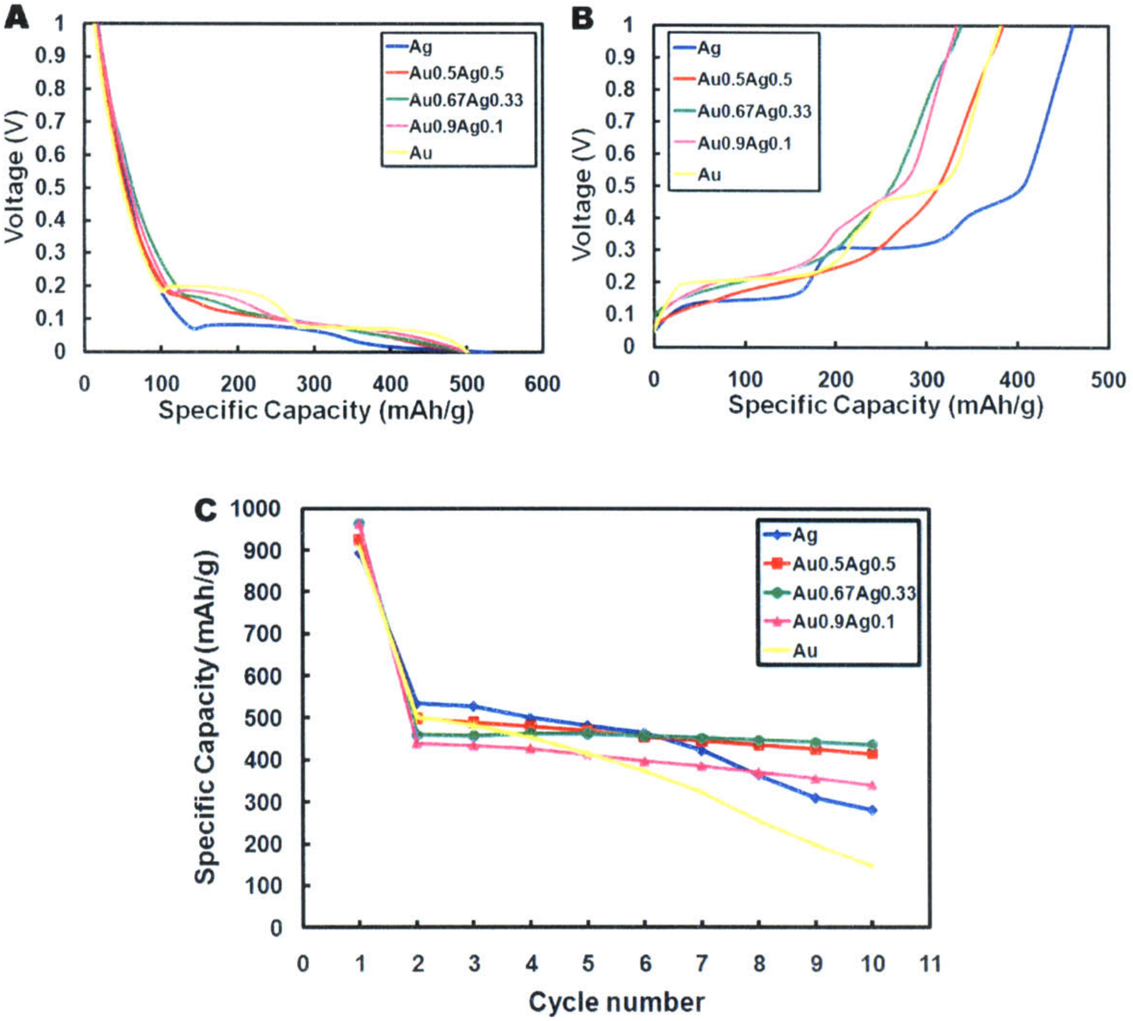

D

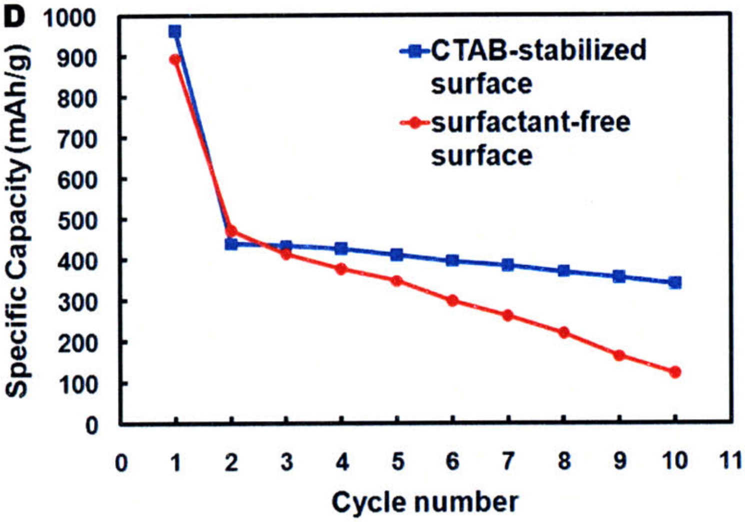
Specific Capacity (mAh/g)
1000
900
800
700
600
500
400
300
200
100
0
0
1
2
3
4
5
6
7
8
9
10
11
Cycle number
CTAB-stabilized surface
surfactant-free surface

Chapter 6

Ongoing Research Works and Future Directions

Chapter 6.1 Hybrid BiF_3/SWNTs cathode electrodes

Chapter 6.1.1. Preliminary results and future works: This work is under way in collaboration with Dr. Mark Allen, Dahyun Oh and Hyunjung Yi in our group

By developing two-gene system with a universal handle to pick up electrically conducting carbon nanotubes, we facilitated a novel method to realize true nanoscale electrical wiring for high power lithium ion batteries using basic biological principles. With the ease of genetic engineering, this biological scaffold could further extend possible sets of electrode materials by activating classes of materials that have been excluded because of their extremely low electronic conductivity such as BiF_3. Metal fluorides have been found to react with lithium by conversion reaction, thus have very high theoretical capacity. Owing to their high volumetric density, they are expected to have very high volumetric energy density. However, due to their ionic nature, they are electronic insulators and have been excluded from conventional electrode materials. The electrochemical activity of metal fluorides have been demonstrated only when prepared in a truly nanostructure state and dispersed in a conductive matrix such as carbon[95]. Herein, we have explored if the platform EC#2 we developed for the true nanoscale electrical wiring would also work for more insulating BiF_3 cathodes.

We have successfully mineralized bismuth fluoride on E4 virus at room temperature. 200 mM , 0.8 ml $Bi(NO_3)_3$ dissolved in 1 M acetic acid aqueous solution was injected using syringe pump for 1 hour to the 128 ml aqueous mixture of LiF solution with various concentrations and virus. Virus (8×10^9 PFU/ul, 3 ml) was dialyzed against water overnight before mixing with LiF solution. Figure 6.1.1 shows TEM images synthesized viral BiF_3 nanowires. As shown in the figure, BiF_3 was successfully template on the virus. The particles size appeared 30~50 nm, however, close examination revealed primary particle size as 10~15 nm. The particles aggregated to secondary structures with size of 30~50 nm. Crystalline phase was determined by XRD in Fig. 6.1.2. The biologically synthesized BiF_3 was highly crystalline and the peaks were indexed as cubic fluorite structure BiF_3. However, slight peak shift at high angle indicates that it is not exactly a fluoride, but very small amount of oxygen is incorporated as oxyfluorides. The determination of exact composition is underway. The preliminary electrochemical test results are shown in Fig. 6.1.3. All electrodes were prepared by mixing with Super P carbon and PTFE binder with mixing ratio of powder tested: Super P carbon: PTFE = 70: 25: 5. During early electrochemical test, electrolyte incompatibility was noticed with 1 M $LiPF_6$ electrolyte as previously reported with BiO_xF_{3-2x}/C electrodes[96]. Therefore, 0.4 M $LiClO_4$ in EC: DMC= 1:1 was used in the electrochemical test for this material. This electrolyte incompatibility also suggests that there is trace amount of oxygen in our BiF_3. In Fig. 6.1.3A, the ratio of bismuth precursor to fluoride precursor was changed from 1: 1 to 1:20. (LiF concentration, 1.25mM to 25 mM) As the LiF concentration decreases, the specific capacity as well as discharge potential decreased remarkably. We speculate that this could be associated with the increase of oxygen content in the compound which could be accompanied with the decrease of fluoride in the precursor. For 1:1 sample, small amount of bismuth oxide impurity were also found in the XRD (data not shown). Compared to the traditionally synthesized macrostructured BiF_3, the specific capacity of BiF_3 in this study at C/5 rate is much higher (140 mAh/g vs. 40 mAh/g[95]) due to small particle size even without virus templating. First charge/discharge curves of viral BiF_3 nanowires were shown in Fig. 6.1.3B. BiF_3 templated on E4 virus showed slightly higher specific capacity and less polarization possibly due to the smaller size particle when templated on the virus. (Fig. 6.1.3C) However, even with this BiF_3 nanosized particles on the virus, the electrochemical performance was still inferior to the best reported values having nanocomposite carbon mixture[95]. Here, we have applied our biololgically derived nanoscale wiring platform EC#2 as a wiring tool for more insulating BiF_3 cathodes. However, the surfactant used for SWNTs dispersion in water turned out to oxidize BiF_3. In Fig. 6.1.4, XRD curves of BiF_3 after reacting with surfactant are shown. Synthesized BiF_3 was washed with water before reacting with surfactant to remove remaining ions and re-dispersed in pure water. The mixing ratio was 1:1 by volume. After reacting for 30 min, BiF_3 powder was washed with water and acetone. As shown in Fig. 6.1.4, both SC and SDS surfactants oxidize BiF_3 leading peak shift at high angle and the degree of oxidation was severe for SC surfactants. For SDS surfactant, the XRD peak matches well with $Na_{0.175}Bi_{0.825}O_{0.25}F_{2.15}$ phase. (For XRD curve of $Na_{0.175}Bi_{0.825}O_{0.25}F_{2.15}$, refer to Fig 6.1.4) For this reason, SWNTs solution dispersed in water with 1 w/v% SDS was used for BiF_3/SWNTs hybrid electrode. Nanoscale wiring using EC#2 virus with SWNTs pickup handle at one end showed improvement in capacity (Fig. 6.1.5), however, the improvement was not very significant as expected. For more insulating BiF_3, only nano-scale wiring is possibly not enough for full utilization of active materials and more intimate contact with conducting materials might be required for each particle. In addition, the surfactants used for SWNTs dispersion induced partial oxidation of BiF_3, which could be one of reason why the improvement is limited.(Fig. 6.1.4) For this matter, we tried to template BiF_3 on the virus coated with SWNTs on the major pVIII proteins. The SWNTs coated on the major protein of virus could serve as an own current collector for every particles deposited on the virus/SWNTs template. We have identified the peptide sequences that can bind with SWNTs on the pVIII protein through phage display with pVIII phage –display library. The identified phage with highest binding affinity to SWNTs was termed p8CS#3. By complex formation with p8CS#3, we could disperse SWNTs in the water without surfactants. If there is some way to use virus-SWNT complex to bio-mineralize such materials of interest, the complex can now serve as a new template for fabricating hybrid electrodes controlled in nano-scale. In order for the virus/SWNTs complex to serve as a template to biomineralize inorganic materials, pVIII proteins need to be modified further. We have noticed that negative charges on the virus surface can lead increased ionic interactions with cations as shown in the synthesis of Co_3O_4, Ag, and a-$FePO_4$. Therefore one possible option for pVIII protein modification is to induce more negative charges on the peptide exposed to the surface. Since the major pVIII coat proteins already have inserts for SWNTs binding, site-mutagenesis of pVIII protein was considered for further modification. Site-mutagenesis changes the DNA sequence and therefore changes amino-acid sequence, without inserting additional residues. This system can be called a dual-functional homoprotein. By mutating amino acids at the surface exposed position of pVIII protein with appropriate functional groups, we could nucleate appropriate materials on the major coat proteins, not pre-occupied by SWNTs, and create intimate contacts between biomineralized nanomaterials and SWNTs. This sit-mutagenesis is currently underway.

Chapter 6.1.2 Figures

Figure 6.1.1. TEM images of viral BiF_3 nanowires. (A) Low magnification: 10K. (B) Higher magnification: 41K. Close examination revealed primary particle size as 10-15 nm, however particles aggregated to secondary structures with size of 30-50 nm.

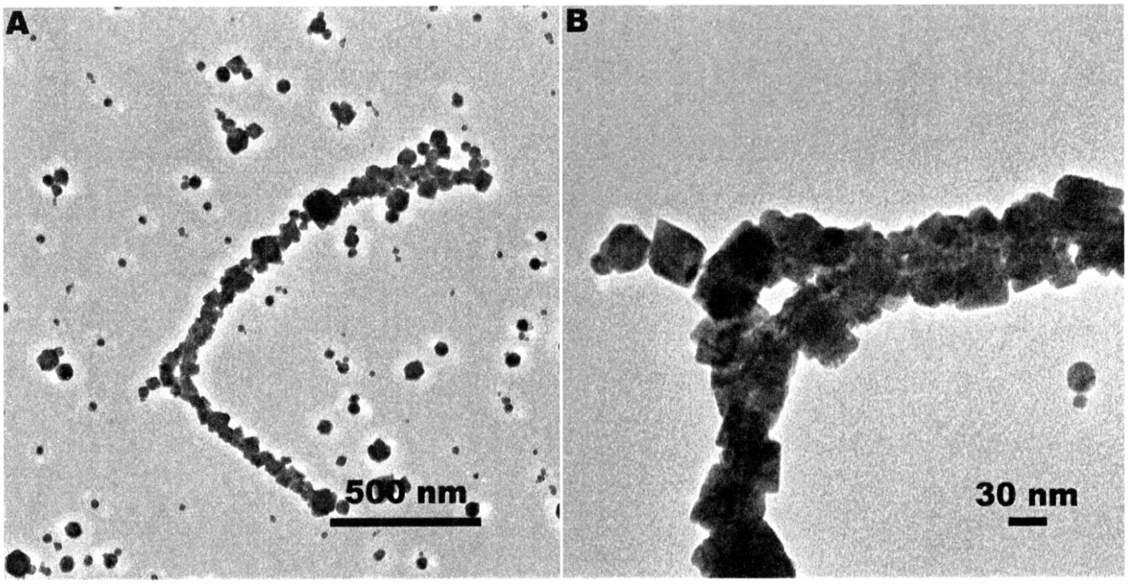

Figure 6.1.2. Xray powder diffraction (XRD) of BiF_3

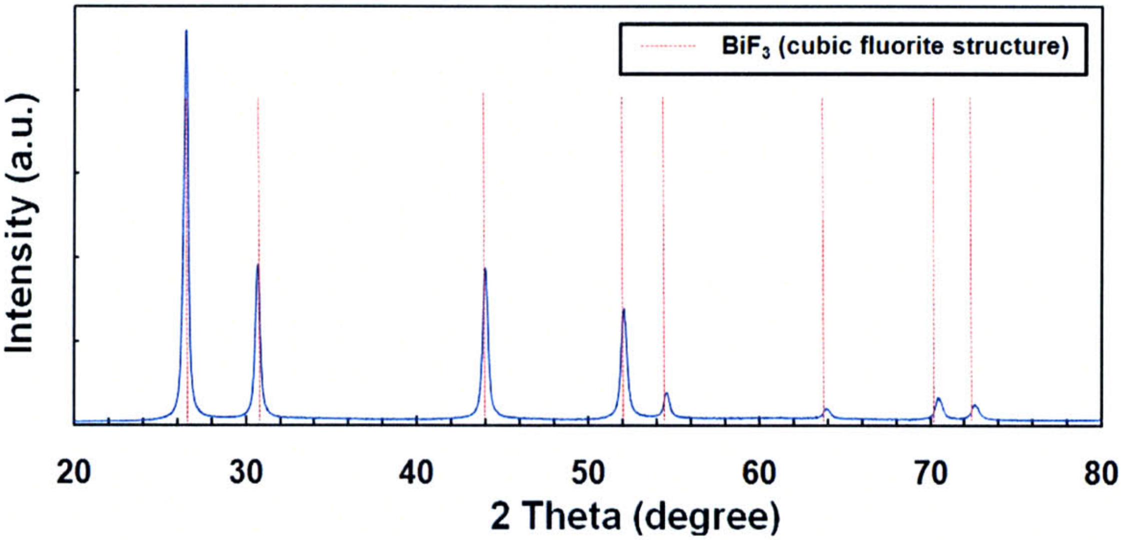

Figure 6.1.3. Electrochemical performances of synthesized c-BiF_3 tested between 2.0 and 4.5 V. (A) First discharge curves at C/5 rate. First discharge curves of c-BiF_3 synthesized with different precursor concentration ratio of Bi^{+3}: F^-=1:20, 1:5 and 1:1 are presented. (B) First discharge/charge curves of viral c-BiF_3 nanowires synthesized with precursor concentration ratio of 1: 20 at C/5 rate. (C) Rate performance of c-BiF_3 viral nanowires synthesized with and without virus. Precursor concentration ratio was 1:20.

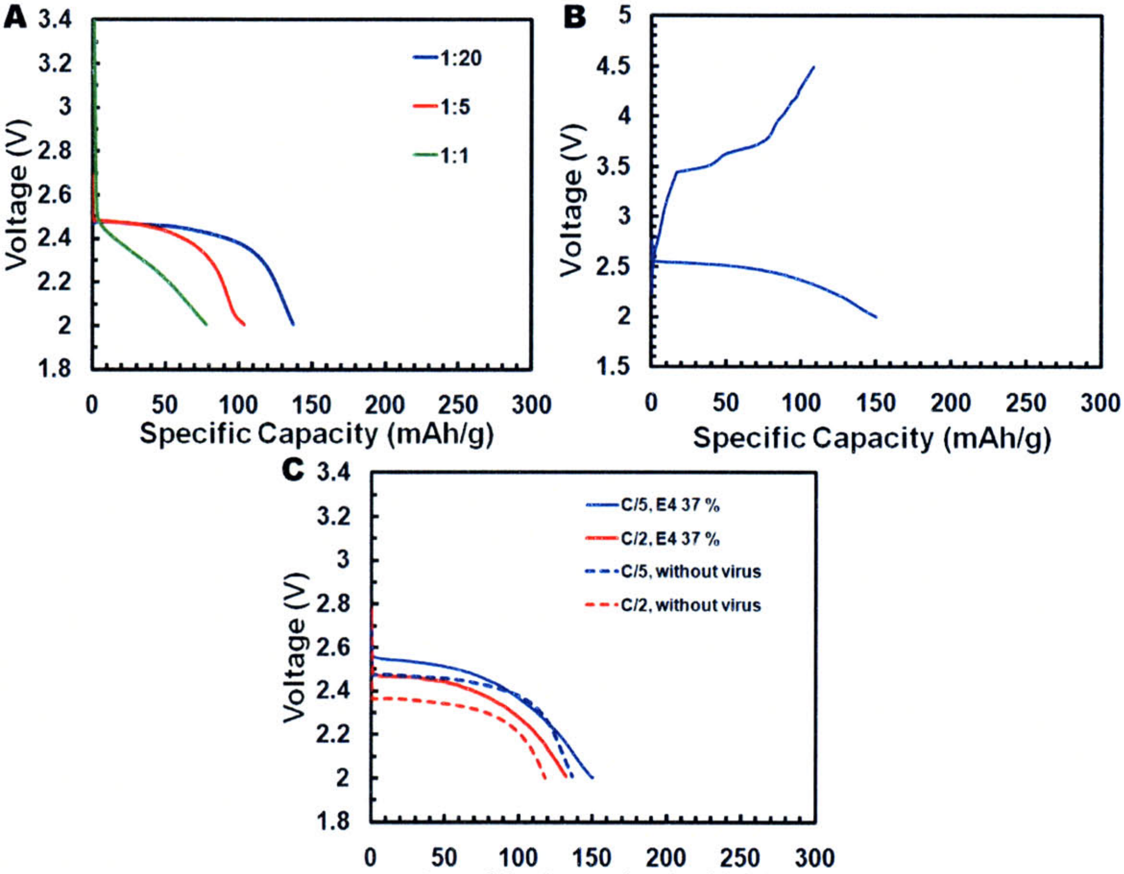

Figure 6.1.4. Xray powder diffraction (XRD) of BiF_3 mixed with surfactant solution of (A) 2 w/v% SC (sodium cholate) solution. Volume ratio of BiF_3 solution to SC solution was 1:1. (B) 1 w/v% SDS (sodium dodecyl sulfate) solution. Volume ratio Volume ratio of BiF_3 solution to SDS solution was 1:1. XRD curve of BiF3 synthesized in pure water was shown for comparison.

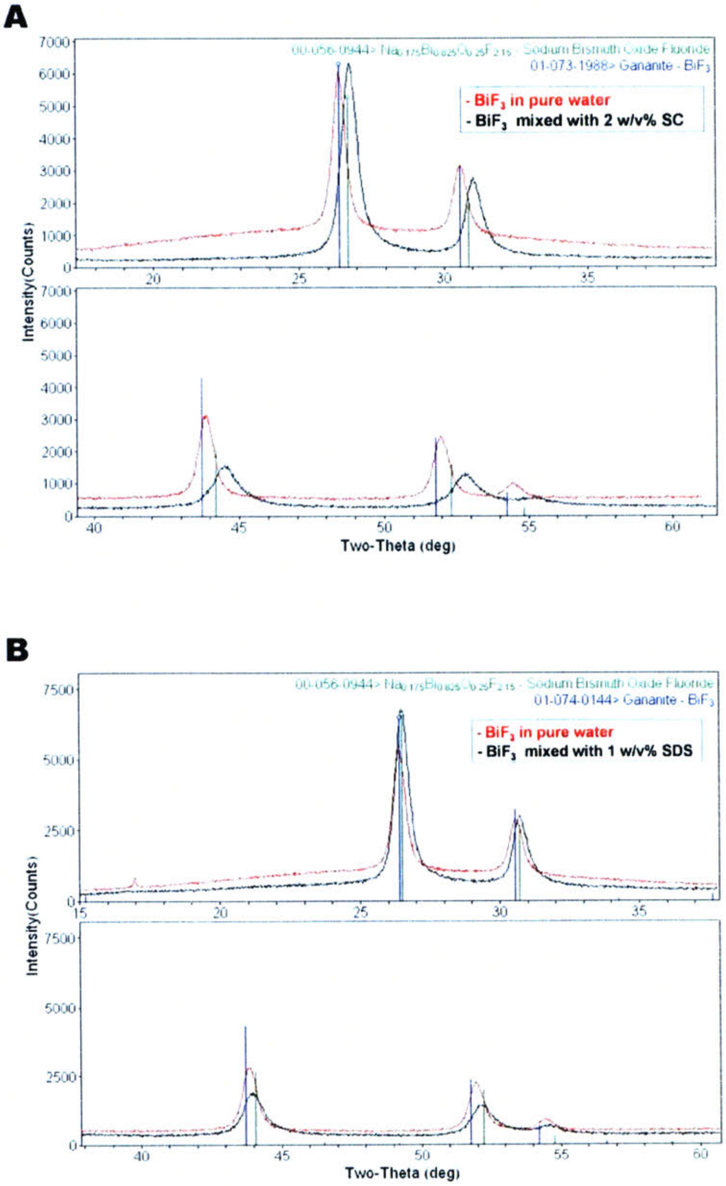

Figure 6.1.5. First discharge curve of BiF_3/SWNTs hybrid electrodes. SWNTs were dispersed in water with 1 w/v% SDS surfactants. The first discharge curve of BiF_3 electrode prepared by mixing with Super P carbon 25% is also presented for comparison.

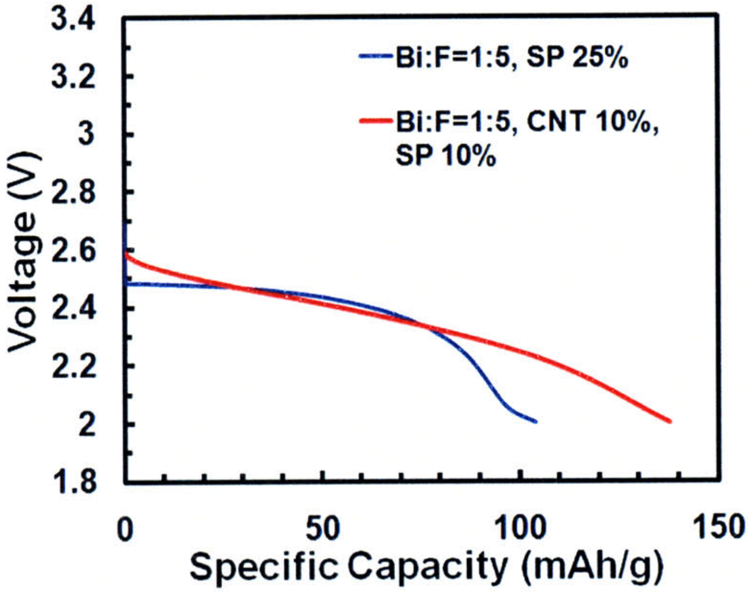

Chapter 6.2 Nanoparticles synthesis using biological nanoreactor – protein cages

Chapter 6.2.1. Preliminary results and future works

Lithium manganese phosphate ($LiMnPO_4$) is also a very promising cathode material for high power applications, since its potential (4.1V vs. Li^+/Li) is higher than iron phosphate materials. Unfortunately, kinetic limitations in $LiMnPO_4$ are even worse than iron phosphates and the good performance has not yet been demonstrated. The most effective experimental approach reported so far is the use of small particles to improve rate performance[97]. However, the particle size still remains in the order of 100 nm.

In this research, we have tried to synthesize nanostructured particles with variable particle size ranging from 1~50 nm by using a so-called nanoreactor, which is a size constrained reaction vessel. In our synthesis, polystyrene-b-pol(4-vinylpyridine) di-block copolymer(BCP) micelles were used as a nanoreactor. Diblock copolymer micelles have been explored as nanoreactors for the synthesis of ordered metallic nanoparticles[98] and gallium nitride (GaN)[99] arrays. Here, the BCP method was studied as a method to fabricate nanostructured cathodes for lithium rechargeable batteries, with multi-component and high temperature phase particles of below 10 nm in diameter. Compared to conventional soft chemistry and sol-gel synthesis methods, advantage of the BCP synthesis is that nanostructured particles of high temperature phases can be made with in-situ surface carbon coating of individual particles. The BCP method started with the formation of reverse micelle structures in the non-polar solvent such as toluene. First, 0.2g of PS-P4VP (M_n-PS-b-P4VP, 20000-b-19000) was added to 60 ml of toluene and stirred at 80°C for 4hours. Resulting clear solution contained reverse micelles with P4VP domains in the core. Then, precursors of each component were added to this solution. For the

$LiMnPO_4$ synthesis, H_3PO_4 aqueous stock solution (85w%), 1 M LiOH aqueous solution, and 1 M $Mn(CH_3COO)_2$ aqueous solution were used. Each precursor was added separately in the order of $H_3PO_4 \rightarrow LiOH \rightarrow Mn(CH_3COO)_2$ or $H_3PO_4 \rightarrow Mn(CH_3COO)_2 \rightarrow LiOH$. Final concentration of each precursors are H_3PO: LiOH: $Mn(CH_3COO)_2$=2mM: 1mM: or 1 mM: 0.5mM: 0.5mM. Each precursor was stirred for 12 hours at room temperature before adding next precursor. Polar precursors were secluded within the core of the reverse micelles.

The reverse micelles that were loaded with these aqueous precursors were deposited directly on the current collector of the cathode. Stainless steel was used as a current collector. After depositing and evaporating the toluene solvent, the cathode system was annealed under N_2 atmosphere at 600 °C for 3 hours without any plasma treatment. Figure 6.2.1A is the result of XRD analysis after annealing. Except from a few peaks from the stainless steel substrate, all the peaks were identified as $LiMnPO_4$ and no other crystalline impurity phases were found. In Fig. 6.2.1B particle size was 1.5~5 nm and crystallinity of these small particles was also confirmed by HRTEM. For some particles, thin amorphous carbonaceous residue layer could be found.

This annealed cathode system was used as a cathode for a lithium rechargeable battery without further processing such as ball milling or mixing with carbon and polymer binder. The result on stainless steel current collector was shown in Fig. 6.2.2. With the assumption of preliminary determined weight, the system showed unusually small polarization during charging/discharging indicating good ionic and electronic conductivity. However, when the stainless steel current collector was used, side reactions including oxidation of stainless steel were unavoidable during the annealing step. This leaded to initial irreversible capacity during the electrochemical test and made determination of active mass difficult. Therefore, platinum was tested to avoid these deleterious side reactions. The particles deposited on platinum current collector was pure crystalline $LiMnPO_4$ and there was no signal of oxidation from substrate (Fig. 6.2.3A) Total materials loading was determined by subtracting initial Pt substrate weight from the mass of Pt substrate and $LiMnPO_4$ after anneal. The $LiMnPO_4$ on Pt showed almost 97% theoretical capacity at the first charge at C/8.3 rate.(Fig. 6.2.3) However, the particles were detached from the platinum during the first charge process, showing almost zero discharge capacity. (Fig. 6.2.3C) The adhesion of $LiMnPO_4$ powder deposited and Pt substrate could not be improved by hot pressing and deposition of polyelectrolyte layers. (LPEI + PAA)

The electrochemical activity of $LiMnPO_4$ nanoparticles synthesized using BCP nanoreactors showed the possibility that performances of $LiMnPO_4$ could be greatly enhanced when the size of particles is in the nanometer range. However, BCP methods involved a toxic solvent (toluene) and block copolymer synthesis. In addition, since aqueous precursor solutions were added to the non-polar toluene solvent, the precursor loading into the micelles was low, thus leading a low yield problem.

Ferritin is a well-known biological nanoreactor. In nature, ferritin proteins function to sequester and store iron. These proteins are composed of 24 subunits that interact to form a spherical protein complex with a hollow cavity. The outer diameter of ferritin is ~12nm and the inner cavity of ~8 nm in diameter can store up to 4500 iron atoms as an iron oxide-hydroxide[100, 101]. These supramolecular structures represent a novel reaction vessel for the synthesis of inorganic materials with controlled dimensions. The nucleation and growth from various precursor ions suggest that inorganic materials other than iron oxide may be developed within the core of ferritin[102]. Inorganic nanoparticles (other than iron oxides) such as Mn_3O_4, Co_3O_4, $Cr(OH)_2$, $Ni(OH)_3$, In_2O_3, CdS, ZnSe have been prepared within apo-ferrtin[102, 103] Along with iron, ferritin also accumulates phosphate within the ferritin mineral core[101]. Therefore, this biological nanoreactor could offer size constrained reaction environments for $LiMnPO_4$. In this study, possibility of crystalline $LiMnPO_4$ synthesis was tested using ferritin protein cages. Figure 6.2.4 shows preliminary results. For the synthesis, 100 mM, 1ml of LiH_2PO_4 aqueous solution (pH=7.0, pH adjusted with 1M LiOH) was injected for 1 hour using syringe pump to aqueous mixture of 20 mM, 1 ml $MnCl_2 \cdot 4H_2O$ and 10 uM, 1ml ferritin solution. The resultant solution was dialyzed against water for overnight to remove remaining ions in the solution. In Fig. 6.2.4A, the dialyzed solution was dried on the glass substrate under vacuum and 600℃, 3 hours anneal under Ar atmosphere was followed for the crystallization. As shown in the XRD curve, $Mn_2P_2O_7$ and Mn_3O_4 were formed which indicate that only Mn^{2+} ions and $PO4^{3-}$ ions were penetrated though the channel of ferritin and accumulated. In addition, there are some ferritins that only accumulated Mn^{2+} ions not $PO4^{3-}$ ions. To incorporate lithium in the structure, stoichiometric $Li(CH_3COO)$ (3 M, 7 ul) was added to the dialyzed solution before drying and annealing. In Fig. 6.2.4B, $LiMnPO_4$ phase was formed but also various impurity phases such as MnO and Li_3PO_4 were also generated. These impurity phase formation could be related to non-uniform precursor loading into the ferritin core. Ferritin that only accumulated Mn^{2+} ions in the core could result MnO phase and ferritin that only contained PO_4^{3-} could generate Li_3PO_4 phase. In Fig. 6.2.4C, the solution was dried and annealed without dialysis. In this case, $LiMnPO_4$ and $Li_4P_2O_7$ were synthesized since excess Li^+ and $PO_4{}^{3-}$ added as a LiH_2PO_4 precursor were still remained. From these preliminary results, more research should be done to make uniform precursor loading into the ferritin core and find the appropriate synthesis procedure/precursor ratios to make correct stoichiometric $LiMnPO_4$ compound.

Chapter 6.2.2 Figures

Figure 6.2.1. Structural characterization of $LiMnPO_4$ deposited and annealed on stainless steel (S.S) substrate (A) XRD of annealed $LiMnPO_4$ (B) HRTEM and low magnification TEM images of annealed sample

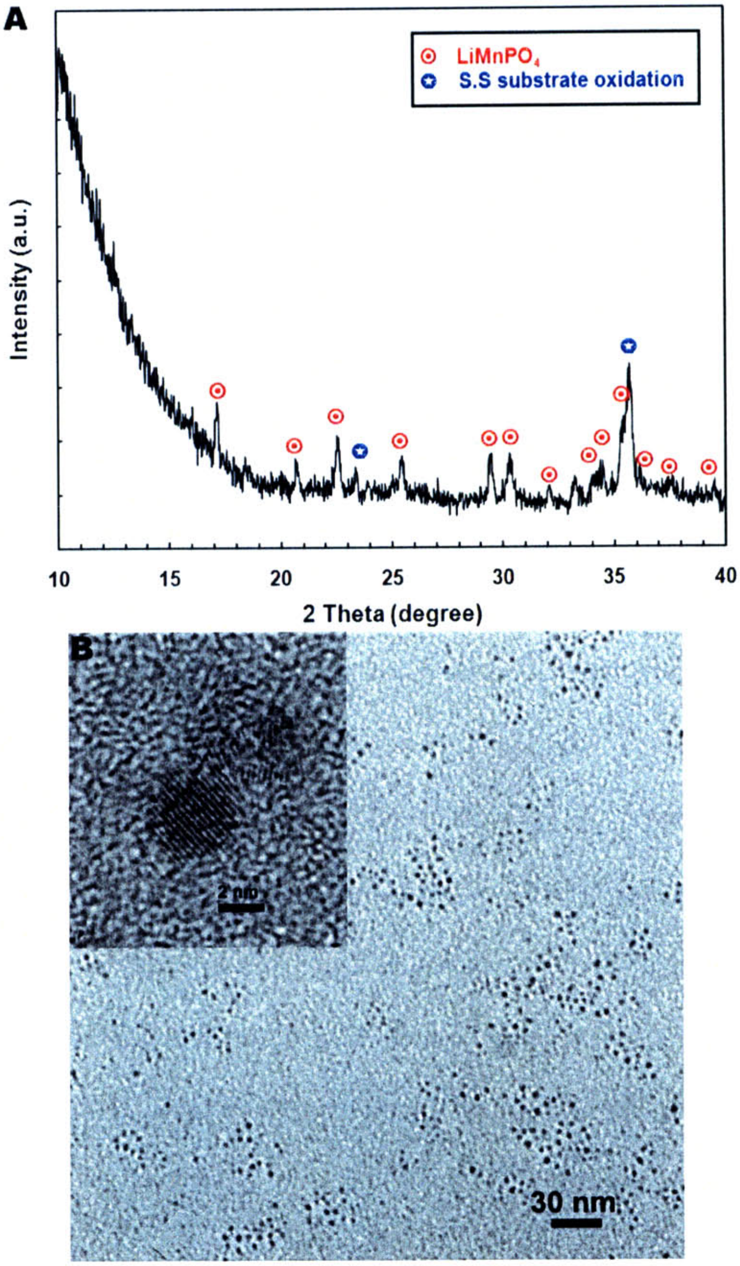

Figure 6.2.2. (A) Rate capability (B) First Charge/Discharge curve of 2C-like rate of LiMnPO$_4$ synthesized by BCP method

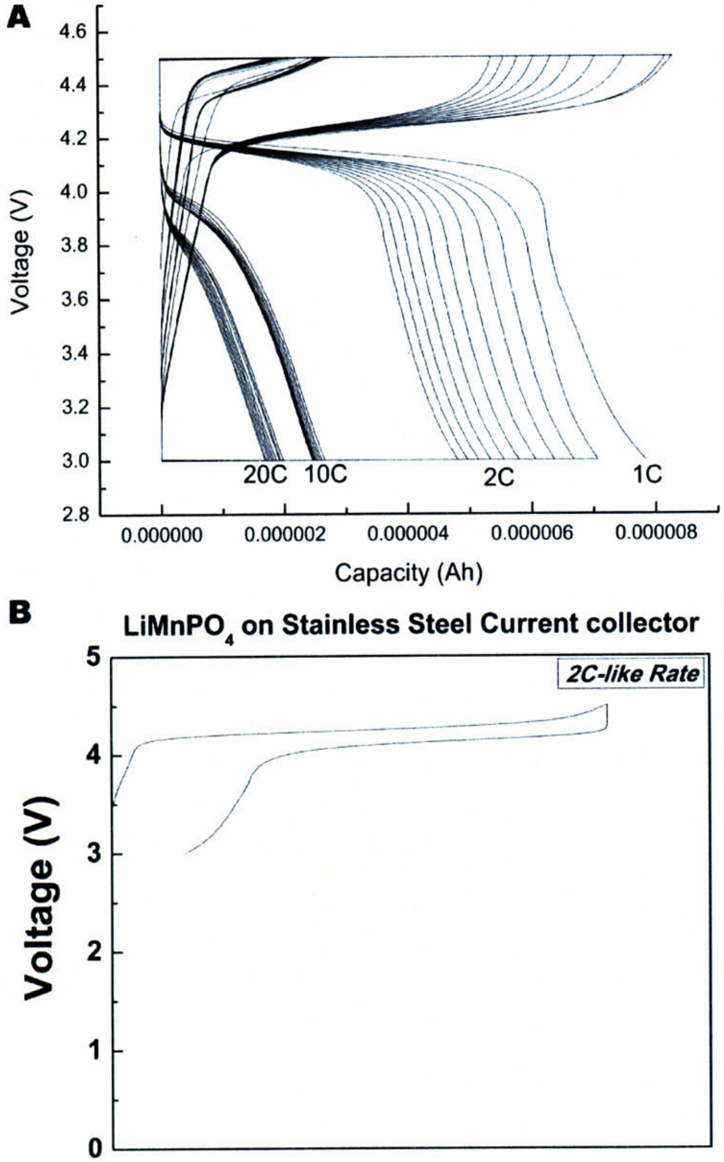

Figure 6.2.3. Structural characterization of $LiMnPO_4$ deposited and annealed on Pt substrate (A) XRD of annealed $LiMnPO_4$. (B) First charge/discharge curve of annealed sample tested between 2.3 and 4.5 V at C/8.3 rate. Total materials loading ($LiMnPO_4$ + C) was 0.83 mg. (C) Picture of the same sample: after deposition→after anneal→after electrochemical test.

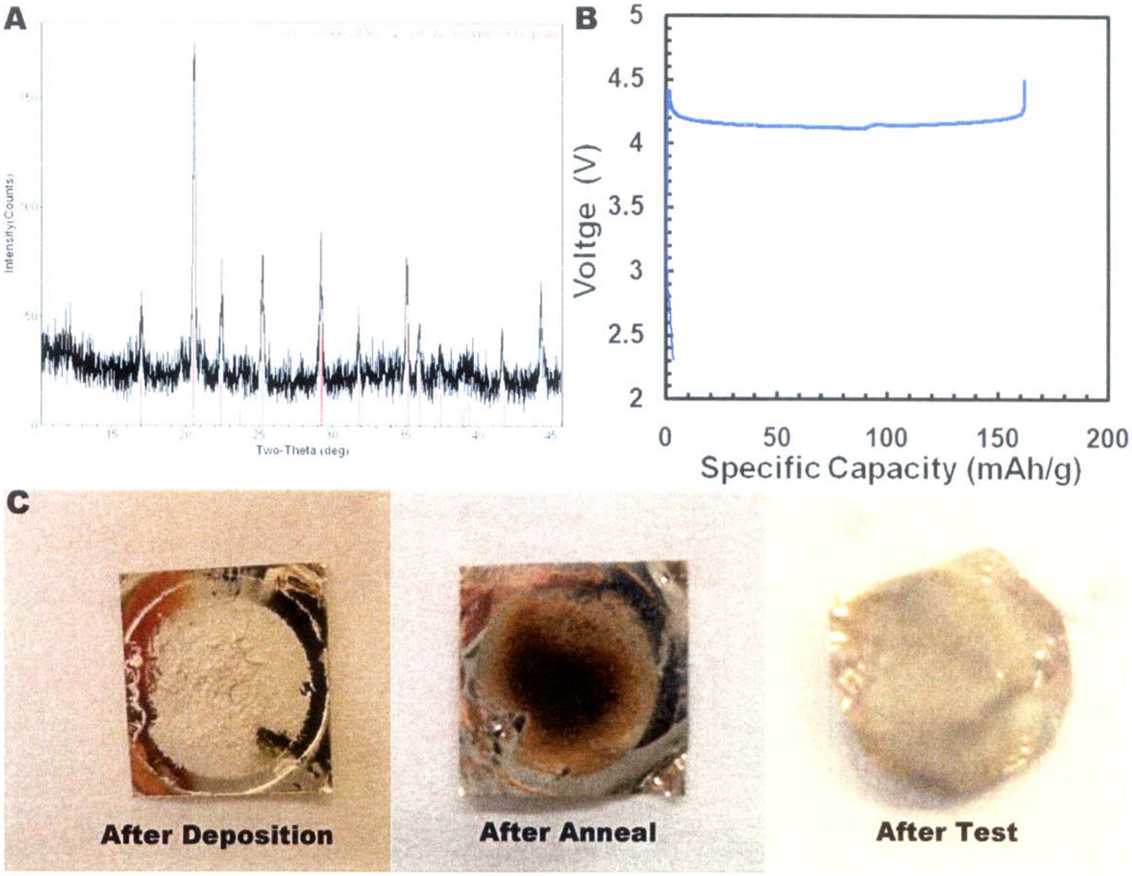

Figure 6.2.4 Preliminary results of $LiMnPO_4$ synthesis using ferritine cage: XRD curves of the solution mixture described in the text (A) anneal after dialysis and drying (B) anneal after dialysis and 3 M, 7 ul $Li(CH_3COO)$ addition, then drying (C) anneal after drying without dialysis.

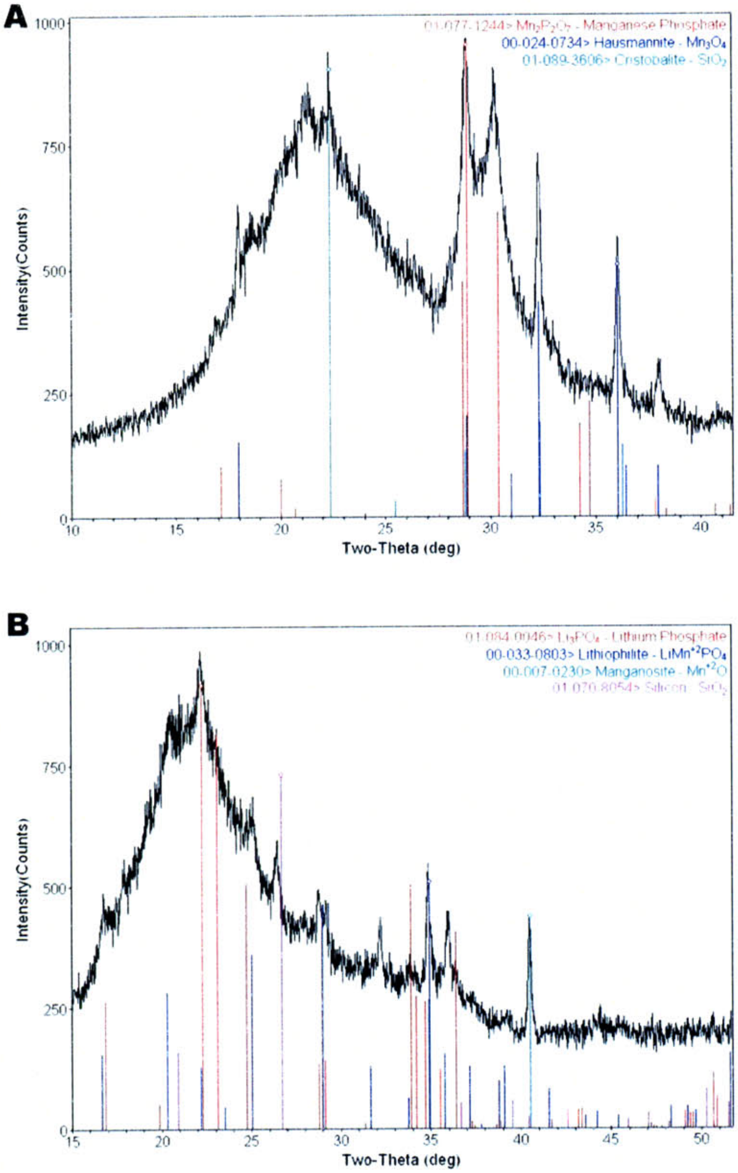

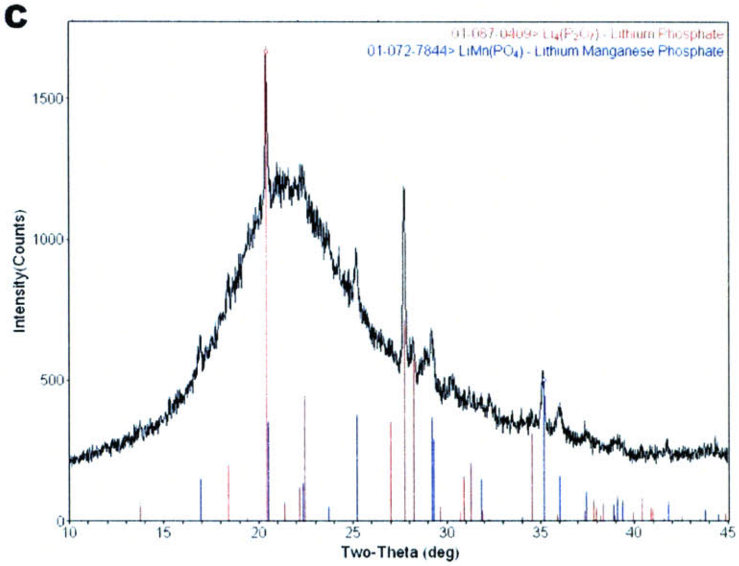
c
01-067-0409> $Li_4(P_2O_7)$ - Lithium Phosphate
01-072-7844> $LiMn(PO_4)$ - Lithium Manganese Phosphate
Intensity(Counts)
1500
1000
500
0
10
15
20
25
30
35
40
45
Two-Theta (deg)

References

1. Mann, S. *Biomimietic Materials Chemistry*, VCH:New York (1996).
2. Weiner, S., Addadi, L. & Wagner, H.D. Materials design in biology. *Materials Science & Engineering C-Biomimetic and Supramolecular Systems* 11, 1-8 (2000).
3. Poulsen, N., Sumper, M. & Kroger, N. Biosilica formation in diatoms: Characterization of native silaffin-2 and its role in silica morphogenesis. *Proceedings of the National Academy of Sciences of the United States of America* 100, 12075-12080 (2003).
4. Cha, J.N. et al. Silicatein filaments and subunits from a marine sponge direct the polymerization of silica and silicones in vitro. *Proceedings of the National Academy of Sciences of the United States of America* 96, 361-365 (1999).
5. Scheffel, A. et al. An acidic protein aligns magnetosomes along a filamentous structure in magnetotactic bacteria. *Nature* 440, 110-114 (2006).
6. Brown, S. Metal-recognition by repeating polypeptides. *Nature Biotechnology* 15, 269-272 (1997).
7. Whaley, S.R., English, D.S., Hu, E.L., Barbara, P.F. & Belcher, A.M. Selection of peptides with semiconductor binding specificity for directed nanocrystal assembly. *Nature* 405, 665-668 (2000).
8. Sarikaya, M., Tamerler, C., Jen, A.K.Y., Schulten, K. & Baneyx, F. Molecular biomimetics: nanotechnology through biology. *Nature Materials* 2, 577-585 (2003).
9. Lee, S.W., Mao, C.B., Flynn, C.E. & Belcher, A.M. Ordering of quantum dots using genetically engineered viruses. *Science* 296, 892-895 (2002).
10. Mao, C.B. et al. Virus-based toolkit for the directed synthesis of magnetic and semiconducting nanowires. *Science* 303, 213-217 (2004).
11. Nam, K.T., Peelle, B.R., Lee, S.W. & Belcher, A.M. Genetically driven assembly of nanorings based on the M13 virus. *Nano Letters* 4, 23-27 (2004).
12. Huang, Y. et al. Programmable assembly of nanoarchitectures using genetically engineered viruses. *Nano Letters* 5, 1429-1434 (2005).
13. Nam, K.T. et al. Virus-enabled synthesis and assembly of nanowires for lithium ion battery electrodes. *Science* 312, 885-888 (2006).
14. Yoo, P.J. et al. Spontaneous assembly of viruses on multilayered polymer surfaces. *Nature Materials* 5, 234-240 (2006).
15. Chiang, C.Y. et al. Weaving genetically engineered functionality into mechanically robust virus fibers. *Advanced Materials* 19, 826-+ (2007).
16. Kay, B.K., Winter, J , McCafferty, J *Phage Display of Peptides and Proteins: A Laboratory Manual* (1996).
17. Lee, S.K., Yun, D.S. & Belcher, A.M. Cobalt ion mediated self-assembly of genetically engineered bacteriophage for biomimetic Co-Pt hybrid material. *Biomacromolecules* 7, 14-17 (2006).

18. Nam, K.T., Lee, Y.J., Krauland, E.M., Kottmann, S.T. & Belcher, A.M. Peptide-mediated reduction of silver ions on engineered biological scaffolds. *Acs Nano* 2, 1480-1486 (2008).
19. Armand, M. & Tarascon, J.M. Building better batteries. *Nature* 451, 652-657 (2008).
20. Nam, K.T. et al. Stamped microbattery electrodes based on self-assembled M13 viruses. *Proceedings of the National Academy of Sciences of the United States of America* 105, 17227-17231 (2008).
21. Khalil, A.S. et al. Single M13 bacteriophage tethering and stretching. *Proceedings of the National Academy of Sciences of the United States of America* 104, 4892-4897 (2007).
22. Klaus, T., Joerger, R., Olsson, E. & Granqvist, C.G. Silver-based crystalline nanoparticles, microbially fabricated. *Proceedings of the National Academy of Sciences of the United States of America* 96, 13611-13614 (1999).
23. Mukherjee, P. et al. Fungus-mediated synthesis of silver nanoparticles and their immobilization in the mycelial matrix: A novel biological approach to nanoparticle synthesis. *Nano Letters* 1, 515-519 (2001).
24. Naik, R.R., Stringer, S.J., Agarwal, G., Jones, S.E. & Stone, M.O. Biomimetic synthesis and patterning of silver nanoparticles. *Nature Materials* 1, 169-172 (2002).
25. Selvakannan, P.R. et al. Synthesis of aqueous Au core-Ag shell nanoparticles using tyrosine as a pH-dependent reducing agent and assembling phase-transferred silver nanoparticles at the air-water interface. *Langmuir* 20, 7825-7836 (2004).
26. Peelle, B.R., Krauland, E.M., Wittrup, K.D. & Belcher, A.M. Design criteria for engineering inorganic material-specific peptides. *Langmuir* 21, 6929-6933 (2005).
27. Clay, R.T. & Cohen, R.E. Synthesis of metal nanoclusters within microphase-separated diblock copolymers: sodium carboxylate vs carboxylic acid functionalization. *Supramol. Sci.* 5, 41-48 (1998).
28. Ghosh, S.K., Kundu, S., Mandal, M., Nath, S. & Pal, T. Studies on the evolution of silver nanoparticles in micelle by UV-photoactivation. *Journal of Nanoparticle Research* 5, 577-587 (2003).
29. Joly, S. et al. Multilayer nanoreactors for metallic and semiconducting particles. *Langmuir* 16, 1354-1359 (2000).
30. Esumi, K., Suzuki, A., Yamahira, A. & Torigoe, K. Role of poly(amidoamine) dendrimers for preparing nanoparticles of gold, platinum, and silver. *Langmuir* 16, 2604-2608 (2000).
31. Henglein, A. Reduction of Ag(CN)(2)(-) on silver and platinum colloidal nanoparticles. *Langmuir* 17, 2329-2333 (2001).
32. Dujardin, E., Peet, C., Stubbs, G., Culver, J.M. & Mann, S. Organization of Metallic Nanoparticles Using Tobacco Mosaic Virus Templates. *Nano Lett.* 3, 413-417 (2003).
33. Esumi, K., Hosoya, T., Suzuki, A. & Torigoe, K. Formation of gold and silver nanoparticles in aqueous solution of sugar-persubstituted poly(amidoamine) dendrimers. *J. Colloid Interface Sci.* 226, 346-352 (2000).
34. Huang, H.Z. & Yang, X.R. synthesis of polysaccharide-stabilized gold and silver nanoparticles: a green method. *Carbohydr. Res.* 339, 2627-2631 (2004).
35. Yonezawa, Y. et al. Photochemical Formation of Silver Metal-Films from Silver Salt of Natural High Molecular Carboxylic-Acid. *J. Appl. Phys.* 68, 1297-1302 (1990).

36. Maillard, M., Huang, P.R. & Brus, L. Silver nanodisk growth by surface plasmon enhanced photoreduction of adsorbed [Ag+]. *Nano Lett.* 3, 1611-1615 (2003).
37. Rybak, B.M., Ornatska, M., Bergman, K.N., Genson, K.L. & Tsukruk, V.V. Formation of silver nanoparticles at the air-water interface mediated by a monolayer of functionalized hyperbranched molecules. *Langmuir* 22, 1027-1037 (2006).
38. Iloukhani, H. & Bahrami, H. Kinetic studies and mechanism on the permanganic oxidation of L-glutamine in strong acid medium in the presence and absence of silver (I). *Int. J. Chem. Kinet.* 31, 95-102 (1999).
39. Paik, D.H., Lee, I.-R., Yang, D.-S., Baskin, J.S. & Zewail, A.H. Electrons in Finite-Sized Water Cavities: Hydration Dynamics Observed in Real Time. *Science* 306, 671-675 (2004).
40. Faust, B.C. & Zepp, R.G. Photochemistry of Aqueous Iron(Iii) Polycarboxylate Complexes - Roles in the Chemistry of Atmospheric and Surface Waters. *Environmental Science & Technology* 27, 2517-2522 (1993).
41. Shoeib, T., Siu, K.W.M. & Hopkinson, A.C. Silver ion binding energies of amino acids: Use of theory to assess the validity of experimental silver ion basicities obtained from the kinetic method. *J. Phys. Chem. A* 106, 6121-6128 (2002).
42. Henglein, A. Small-particle research: physicochemical properties of extremely small colloidal metal and semiconductor particles. *Chem. Rev.* 89, 1861-1873 (1989).
43. Keizer, J. Theory of Rapid Biomolecular Reactions in Solution and Membranes. *Acc. Chem. Res.* 18, 235-241 (1985).
44. Castanho, M.A.R.B. & Fernandes, M.X. Lipid membrane-induced optimization for ligand-receptor docking: recent tools and insight for the "membrane catalysis" model. *Eur. Biophys. J.* 35, 92-103 (2006).
45. Mallick, K., Jewrajka, S., Pradhan, N. & Pal, T. Micelle-catalysed redox reaction. *Current Science* 80, 1408-1412 (2001).
46. Ghosh, S.K., Kundu, S., Mandal, M. & Pal, T. Silver and gold nanocluster catalyzed reduction of methylene blue by arsine in a micellar medium. *Langmuir* 18, 8756-8760 (2002).
47. Hardt, S.L. RATES OF DIFFUSION CONTROLLED REACTIONS IN ONE, 2 AND 3 DIMENSIONS. *Biophysical Chemistry* 10, 239-243 (1979).
48. Laszlo, P. CATALYSIS OF ORGANIC-REACTIONS BY INORGANIC SOLIDS. *Accounts of Chemical Research* 19, 121-127 (1986).
49. Lee, S.-Y., Royston, E., Culver, J.M. & Harris, M.T. Improved metal cluster deposition on a genetically engineered tobacco mosaic virus template. *Nanotechnology* 16, S435-S441 (2005).
50. Barbas, C.F. Phage display : a laboratory manual. (Cold Spring Harbor Laboratory Press, Cold Spring Harbor, NY; 2001).
51. Graff, A., Wagner, D., Ditlbacher, H. & Kreibig, U. Silver nanowires. *European Physical Journal D* 34, 263-269 (2005).
52. Gilbert, P.U.P.A., Abrecht, M. & Frazer, B.H. The organic-mineral interface in biominerals. *Molecular Geomicrobiology* 59, 157-185 (2005).
53. Bruce, P.G., Scrosati, B. & Tarascon, J.M. Nanomaterials for rechargeable lithium batteries. *Angewandte Chemie-International Edition* 47, 2930-2946 (2008).

54. Chung, S.Y., Bloking, J.T. & Chiang, Y.M. Electronically conductive phospho-olivines as lithium storage electrodes. *Nature Materials* 1, 123-128 (2002).
55. Delacourt, C., Poizot, P., Levasseur, S. & Masquelier, C. Size effects on carbon-free LiFePO4 powders. *Electrochem. Solid State Lett.* 9, A352-A355 (2006).
56. Kim, D.H. & Kim, J. Synthesis of LiFePO4 nanoparticles in polyol medium and their electrochemical properties. *Electrochem. Solid State Lett.* 9, A439-A442 (2006).
57. Tarascon, J.M. et al. Various strategies to tune the ionic/electronic properties of electrode materialst. *Dalton Trans.*, 2988-2994 (2004).
58. Croce, F. et al. A novel concept for the synthesis of an improved LiFePO4 lithium battery cathode. *Electrochem. Solid State Lett.* 5, A47-A50 (2002).
59. Hu, Y.S. et al. Improved electrode performance of porous LiFePO4 using RuO2 as an oxidic nanoscale interconnect. *Advanced Materials* 19, 1963-1966 (2007).
60. Shi, Z.C. et al. Synthesis, characterization and electrochemical performance of mesoporous FePO4 as cathode material for rechargeable lithium batteries. *Electrochimica Acta* 53, 2665-2673 (2008).
61. Prosini, P.P. et al. Synthesis and characterization of amorphous hydrated FePO4 and its electrode performance in lithium batteries. *Journal of the Electrochemical Society* 149, A297-A301 (2002).
62. Hong, Y.S. et al. Amorphous FePO4 as 3 V cathode material for lithium secondary batteries. *Journal of Materials Chemistry* 12, 1870-1874 (2002).
63. Song, Y.N., Yang, S.F., Zavalij, P.Y. & Whittingham, M.S. Temperature-dependent properties of FePO4 cathode materials. *Materials Research Bulletin* 37, 1249-1257 (2002).
64. Sheem, K., Lee, Y.H. & Lim, H.S. High-density positive electrodes containing carbon nanotubes for use in Li-ion cells. *Journal of Power Sources* 158, 1425-1430 (2006).
65. Kang, K.S., Meng, Y.S., Breger, J., Grey, C.P. & Ceder, G. Electrodes with high power and high capacity for rechargeable lithium batteries. *Science* 311, 977-980 (2006).
66. Ahn, S. High capacity, high rate lithium-ion battery electrodes utilizing fibrous conductive additives. *Electrochem. Solid State Lett.* 1, 111-113 (1998).
67. Sakamoto, J.S. & Dunn, B. Vanadium oxide-carbon nanotube composite electrodes for use in secondary lithium batteries. *Journal of the Electrochemical Society* 149, A26-A30 (2002).
68. O'Connell, M.J. et al. Band gap fluorescence from individual single-walled carbon nanotubes. *Science* 297, 593-596 (2002).
69. Wu, Z.C. et al. Transparent, conductive carbon nanotube films. *Science* 305, 1273-1276 (2004).
70. Wang, S.Q. et al. Peptides with selective affinity for carbon nanotubes. *Nature Materials* 2, 196-200 (2003).
71. Zheng, M. et al. Structure-based carbon nanotube sorting by sequence-dependent DNA assembly. *Science* 302, 1545-1548 (2003).
72. Ryan, E. *US patent* (2002).
73. Sanghvi, A.B., Miller, K.P.H., Belcher, A.M. & Schmidt, C.E. Biomaterials functionalization using a novel peptide that selectively binds to a conducting polymer. *Nature Materials* 4, 496-502 (2005).

74. Hopp, T.P. & Woods, K.R. Prediction of Protein Antigenic Determinants from Amino-Acid-Sequences. *Proceedings of the National Academy of Sciences of the United States of America-Biological Sciences* 78, 3824-3828 (1981).
75. Moore, V.C. et al. Individually suspended single-walled carbon nanotubes in various surfactants. *Nano Letters* 3, 1379-1382 (2003).
76. Kavan, L. Enhancement of electrochemical activity of LiFePO4 (olivine) by amphiphilic Ru-bipyridine complex anchored to a carbon nanotube. *Chemistry of Materials* 19, 4716-4721 (2007).
77. Wang, Q., Evans, N., Zakeeruddin, S.M., Exnar, I. & Gratzel, M. Molecular wiring of insulators: Charging and discharging electrode materials for high-energy lithium-ion batteries by molecular charge transport layers. *Journal of the American Chemical Society* 129, 3163-3167 (2007).
78. Yin, J.T. et al. New Ag-Sn alloy anode materials for lithium-ion batteries. *Journal of the Electrochemical Society* 150, A1129-A1135 (2003).
79. Laik, B. et al. Silicon nanowires as negative electrode for lithium-ion microbatteries. *Electrochimica Acta* 53, 5528-5532 (2008).
80. Chan, C.K. et al. High-performance lithium battery anodes using silicon nanowires. *Nature Nanotechnology* 3, 31-35 (2008).
81. Taillades, G., Benjelloun, N., Sarradin, J. & Ribes, M. Metal-based very thin film anodes for lithium ion microbatteries. *Solid State Ionics* 152, 119-124 (2002).
82. Massalski, T.B. (ed.) Binary Alloy Phase Diagrams, Vol. 1, Edn. II. (Materials Park, Ohio : ASM International, 1990).
83. Massalski, T.B. (ed.) Binary Alloy Phase Diagrams, Vol. 1, Edn. 1. (Materials Park, Ohio : ASM International, 1990).
84. Taillades, G. & Sarradin, J. Silver: high performance anode for thin film lithium ion batteries. *Journal of Power Sources* 125, 199-205 (2004).
85. Morales, J., Sanchez, L., Martin, F., Ramos-Barrado, J.R. & Sanchez, M. Synthesis, characterization, and electrochemical properties of nanocrystalline silver thin films obtained by spray pyrolysis. *Journal of the Electrochemical Society* 151, A151-A157 (2004).
86. Yuan, L. et al. Mesoporous gold as anode material for lithium-ion cells. *J. New Mat.Electrochem. Syst.* 10, 95-99 (2007).
87. Park, M.S. et al. Preparation and electrochemical properties of SnO2 nanowires for application in lithium-ion batteries. *Angew. Chem.-Int. Edit.* 46, 750-753 (2007).
88. Lee, Y.J. et al. Fabricating Genetically Engineered High-Power Lithium-Ion Batteries Using Multiple Virus Genes. *Science* 324, 1051-1055 (2009).
89. Lee, Y., Kim, J. H.,Yun, D.S., Nam, Y.S. , Yang, S.H. and Belcher, A.M. *submitted* (2009).
90. Huggins, R.A. Lithium alloy negative electrodes. *Journal of Power Sources* 81, 13-19 (1999).
91. Idota, Y., Kubota, T., Matsufuji, A., Maekawa, Y. & Miyasaka, T. Tin-based amorphous oxide: A high-capacity lithium-ion-storage material. *Science* 276, 1395-1397 (1997).
92. Kwon, Y., Kim, H., Doo, S.G. & Cho, J.H. Sn0.9Si0.1/carbon core-shell nanoparticles for high-density lithium storage materials. *Chemistry of Materials* 19, 982-986 (2007).

93. http://www.asminternational.org/asmenterprise/APD/ViewAPD.aspx?id=900032.
94. http://www.asminternational.org/asmenterprise/APD/ViewAPD.aspx?id=900226 Au-Li.
95. Bervas, M., Badway, F., Klein, L.C. & Amatucci, G.G. Bismuth fluoride nanocomposite as a positive electrode material for rechargeable lithium batteries. *Electrochem. Solid State Lett.* 8, A179-A183 (2005).
96. Bervas, M., Klein, L.C. & Amatucci, G.G. Reversible conversion reactions with lithium in bismuth oxyfluoride nanocomposites. *Journal of the Electrochemical Society* 153, A159-A170 (2006).
97. Kwon, N.H. et al. Enhanced electrochemical performance of mesoparticulate LiMnPO4 for lithium ion batteries. *Electrochem. Solid State Lett.* 9, A277-A280 (2006).
98. Bhaviripudi, S., Reina, A., Qi, J.F., Kong, J. & Belcher, A.M. Block-copolymer assisted synthesis of arrays of metal nanoparticles and their catalytic activities for the growth of SWNTs. *Nanotechnology* 17, 5080-5086 (2006).
99. Bhaviripudi, S., Qi, J., Hu, E.L. & Belcher, A.M. Synthesis, characterization, and optical properties of ordered arrays of III-nitride nanocrystals. *Nano Letters* 7, 3512-3517 (2007).
100. Uchida, M. et al. Biological containers: Protein cages as multifunctional nanoplatforms. *Advanced Materials* 19, 1025-1042 (2007).
101. Polanams, J., Ray, A.D. & Watt, R.K. Nanophase iron phosphate, iron arsenate, iron vanadate, and iron molybdate minerals synthesized within the protein cage of ferritin. *Inorganic Chemistry* 44, 3203-3209 (2005).
102. Kramer, R.M., Li, C., Carter, D.C., Stone, M.O. & Naik, R.R. Engineered protein cages for nanomaterial synthesis. *Journal of the American Chemical Society* 126, 13282-13286 (2004).
103. Meldrum, F.C., Wade, V.J., Nimmo, D.L., Heywood, B.R. & Mann, S. Synthesis of Inorganic Nanophase Materials in Supramolecular Protein Cages. *Nature* 349, 684-687 (1991).